

NASA-CR-172,192

NASA Contractor Report 172192

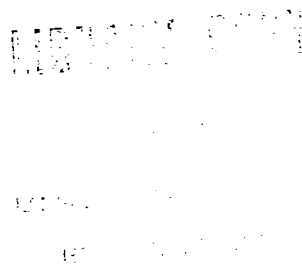
NASA-CR-172192
19830025700

**FAILURE ANALYSIS OF COMPOSITE LAMINATES
INCLUDING BIAXIAL COMPRESSION**

R. C. Tennyson and W. G. Elliott

UNIVERSITY OF TORONTO
Institute for Aerospace Studies
Toronto, Ontario, Canada

Grant NSG-7409
August 1983



National Aeronautics and
Space Administration

Langley Research Center
Hampton, Virginia 23665



NF02503

Contents

	<u>Page</u>
Acknowledgement	iii
Nomenclature	iv
1. Introduction	1
2. The Tensor Polynomial Failure Criterion	5
2.1 Cubic Form	5
2.2 Principal Strength Tensors	9
2.3 Interaction Strength Tensors	9
3. Biaxial Compression Experiment	11
3.1 Experiment Design	11
3.2 Test Specimen Design	13
3.3 Test Specimen Fabrication	16
3.4 Biaxial Compression Test Rig	18
3.5 Experimental Procedure	19
3.6 Experimental Results	21
4. Analysis of Failure Equation	22
4.1 Calculation of Interaction Tensors	22
4.2 Failure Surface and Profiles	23
4.3 Strength Prediction Profiles For Biaxial Loading of Laminates	25
5. Application of Strength Criterion to Laminates With Holes	27
6. Conclusions	28
References	30
Tables	33
Figures	36

	Page
Appendix A: Application of Strength Criterion to Fatigue Life Prediction	79
Appendix B: Stress Diffusion in an Aluminum Cross-Beam in Bending	81
Appendix C: Biaxial Bending of Aluminum Cross-Beam	88
Appendix D: Finite Element Analysis of the Honeycomb Sandwich Cross-Beam	95
Appendix E: Cross-Beam Analysis Using Beam Theory	101
Appendix F: Technical Drawings of the Biaxial Compression Test Rig	110

Acknowledgements

The authors would like to acknowledge the contribution made to this research program by Mr. Qi Rufan, a visiting Chinese scholar from Harbin, who performed the strength tests and analysis on the samples with circular holes. In addition, the financial aid of the Natural Sciences and Engineering Research Council of Canada, (Grant No. A-2783) has provided a valuable supplement to the support received from the U.S. National Aeronautics and Space Administration under Grant No. NSG-7409. We are also very appreciative to Mr. Don Baker (NASA Langley) for his continued interest in our work.

Nomenclature

C_{ij}	load parameter coefficients
d	hole diameter
d_1, d_2	beam dimensions
E_{11}, E_{22}	orthotropic moduli of elasticity in the 1 and 2 directions, respectively
E_c, E_h, E_m	moduli of elasticity of the composite, honeycomb and metal, respectively
EI	bending stiffness
$F_1, F_2, F_3, F_4, F'_1, F'_3, F$	forces
F_i, F_{ij}, F_{ijk}	lamina strength tensors of the 2nd, 4th and 6th ranks, respectively
G_{12}	orthotropic shear modulus of elasticity in the 1-2 plane
ℓ_1, ℓ_2, ℓ_3	beam dimensions
$\ell_{T,C,S,B}$	characteristic distances for tension, compression, shear and biaxial loading, respectively
L_1, L_2	beam dimensions
M_x	beam bending moment
M_x, M_y	laminate bending moment resultants
N_x, N_y	laminate normal stress resultants
P	hydraulic force
p	line load (force/unit length)
S	static lamina shear strength measured in 1-2 plane
S_D	fatigue shear strength of lamina measured in the 1-2 plane for given N and R values
W	sample width
X, X'	tensile and compressive static lamina strengths measured in the 1-direction

x_D, x'_D	tensile and compressive lamina fatigue strengths measured in the 1-direction for given N and R values
y, y'	tensile and compressive static lamina strengths measured in the 2-direction
y_D, y'_D	tensile and compressive lamina fatigue strengths measured in the 2-direction for given N and R values

Greek Symbols

α	biaxial stress ratio
γ	shear strain
ϵ	normal strain
θ	fiber orientation relative to structural x-axis
λ	structural load parameter
ν	Poisson's ratio
σ	normal stress

Subscripts

x, y	orthogonal in-plane structural axes
$1, 2$	lamina material axes parallel and orthogonal to the fiber reinforcement, respectively
6	indicates shear properties in the 1-2 plane

1. Introduction

With the advent of composite material primary structural components in advanced high performance aircraft and helicopters, the need for proven predictive formulations to quantify the strength of laminates is of paramount concern. Not only is this important in the initial structural design phase, but efficient systems management programs require the ability to define 'accept/repair' criteria and non-destructive inspection intervals, thus necessitating the development of a methodology for assessing the effect of defects as well.

In the design of laminates, one of the major difficulties still confronting the analyst is that of selecting a suitable strength criterion. This problem is of course further compounded by the presence of holes, interlaminar flaws and boundary conditions which give rise to local stress concentrations and three-dimensional stress fields. Suffice it to say that an accurate static strength prediction for a laminate subject to these conditions represents a considerable analytical task. To extend this predictive capability to include fatigue loading represents an even more difficult problem. One can illustrate the various aspects involved by examining the flow chart of Fig. 1. For a given external load system (i.e., including temperature), one first needs to calculate the stress state in each lamina. If the effects of flaws and boundary conditions are not considered, then classical laminate theory can be used. Otherwise, recourse to complex analytical models and fracture mechanics considerations are necessary.

The application of any failure criterion first requires a relatively accurate evaluation of the stress field. This is not at all a trivial task as, in general, composite failures result from complex three-dimensional stress states and the materials are anisotropic. Thus, from

an applications point of view it seems that the assumption of laminate homogeneity must be made and this assumption has been determined to be reasonable even for cracked structures, provided that the elastic crack tip singularity contains a sufficient number of fibers [1]. In addition there are several other features of the problem which must be considered. First, is the failure dominated by planar or three-dimensional phenomena? For example, if delamination is a predominant mode of failure, then a three-dimensional analysis is a necessity. On the other hand, if the failure is planar, then it is reasonable to approach the problem from a conventional lamina-laminate approach. The second consideration relates to the absence or presence of flaws. In this regard, there are basically three cases; nominally flaw free, sharp flaws (cracks, delaminations) and smooth flaws (circular holes, cutouts). The failure criterion adopted and the corresponding stress analysis should probably address each of the above situations individually since it seems at present, that it is not possible to encompass all failure possibilities using a single failure criterion.

Once the stress field is known, it would appear that the application of a lamina failure criterion would be appropriate, at each 'point' or 'element' (if finite element techniques are used) throughout the laminate. Because of local stress concentrations, one would presume that failure initiates in the highest stressed region and progresses through the laminate. However, previous analytical and experimental studies on holes and cracks [Refs. 2, 3] for example, have shown poor correlation using this approach and recourse to 'characteristic distances', which define either 'evaluation points' or 'integration intervals' was necessary. These 'characteristic distances' were obtained from test data on laminates in combination with the calculated stress fields.

It should also be noted that environmental effects can readily be taken into account by measuring the change in the constitutive properties (such as E_{11} , E_{22} , G_{12} , ν_{12}) and strength parameters. In the latter case, however, one requires a strength criterion before evaluating the appropriate coefficients. Such a criterion should also include three-dimensional stress effects consistent with the stress analysis.

An alternative method to that involving detailed stress calculations coupled with selected laminate strength measurements is a phenomenological approach. Assuming a given lamina failure criterion, one can proceed to evaluate the strength parameters as a function of flaw size/plate width, flaw location and environment. Thus, a laminate is treated as though it had no flaw but consisted of individual lamina having strength properties suitably reduced according to the above parameters.

Up to present, the discussion has focussed on static strength predictions. It is of interest to examine if these methods can be extended to predict fatigue failure of laminates. Previous work by other authors [4-6] has shown that the use of 'fatigue functions', based on simple static quadratic failure relations, can yield reasonable correlation with test data in many instances. In these cases, only the fatigue strengths under tension-tension and shear loading were required (X , Y , S) although a delamination effect was included. Similar work based on a quadratic Tsai-Hill failure criterion has also been completed [7] , again using only the X , Y and S strength parameters. Although reasonable comparisons with test data were reported in Ref. 7 for S-glass/epoxy (SP-250-SF1), such was not the case for graphite/epoxy (GRE) (E 788/T300) based on limited results to date. However, despite the disagreement, it is felt that this approach should be pursued utilizing an improved strength criterion in combination with fatigue

functions derived from tension, compression, torsion and biaxial load tests, a brief outline of which is presented in Appendix A.

In this investigation, effort has been directed towards evaluating the tensor polynomial failure criterion, which was advocated as early as 1966 by Malmeister [8] for 'unflawed' laminates. This failure model has been further developed extensively by Tsai and Wu [9] in quadratic and cubic forms [10]. However, it has also been found [10] that the cubic form can lead to some undesirable features. The mathematical nature of the cubic equation is such that the failure surface in stress space ($\sigma_1, \sigma_2, \sigma_6$) is not closed. Thus, there exist situations for which the cubic failure criterion will predict that the ultimate strength of a laminate is infinite. This phenomenon was found [10,11] to occur for some regions in the compression-compression quadrant for example.

These difficulties have led to the desire to obtain some experimental results in this 'open area' of the compression-compression quadrant. With these experiments, and some additional analysis, it was hypothesized that the open areas of the failure surface could be closed. Thus the cubic tensor polynomial would be all the more viable as a failure criterion. At this point, it is reasonable to question the need for retaining the cubic interaction terms. However, it has been found that in certain biaxial load cases, these terms contribute substantially to the ultimate strength prediction [10-12] and must therefore be included in the formulation. On the other hand, it should be emphasized that for many load cases, particularly simple tension and compression, little difference in failure loads is predicted between the quadratic and cubic models. This feature will be implemented later when the quadratic form is employed to analyse samples containing circular holes. This report

describes the design of an experimental technique and the subsequent testing of a composite laminate under a biaxial compressive loading. The results are then used to obtain new coefficients for the cubic tensor polynomial. The improved failure surfaces that are calculated from the biaxial compression experiment are studied, and some comparisons are made between the revised cubic and quadratic theories.

Complete descriptions of the analysis and design of the biaxial compression apparatus are provided in Appendices D-F.

In addition to the refinement of the tensor polynomial failure criterion, a combined analytical and experimental program was undertaken to demonstrate its application in predicting the tensile strength of laminates with holes. This work is described in Section 5.

2. The Tensor Polynomial Failure Criterion

2.1 Cubic Form

The general form of the tensor polynomial failure criterion is [8,9]

$$F_i \sigma_i + F_{ij} \sigma_i \sigma_j + F_{ijk} \sigma_i \sigma_j \sigma_k + \dots = f(\sigma) \begin{cases} < 1 & \text{no failure} \\ = 1 & \text{failure} \\ > 1 & \text{failure exceeded} \end{cases} \quad (1)$$

$i, j, k = 1, 2, \dots, 6$

The σ_i represents the six principal stresses and F_i , F_{ij} and F_{ijk} are strength tensors of 2nd, 4th and 6th rank, respectively. If one considers a cubic formulation and restricts the analysis to a state of plane stress, then Eq. (1) reduces to

$$F_i \sigma_i + F_{ij} \sigma_i \sigma_j + F_{ijk} \sigma_i \sigma_j \sigma_k = 1 \quad i = 1, 2, 6 \quad (2)$$

It is further assumed that the material exhibits some form of symmetry and thus $F_{ij} = F_{ji}$, $F_{ijk} = F_{ikj} = \dots = F_{kji}$, etc. Furthermore, it can

be shown that [9] F_{iii} terms can be discarded. If the material exhibits equal strength in both positive and negative shear, then the failure criterion should not depend upon the sign of σ_6 . Since this is true for most materials, including the one considered in this report, all odd order terms of σ_6 in Eq. (2) can be removed. Finally, Eq. (2) reduces to the following:

$$\begin{aligned} F_1\sigma_1 + F_2\sigma_2 + 2F_{12}\sigma_1\sigma_2 + F_{11}\sigma_1^2 + F_{22}\sigma_2^2 + F_{66}\sigma_6^2 \\ + 3F_{112}\sigma_1^2\sigma_2 + 3F_{122}\sigma_1\sigma_2^2 + 3F_{166}\sigma_1\sigma_6^2 + 3F_{266}\sigma_2\sigma_6^2 = 1 \end{aligned} \quad (3)$$

This is the final form of the cubic tensor polynomial that is used as a lamina failure criterion. It can be considered to present the equation of a surface in stress space $(\sigma_1, \sigma_2, \sigma_6)$. To visualize this, consider a surface enclosing the origin formed by the intersection of orthogonal σ_1 , σ_2 and σ_6 axes (Fig. 2). Also, consider a load starting at the origin within this surface and pointing in an arbitrary direction. As the material is loaded, its state of stress increases along this path. The location at which the load path intersects the surface represents the point of failure.

If one considers a linear load path, not necessarily commencing at the origin, then the principal stresses can be written as a function of a load parameter, λ , such that

$$\begin{aligned} \sigma_1 &= C_{11}\lambda + C_{12} \\ \sigma_2 &= C_{21}\lambda + C_{22} \\ \sigma_6 &= C_{31}\lambda + C_{32} \end{aligned} \quad (4)$$

Substituting these equations into Eq. (3) yields

$$a\lambda^3 + b\lambda^2 + c\lambda + d = 0 \quad (5)$$

where

$$a = 3(F_{112}C_{11}^2C_{21} + F_{122}C_{11}C_{21}^2 + F_{166}C_{11}C_{31}^2 + F_{266}C_{21}C_{31}^2) \quad (6a)$$

$$\begin{aligned}
b = & 3F_{112}(C_{11}^2 C_{22} + 2C_{11} C_{12} C_{21}) + 3F_{122}(C_{12}^2 C_{21} + 2C_{11} C_{21} C_{22}) \\
& + 3F_{166}(C_{12}^2 C_{31} + 2C_{11} C_{31} C_{32}) + 3F_{266}(C_{22}^2 C_{31} + 2C_{21} C_{31} C_{32}) \quad (6b) \\
& + F_{11} C_{11}^2 + F_{22} C_{21}^2 + F_{66} C_{31}^2 + 2F_{12} C_{11} C_{21}
\end{aligned}$$

$$\begin{aligned}
c = & 3F_{112}(2C_{11} C_{12} C_{22} + C_{12}^2 C_{21}) + 3F_{122}(2C_{12} C_{21} C_{22} + C_{11} C_{22}^2) \\
& + 3F_{166}(C_{11}^2 C_{32} + 2C_{12} C_{31} C_{32}) + 3F_{266}(C_{21}^2 C_{32} + 2C_{22} C_{31} C_{32}) \\
& + 2F_{11} C_{11} C_{12} + 2F_{22} C_{21} C_{22} + 2F_{66} C_{31} C_{32} \quad (6c) \\
& + 2F_{12} (C_{11} C_{22} + C_{21} C_{12}) + F_1 C_{11} + F_2 C_{21}
\end{aligned}$$

$$\begin{aligned}
d = & 3F_{112} C_{12}^2 C_{22} + 3F_{122} C_{12} C_{22}^2 + 3F_{166} C_{12} C_{32}^2 \\
& + 3F_{266} C_{22} C_{32}^2 + F_{11} C_{12}^2 + F_{22} C_{22}^2 + 2F_{12} C_{12} C_{22} \\
& + F_{66} C_{32}^2 + F_1 C_{12} + F_2 C_{22} - 1 \quad (6d)
\end{aligned}$$

Once the coefficients of the load parameter, C_{ij} , have been specified, Eq. (5) can be solved for the two ultimate failure loads, corresponding to positive and negative values of λ . However, the solution of this cubic equation will yield a set of three roots, so a selection criterion must be used to establish which of the roots is valid.

These sets of roots can be classified into three groups: three real distinct roots, three real roots with two equal, and one real root with a complex conjugate pair. These three possibilities are illustrated in Fig. 3 where $f(\lambda)$ (Eq. 5) is plotted as a function of the load parameter, λ . Any state of stress which results in an $f(\lambda)$ below the λ -axis represents a 'no-failure' condition. However, once $f(\lambda)$ becomes greater than or equal to zero, the material has failed, and the

values of λ for $f(\lambda)=0$ represent the ultimate failure loads.

For the first case of three distinct real roots (Fig. 3a), the two physically realistic values of λ_{ult} are those that bound the local minimum of the curve. The third root is superfluous since it cannot be reached from the origin without passing through the failed state of $f(\lambda)>0$.

The second case of two equal roots is also straightforward (Fig. 3b). Here there exists a local minimum bounded on either side by only two roots. The monotonically decreasing portion of the curve cannot be reached without passing through the $f(\lambda)=0$ value, and therefore it is not an admissible region.

The last group of roots, the single real value with a complex conjugate pair, is represented in Fig. 3c. Mathematically, the entire curve below the λ -axis is an admissible region since it can be reached from $\lambda=0$ without passing through a failed state. Thus the value of λ is unbounded on one side of the origin. This effect arises from the undesirable nature of the cubic polynomial to be 'open-surfaced'. Hence, it is necessary to develop a scheme to artificially bound the local minimum. The method which has been proposed [12,14] is the intuitive one of taking the local maximum as the second root. Analytically, this involves solving the derivative of Eq. (5) for $\bar{\lambda}$ such that the second derivative is positive,

ie;
$$f'(\lambda) = 3a\lambda^2 + 2b\lambda + c = 0 \quad (7)$$

Therefore,

$$\bar{\lambda} = \frac{-2b \pm \sqrt{4b^2 - 12ac}}{6a}$$

where

$$f''(\bar{\lambda}) = 6a\bar{\lambda} + 2b > 0$$

This method is satisfactory if the local maximum is relatively close to the λ -axis. However, if the $f(\lambda)$ curve appears as shown in Fig. 4, the local maximum does not intuitively represent the best solution. Indeed, it is difficult to use any intuitive method to establish the value of the second root for this case. This is the situation that arises in the third quadrant (compression-compression) of the (σ_1, σ_2) planar surface.

2.2 Principal Strength Tensors

The principal strength tensors for the cubic polynomial are F_1 , F_{11} , F_2 , F_{22} and F_{66} . It has been shown by Wu [15] that these are experimentally derivable quantities from simple tension, compression and shear tests; ie;

$$F_1 = \frac{1}{X} - \frac{1}{X'} \quad F_2 = \frac{1}{Y} - \frac{1}{Y'} \quad F_{11} = \frac{1}{XX'} \quad F_{22} = \frac{1}{YY'} \quad F_{66} = \frac{1}{S^2} \quad (8)$$

Extensive experimentation on 3M SP288-T300 GRE has been performed in Ref's. [10-12] to determine the values for these five principal strength tensors. The results are summarized in Table 1.

2.3 Interaction Strength Tensors

The nature of these tensor components demands that complicated multi-load experimental techniques be used to determine material strengths with interacting principal stresses. These experiments can be expensive and tedious to perform. Consequently a hybrid method was devised [10-11] using only one experiment and four constraint equations to determine the interaction tensors. However, this approach is inadequate in providing a reasonable solution in the compression-compression quadrant of the (σ_1, σ_2) plane. The following alternate method has been developed to overcome this problem.

Consider a biaxial experiment involving only σ_1 and σ_2 stresses. With σ_6 equal to zero, the following tensor polynomial equation is

obtained from Eq. (3)

$$\begin{aligned} F_{12}(2\sigma_1\sigma_2) + F_{112}(3\sigma_1^2\sigma_2) + F_{122}(3\sigma_1\sigma_2^2) \\ = (1 - F_1\sigma_1 - F_2\sigma_2 - F_{11}\sigma_1^2 - F_{22}\sigma_2^2) \end{aligned} \quad (9)$$

Having previously established the values of the principal tensors, there are three unknowns in this equation: F_{12} , F_{112} and F_{122} . By performing three different strength experiments in the (σ_1, σ_2) plane, three simultaneous equations of the form of Eq. (9) can be obtained. Solving this set of equations will yield values for the interaction tensors. It should be noted that this technique does not guarantee closure in the (σ_1, σ_2) plane. The three experiments must be judiciously selected so that closure will be obtained.

The remaining two interaction parameters, F_{166} and F_{266} , are then determined using the method of constraint equations which are derived by setting the discriminant of the cubic polynomial equation (Eq. (5)) to zero. This has the effect of forcing the failure equation to yield three real roots, two of which are equal, along the chosen load path.

Previous work [10,11] has used internal pressure loading of symmetric balanced $(\pm\theta)_S$ laminated tubes for different values of θ as the load paths. Under this type of loading, with the load parameter equal to internal pressure,

$$\begin{bmatrix} C_{11} \\ C_{21} \\ C_{31} \end{bmatrix}_k = [T]_k [\bar{Q}_{ij}]_k [A]^{-1} \begin{bmatrix} R/2 \\ R \\ 0 \end{bmatrix} \quad (10)$$

and

$$\begin{bmatrix} C_{12} \\ C_{22} \\ C_{32} \end{bmatrix}_k = \begin{bmatrix} 0 \\ 0 \\ 0 \end{bmatrix} \quad (11)$$

where R represents the tube radius. Note that for symmetric balanced tubes, the C_{ij} are equal for each ply. Using the above, Eq. (6) reduces to

$$\begin{aligned} a &= 3(F_{112}C_{11}^2C_{21} + F_{221}C_{11}C_{21}^2 + F_{166}C_{11}C_{31}^2 + F_{266}C_{21}C_{31}^2) \\ b &= F_{11}C_{11}^2 + F_{22}C_{21}^2 + F_{66}C_{31}^2 + 2F_{12}C_{11}C_{21} \\ c &= F_1C_{11} + F_2C_{21} \\ d &= -1 \end{aligned} \quad (12)$$

Setting the discriminant of Eq. (5) to zero, and substituting $d=-1$, yields,

$$27a^2 + a(4c^3 + 18bc) - 4b^3 - b^2c^2 = 0 \quad (13)$$

By solving Eq. (10) for two different ply angles, θ , Eqs. (12) and (13) can be set up as a system of two nonlinear simultaneous equations in two unknown. The solution of this system will yield appropriate values for F_{166} and F_{266} .

3. Biaxial Compression Experiment

3.1 Experiment Design

To obtain the desired stress state of biaxial compression, several different experimental techniques were considered. These included: (1) combined external pressure and axial compression of tubes; (2) bending of honeycomb sandwich plates; (3) bi-directional compressive loading of coupons with small test sections; (4) bending of honeycomb sandwich cross-beams.

The most attractive of the above options is the combined loading of tubes. It is, at first glance, a straightforward experiment to implement and analyse. However, the experiment is susceptible to the problem of shell buckling. To overcome this, the tube dimensions would

have become unwieldy: very short and thick with a small diameter. The advantage of simple analysis no longer exists because the tube cannot be considered to behave as a shell, and boundary effects would have also become a problem. Thus, the first of the above options was eliminated.

The loading of plates or coupons to achieve a biaxial compressive state was deemed to be too complicated to implement experimentally. This left the bending of cross-beams as the most desirable experimental technique. The same conclusion was reached by Cole (Ref. 16).

Much experience has been obtained in the use of honeycomb sandwich beams in bending to achieve a uniaxial compressive stress state [17]. It is a natural extension of this test procedure to develop a beam in the shape of a 'cross' for compression-compression tests. By applying bending moments to each of the two perpendicular arms of this cross-beam, a biaxial compressive state can be produced in the region where the beams coincide.

The bending of honeycomb sandwich cross-beams has the advantage of being relatively simple to design experimentally, but also has the disadvantage of being difficult to analyse. Because of the complex nature of the cross-beam, a finite element subroutine called 'ADINA' [18] was employed. As a check on its ability to analyse the biaxial experiment, two cases were studied: uniaxial and biaxial bending of an aluminum cross-beam. The theoretical load-strain responses agreed very favourably with experimental results obtained using the bending rig described in Section 3.4. The results of these check cases are described more fully in Appendices B and C.

The finite element model of the composite cross-beam is presented in Appendix D. This model is the final version, based upon many

iterations, and includes the final specimen design described in the next section. One of the problems that involved this model was the difficulty in matching the analytical stiffness of the cross-beam to experimental results. Correction factors which were included in the finite element model solved this difficulty, but their necessity gives some indication of the complexity of the problem.

Finally, it was necessary to determine the stress ratio, σ_1/σ_2 , to use as a load path for the experiment. Since the purpose of the biaxial compression test is to close the compression-compression quadrant, it was decided to load the beam with a stress ratio that would create a load vector passing through the open area of the original cubic solution. Thus a biaxial compression stress ratio of about $\sigma_1/\sigma_2 = 13$ was initially chosen based on previous solutions. This value is perhaps not the optimum one for use in evaluating the strength tensors, but it does guarantee a data point in the open area of the quadrant. With no previous experimental data available in this region, it is valid as a first iteration.

3.2 Test Specimen Design

The first parameter that was fixed in the design of the test specimen was the ply layup. Since the objective of the biaxial compression experiment was to obtain a data point in the 1-2 plane, any laminate which would involve a failure with a shear stress component present could not be used. Also, the complexity of multimode failure during the initial testing process was deemed to be undesirable. Thus it was decided to use a unidirectional 0° laminate.

The primary concern in the design of the test specimen was to ensure that the first failure of the GRE would occur in the test section area without being initiated elsewhere. This premature failure could arise from two sources: (1) stress concentrations at the interior

corners of the cross-beam or (2) the lower strength of the cross-beam arms due to their uniaxial stresses. The first point is an obvious one and was solved, to a certain extent, by filleting the interior corners of the cross-beam. From tables of stress concentration factors (SCF) [19], it was found that rounding the interior corners to a radius of 0.5 inches was appropriate. This resulted in an SCF of about 2. Any further decrease in the SCF at the corners would have resulted in a fillet radius much too large to be practical.

The second problem mentioned above is not as obvious as the first. The ultimate load of a unidirection laminate under biaxial compression could be greater than the ultimate load under uniaxial compression, if the load vector, originating at the origin and intersecting the curve in the compression-compression quadrant, is larger than the load vectors along either of the compressive axes. Thus a uniform thickness GRE facing could fail on the cross-beam arms before ultimate stresses are reached within the test section.

The solution to this problem is to create a reduced thickness test section. This is equivalent to reinforcing the arms and corners of the cross-beam. The thickness ratio between the test section and the rest of the GRE facing was obtained from a consideration of the preliminary analysis in Fig. 5. This was deemed to be a "worst case" condition since the actual cubic representation of the 1-2 plane was not expected to dip as low, in the compression-compression quadrant, as this analysis predicted. Nevertheless, this was taken to be the design condition. The maximum ratio between the lengths of the compressive load vectors discussed above, and shown in Fig. 5 is about 4. Hence, the thickness ratio was also taken to be 4.

It is interesting to note that this thickness ratio is also

sufficient to solve the SCF problem at the cross-beam corners. Since the SCF is 2 and the thickness ratio is 4, the stresses at the corners will be about one half those in the test section.

The shape of the test section was chosen to be square. This simplifies the finite element analysis by allowing one to use only a few elements in the test section area. A circular test section would require a detailed fine structure consisting of many elements. The dimension of the test section was chosen to be 0.75 inches square, for convenience and sufficiency.

The major drawback with the reduced thickness test section is the tendency for the sample to fail at the thickness discontinuity. It is in this area where the stresses are the greatest. However, this effect was lessened by tapering the thickness change with resin during the fabrication process. The method will be described in the following section on specimen fabrication.

The thickness of the test section is largely determined by the honeycomb to which it is bonded. The minimum thickness is determined by stability requirements, such as intercellular buckling of the facing. However, the maximum thickness is established by the requirement that the ultimate compressive and shear stresses of the honeycomb are not to be exceeded.

Some other factors that also influence the design of the test specimen include the type of metal facing that is bonded to the tensile side of the honeycomb, its tensile strength and modulus, and the thicknesses of the metal and honeycomb. Other considerations include the beam bending moment arm (distance between load points) and the adhesive strength. All of the above parameters influence one another and hence, an iterative procedure was used to select the optima.

To do this, a computer program was written which calculated the stresses within the various components of the cross-beam. This program uses simple beam theory (Appendix E) for each of the cross-beam arms and some constraint equations at their intersection. It is recognized that the program only approximates the stresses, but it was nevertheless useful for design purposes given the cost of solving the finite element problem. The final parameters were verified with the finite element model as being within design limits. In addition to the computer program, the stability requirements for the composite facing were obtained from the design curves in Ref. 20.

The final design of the cross-beam test specimen resulted in a test section thickness of two plies (about 0.01 inches). Thus, the thickness of the surrounding composite was eight plies (about 0.04 inches). The tensile facing material was selected to be 7075-T6 aluminum for its low modulus and high strength characteristics. Also, corrugated honeycomb, Hexcel ALC-1/8-5052-.003, was chosen for the design because of its superior compressive and shear strengths compared to the expanded variety. Finally, the optimum thicknesses of the aluminum and honeycomb were found to be 0.25 inches and 1.5 inches, respectively.

3.3 Test Specimen Fabrication

The procedure used in the manufacture of GRE test specimens and honeycomb beams is well documented and only an outline will be given here. The GRE used in the fabrication of the cross-beam is 3M SP288-T300 prepreg tape. It was cut to shape using a cross-shaped template as a guide. The individual plies were laid up, along with resin bleeder cloth, on a steel mandrel coated with a releasing agent. The two plies that comprised the test section were laid up against the mandrel. The remaining six plies, being identical to the first two but with the

square test section cut out, were laid on top. Teflon coated release fabric separated the bleeder cloth from the prepreg.

A small steel insert, which was the size of the test section and the thickness of the remaining plys, was placed between the Teflon fabric and the bleeder cloth (Fig. 6). This insert had its edges rounded and served the double purpose of (1) keeping the test section from filling with resin and (2) creating contoured edges for the test section to eliminate sharp thickness gradients.

A cork resin dam was built around the edge of the sample and a steel caul plate was placed on top. The entire surface was covered with an air breather cloth and placed in a vacuum bag. (The entire layup sequence is depicted in Fig. 7.) The sample was then cured in an autoclave according to manufacturer's specifications. A photograph of the cured sample is shown in Fig. 8. The average thickness of the test section was measured to be 0.009 inches. The surrounding thickness of the composite was found to average 0.035 inches.

The second stage in the manufacture of the cross-beam is the bonding of the facings to the honeycomb. The adhesive that was used for this procedure was Cyanamid FM123-2 film adhesive, selected for its excellent shear properties and low temperature cure. The adhesive cure temperature must not exceed the glass transition temperature of the composite (in this case 275⁰F) or else degradation of properties will occur.

Prior to bonding, the aluminum facing was cleaned in an acid solution. Subsequently, all bonding surfaces of the honeycomb and facings were primed with Cyanamid BR-127 primer. The adhesive was cut to shape, placed between the parts, and cured according to manufacturers' specifications.

3.4 Biaxial Compression Test Rig

The assembled rig that was designed to carry out the biaxial compression tests is shown in Figs. 9 and 10. The design is basically an extension of the beam bending rigs that are currently in use at UTIAS for uniaxial compression testing [17].

The biaxial compression rig is designed to allow independent loading of the two cross-beam arms. This is an extremely powerful feature since it enables one to achieve almost any desired stress ratio within the test section. The stresses are induced in the sample by combining two distinct types of loadings. A diagram showing the applied loads is presented in Fig. 11. One of the arms is placed under a four-point bending moment. The second arm, due to the restraining action of the first arm, is loaded by an approximately three-point bending moment.

The first cross-beam arm is supported at the outside points by two simple-support pads (Fig. 12). The two inside loads that complete the four-point bending are applied by the central loading block illustrated in Fig. 13. (Note the two simple-support pads here also.) This loading block is held in position by four guide posts (Fig. 14) and is loaded, in a testing machine, through a ball bearing placed centrally in a divot on the upper surface of the block (Fig. 15). The ball bearing ensures that the load is applied centrally with no bending moments.

The second arm is loaded independently with hydraulic pistons and the load bar shown in Fig. 16. This load bar is placed along the lower surface of the cross-beam and transmits the loads through the customary simple-support pads. The hydraulic pistons load the sample through cables attached to the transfer blocks of the load bar. These blocks are pinned to allow only the transfer of pure forces to the load bar.

The simple-support pads are merely rocker type supports consisting

of a grooved pad capable of rotating on a fulcrum. These parts have all been machined from mild steel and then case hardened to protect the sharp surfaces through which the loads are transmitted.

Note that the configuration shown in Fig. 15 depicts the use of the compression rig without independent loading. This set up, with each of the cross-beam arms under a four-point bending moment, was used to load the aluminum cross described in Appendices B and C. However, this same arrangement was found difficult to implement with the composite cross-beam because of the stiffness discrepancies between the two arms.

The technical drawings of the biaxial compression rig are given in Appendix F.

3.5 Experimental Procedure

Prior to its testing, the honeycomb cross-beam was instrumented with strain gauges. A single rosette (Micro-Measurements CEA-125WT-350) was bonded to the test section with Micro-Measurements M-Bond 200 adhesive. This rosette monitored the biaxial strain in the test section in order that the failure stress could be determined from a knowledge of the material properties.

The cross-beam was then placed in the test rig with the 0° direction of the composite facing under the four point bending load applied by the tensile testing machine (Tinius Olsen). The hydraulic pistons and cables were then connected to the rig while in place in the testing machine. The experimental set-up before testing is presented in Fig's. 17 and 18.

An overall view of the associated instrumentation, monitoring equipment and test set-up is shown in Fig. 19. A load cell on the Tinius Olsen testing machine was connected to the abscissa of a dual pen X-Y plotter. The two ordinates of the plotter received signals from the strain gauge conditioning units. In addition, digital outputs from

the conditioning units were used to manually record the strains. The pressure in the hydraulic lines was measured with a pressure transducer and associated conditioning unit. This output signal was then connected to the abscissa of a second, single pen X-Y plotter and also to a digital voltmeter for manual recording. The ordinate of this plotter was also connected to the load cell. A schematic of the setup is presented in Fig. 20.

Since the two loads (hydraulic pressure and testing machine) were applied simultaneously and independently, a method was required to ensure that they were always being applied in the correct proportion. Knowing the desired ratio of the applied loads (Section 3.1), a line was drawn on the graph paper which represented the desired path of the pen on the X-Y plotter as it tracked the pressure transducer and load cell signals. By tracing this line during the test, one was guaranteed that the proper load ratio was being applied to the specimen. It should be noted here that due to the setup configuration, the load cell measured the sum of the applied compressive load of the testing machine and the applied load of the hydraulic pistons. Thus, referring to Fig. 11, the plotter recorded $(F + P)$ versus P . As the specimen was loaded with the testing machine, the desired load ratio was obtained by hand pumping the hydraulic pistons to follow the predetermined line on the X-Y plotter. It was found that this could be done with extreme ease and little deviation from the desired path.

As the test progressed, the strains and hydraulic pressures were noted and recorded at predetermined load increments. Simultaneously, the dual pen plotter recorded the load-strain responses to give a more complete, although less accurate record up to failure.

3.6 Experimental Results

The biaxial compression test was successful in achieving a proper compressive failure, as can be seen in the photographs of the failed specimen, Figs. 21 and 22. It should be noted that no portion of the composite facing appears to have buckled. A buckling failure is usually characterized by the failure area lifting up from the surrounding composite. Instead, the failure observed here is typical of the compressive failure mode of composites.

The location of failure is seen to first occur at the edge of the test section. It then propagates towards the corner of the beam. The failure at the thickness discontinuity was predicted. However, it is believed that the difference between the stresses at the failure location and those at the centre of the test section is not large. Experience with other types of compression experiments where failure can sometimes occur near loading grips, reinforcements, etc., indicates little correlation between ultimate load and location of failure. Since the composite surrounding the biaxial test section is basically reinforcement, the same can probably be said for this experiment, as well. Only until further experiments build up a data base can this be conclusively shown to be true.

The load-strain history for the specimen is presented in Fig. 23. The curves do not pass through the origin because of some initial takeup in the testing rig. The initial nonlinearity in the curves (below 1000 lb.) is due to the loading method at the start of the test to prevent premature failure of the cross-beam. Until the total load reached 1000 lb., the hydraulic pressure was below, and asymptotically approaching, the desired load ratio. To obtain the final strain at failure to be used in the calculation of the failure stresses, the linear portion of this curve was extrapolated to the measured failure load value.

This is the standard practice in cases where multiple failures occur. These ultimate strains and stresses, along with the failure loads, are given in Table 2, based on the material properties given in Table 1.

4. Analysis of Failure Equation

4.1 Calculation of the Interaction Tensors

The pair of ultimate stresses obtained from the biaxial compression experiment, along with those listed in Table 3, were employed to calculate the new values for F_{12} , F_{112} and F_{122} . The method used was that described in Section 2.4. The complete new set of strength tensors for use in the cubic polynomial criterion is shown in Table 4.

To verify the consistency of these new coefficients with previous experimental results, two check cases were analysed. The first case was the critical one of internal pressure loading of symmetric balanced $(\pm\theta)_s$ laminated tubes. Figure 24 shows some experimental results [10,12] of failure pressure versus lamination angle, along with cubic and quadratic predictions. These predictions were obtained with the use of the failure analysis program in Reference 15. Excellent agreement is observed between the cubic polynomial predictions and the experimental results. Again, one should note the inadequacy of the quadratic theory to accurately predict the failure load, as reported in [10].

The second check case involves some torsional strength experiments of tubes reported in Ref. (14). Figure 25 presents the ultimate shear strength of off-axis, four-ply laminated tubes versus lamination angle. As with the pressure loading case, the quadratic and new cubic strength prediction curves are plotted on this graph. Again it is seen that the cubic polynomial is superior to the quadratic as a failure criterion. However, whereas the quadratic prediction for internal pressure loading resulted in conservative estimates, the quadratic polynomial over-

predicts the strength of tubes under torsion. It should be noted that the poor correlation between experiment and theory for lamination angles greater than $\theta=35^0$ is due to shear buckling of the tubes. This phenomenon was reported by Wharram (Ref. 14).

The good agreement between the cubic theory and the established experimental results for the above two cases indicates that the new set of strength tensors is a reasonable one. The agreement does not validate the accuracy of the tensors under all forms of loading, but since the above cases are sensitive to differences between cubic and quadratic theories, any existing inconsistencies would have likely surfaced as a result of these checks.

4.2 Failure Surface and Profiles

The ultimate goal of this phase of the investigation was the closure of the cubic failure surface. The 1-2 planar failure surface that was recalculated with the new set of tensors is shown in Fig. 26. It can be seen that the use of the biaxial compression test has been entirely successful in closing this plane. Also notice that the quadratic theory seems to overpredict the strength of the material under biaxial compression. This could have dramatic implications in the design of composite parts if one incorrectly assumes that the quadratic theory is either exact or is a conservative estimate of the strength. The drawback to the stress pair resulting from the biaxial compression test is its proximity to the σ_1 axis. The stress ratio chosen for this experiment ($\sigma_1/\sigma_2 = 13$) was designed to travel down the throat of the open area of the cubic solution presented in Refs. 10,11. This ratio turned out to be much larger considering the lower than expected failure load. Further work is definitely necessary, not only to increase the data base, but also to obtain failures with a σ_1/σ_2 stress ratio less than 13.

For the sake of completeness, the cubic and quadratic surfaces for the 1-6 and 2-6 planes are presented in Figs. 27 and 28, respectively. These curves are similar to those reported earlier (Ref. 10). It is interesting to note that the dramatic differences in shape between the two strength criteria in the 2-6 plane have never been verified experimentally. Valuable information concerning the cubic polynomial could be obtained from some simple tension-shear tests on unidirectional laminates.

By looking at slices through the cubic surface parallel to the 1-2 plane, one can get an impression of its overall shape. Such a series of curves is presented in Fig. 29. An examination of this figure reveals the existence of a previously unknown open area in the tension-tension quadrant for $\sigma_6 \approx 10$ ksi. Recall that there is no sign dependence on the shear strength of the material. Thus the surface is mirror imaged in the 1-2 plane and has two areas where it is open. However, in contrast to the 1-2 plane of the original cubic solution, the surface pinches together before opening out. An alternate view of this surface is seen in Fig. 30, where one is now observing it along the σ_1 -axis. The pinching effect of the surface is quite apparent here also.

These open areas are representative of the third possibility to the solution of Eq. (5) described in Section 2.2; the case of one real and two complex roots. These regions are the result of the complex valued solution to the cubic equation. The technique that is used in an attempt to solve this problem is the evaluation of the cubic equation at its local maximum (Fig. 3c). This was done for the $\sigma_1=150$ ksi planar failure surface and is presented in Fig. 31. Notice how the local maximum solution closes the surface almost as one would do so intuitively, based upon the shapes of the $\sigma_1=0, 50$

and 100 ksi curves. Thus this 'patching' method can be considered to be a very successful engineering approximation to the complex root problem.

Finally, it is observed that the entire cubic failure surface has been closed using both experimental and analytical techniques thus eliminating one of the major criticisms for its use.

4.3 Strength Prediction Profiles for Biaxial Loading of Laminates

As an application of the new tensor coefficients and a comparison between quadratic and cubic theories, some strength prediction curves were re-derived for laminates under biaxial loading. The lamination sequence is fourply, symmetric balanced $(\pm\theta)_S$ and the material is 3M SP288-T300 GRE. The biaxial loads are N_x and N_y , and are applied with the ratio $\alpha = N_x/N_y$.

Figures 32 to 35 show profiles of the ultimate failure stress, $(\sigma_y)_{ult}$, as a function of lamination angle, θ , for the cubic tensor polynomial theory. Figures 36 to 39 show the corresponding profiles for the quadratic theory.

Each of the above figures shows the effect of varying the biaxial stress ratio, α , from 0 to ± 1 . For example, Fig. 32 presents the tension-tension case with N_x and N_y positive. Notice the definite existence of an optimum lamination angle for maximum strength. The case of $\alpha=0.5$ represents the internal pressure loading of tubes discussed in Section 4.1. The uncharacteristic sharp peaks that occur when α equals 0.6 and 0.7 are due to the effect of complex roots. At these locations, the solutions are described by the local maximum of the cubic equation. The corresponding quadratic profiles are given in Fig. 36. Notice that the quadratic maxima are significantly less than the cubic maxima. Of the remaining curves of biaxial

failure profiles, Figs. 33 and 37 are for $N_x > 0$ and $N_y < 0$; Figs. 34 and 38 for $N_x < 0$ and $N_y > 0$; and Figs. 35 and 39 for $N_x < 0$ and $N_y < 0$.

To more easily compare the differences between cubic and quadratic theories, Figs. 40 to 43 were compiled. They represent the loci of maximum failure stress and optimum fiber angle as a function of biaxial stress ratio. All failure stresses have been normalized with respect to their corresponding strength parameter, X or X' , depending upon the magnitude of N_y .

Figure 40 plots the case of $N_x, N_y > 0$ for $(\pm\theta)_s$ laminates. It is interesting to note the drastic difference between the maximum strengths predicted by the two theories. Yet, the optimum lamination angle is not nearly as affected by the choice of strength criterion. The effect of the complex root problem is evident here as well. The cubic locus has a distinct 'aberration' in it at $\alpha=0.6$ resulting from the "local maximum" solution. However, the deviation from the intuitive smooth path is, at most, ten percent. This difference is quite acceptable when one considers that a real solution does not even exist for $\alpha=0.6$ or 0.7. As long as the designer realizes that a complex solution exists for a given loading scheme, compensations can be made for the overprediction of the strength.

The next two curves for $N_x > 0, N_y < 0$ and $N_x < 0, N_y > 0$ show very little difference between the two theories. However, the final curve (Fig. 43) showing the compression-compression case indicates a significant difference. This is largely due to the results of the biaxial compression experiment which gave an ultimate stress much less than was predicted by the quadratic theory. Since this was the result of a single experiment, which is seldom sufficient to establish material properties, further experiments at other stress ratios may

alter compressive results. However, the biaxial compression experiment was successful and there is no reason to doubt its results.

The above figures illustrate the significant differences between cubic and quadratic strength theories. The discrepancies are not limited to a select few of possible load cases, but become quite apparent when a laminate is under a biaxial tension or biaxial compression load. Further experiments at different load ratios are necessary to confirm these differences.

5. Application of Strength Criterion to Laminates With Holes

Although the phenomenological approach to predicting the strength of laminates under plane stress conditions (without consideration for three-dimensional and stress concentration effects) has been demonstrated to work reasonably well, it is of interest to ascertain if the same methodology could be utilized to treat laminates with holes, i.e., in the presence of local stress concentrations. Other investigators have considered laminated composites with holes and cracks (such as Ref's. 2, 3) under simple tension loading for example, and they have shown that reasonably good correlations with test data can be achieved using a combined fracture mechanics approach and the notion of 'characteristic distances', as described earlier. Note that this latter method also relies on test data to solve for the 'characteristic distances'. To illustrate the difference between this technique and the 'all experimental' method, a flow chart comparison is given in Fig. 44.

This phase of the program involved a series of tension tests on off-axis (θ) and angle-ply ($\pm\theta$) glass/epoxy laminates (3M, 1003) containing circular holes with $d/W = 0.15, 0.25$ and 0.40 . Two or three replicates were tested for varying values of θ for both laminate configurations, the results of which are presented in Figs. 45 and 46.

Note that 'first failure' was taken as the laminate 'strength' value. This is consistent with the tests conducted on 0° and 90° laminates to determine both the tensor polynomial parameters and the 'characteristic distances' used in the 'point stress' calculations. Figures 47 and 48 present photographs of the off-angle and angle ply samples tested. As noted in Figs. 45 and 46, the predicted curves are based on 'point stress' calculations of the strength parameters for varying d/W . In Fig. 49, the curves were obtained from the experimentally determined strength coefficients for $d/W = 0.25$ (given in Table 5). One can readily see that both methods are in good agreement with test data.

6. Conclusions

The cubic tensor polynomial failure criterion has an inherent drawback in that the $(\sigma_1, \sigma_2, \sigma_6)$ surface in stress space is not closed. Thus there exist some cases for which the theory will predict an infinite failure load. This is partially solved with the use of three biaxial strength tests involving σ_1 and σ_2 . Using the results from these experiments, the three interaction tensors F_{12} , F_{112} and F_{122} can be evaluated. By choosing these tests properly, the problem of an open compression-compression quadrant in the 1-2 plane can be eliminated. The three tests which were found to close the plane are: the 'quadratic B_{12} ' test, a biaxial tension test, and a biaxial compression test. The remaining open areas of the surface, which are the result of the formation of complex roots of the cubic equation, can be closed by evaluating the cubic equation at its local maximum.

The experimental technique that was developed in this program for obtaining the biaxial compressive strength data for composite laminates has been found to be quite successful. The procedure involves the bending of honeycomb sandwich cross-beams with independent

loading of each arm. This loading scheme allows one to obtain almost any desired stress ratio. The major disadvantage with the use of the cross-beam bending method is the difficulty of analysing the stresses within the composite. This is compounded by the necessity of using a reduced thickness test section to localize the location of failure. Nevertheless, stress results were successfully obtained from strain gauge data and a knowledge of the material properties.

In analysing the differences between the cubic and quadratic tensor polynomial theories, it is seen that the cubic requires more experiments to evaluate the strength tensors. Some of these experiments, for example biaxial compression, are tedious and expensive to perform. The open nature of the cubic polynomial is a disadvantage that has, until now, been difficult to overcome. Nevertheless, the quadratic theory is, in many cases, inadequate to accurately predict the ultimate strength of composite laminates. In some instances, the quadratic can even over-predict the strength. This is particularly true of the compression-compression strength. It would be argued that most laminates under biaxial compression will fail due to buckling long before material failure occurs. The fact is that situations could arise where the difference between the prediction methods could be critical. For example, a composite facing under compression but stabilized by honeycomb, or a multimode failure where one or more plies is subjected to a compressive stress without the laminate being under biaxial compression. Since a failure criterion is only as good as its predictive ability, the cubic tensor polynomial is the obvious choice. The benefits far outweigh the disadvantages.

Finally, the application of the tensor polynomial failure criterion to the strength analysis of laminates with holes has been shown to

provide the same degree of correlation with test data as the method of 'characteristic distances'. Both approaches work well for uniaxial loading but insufficient evidence exists for biaxial load cases.

References

1. Snyder, M. D., Cruse, T. A., "Crack Tip Stress Intensity Factors in Finite Anisotropic Plates", Air Force Materials Laboratory, AFML-TR-73-209, Aug. 1973.
2. Nuismer, R. J., Whitney, J. M., "Uniaxial Failure of Composite Laminates Containing Stress Concentrations", Fracture Mechanics of Composites, ASTM STP 593, 1975.
3. Garbo, S. P., Ogonowski, J. M., "Strength Predictions of Composite Laminates with Unloaded Fastener Holes", AIAA J., Vol. 18, No. 5, May 1980.
4. Hashin, Z., Rotem, A., "A Fatigue Failure Criterion for Fiber Reinforced Materials", J. Composite Materials, Vol. 7, Oct. 1973.
5. Rotem, A., Hashin, Z., "Fatigue Failure of Angle Ply Laminates", AIAA J., Vol. 14, July 1976.
6. Rotem, A., "Fatigue Failure of Multidirectional Laminate", AIAA J., Vol. 17, March 1979.
7. Sims, D. F., Brogdon, V. H., "A Comparison of the Fatigue Behavior of Composites Under Different Loading Modes", Proc. ASTM Symp. on "Fatigue of Filamentary Composite Materials", Denver, Colorado, Nov. 1976.
8. Malmeister, A. K., "Geometry of Theories of Strength", Mekhanika Polimerov, Vol. 2, No. 4, 1966.
9. Tasi, S. W., Wu, E. M., "A General Theory of Strength for Anisotropic Materials", J. Composite Materials, Vol. 5, 1971.
10. Tennyson, R. C., MacDonald, D., Nanyaro, A. P., "Evaluation of the Tensor Polynomial Failure Criterion for Composite Materials",

- J. Composite Materials, Vol. 12, p. 63, 1978.
11. Nanyaro, A. P., "Evaluation of the Tensor Polynomial Failure Criterion for Composite Materials", Thesis for the Degree of Master of Applied Science, University of Toronto, 1978.
 12. Tennyson, R. C., Nanyaro, A.P., Wharram, G. E., "Application of the Cubic Polynomial Strength Criterion to the Failure Analysis of Composite Materials", J. Composite Materials Supplement, Vol. 14, p. 28, 1980.
 13. Wu, E. M., Scheublein, J. K., "Laminate Strength - A Direct Characterization Procedure", Composite Materials: Testing and Design (3rd Conf.), ASTM STP 546, June, 1974.
 14. Wharram, G. E., "Multi-Mode Failure Analysis of Laminated Composite Structures", Thesis for the Degree of Master of Applied Science, University of Toronto, 1980.
 15. Wu, E. M., "Optimal Experimental Measurements of Anisotropic Failure Tensors", J. Composite Materials, Vol. 6, 1972.
 16. Cole, B. W., Pipes, R. B., "Filamentary Composite Laminates Subjected to Biaxial Stress Fields", IIT Research Institute, Air Force Flight Dynamics Laboratory Report No. AFFDL-TR-73-115, 1974.
 17. Mabson, G. E., Hansen, J. S., Tennyson, R. C., Wharram, G. E., "Investigation of the Strength and Fatigue Properties of Graphite/Epoxy Laminates", Final Report to DND/DREP, DND/DSS, Contract No. 05Sb.97708-1-0043, 1982, Engineering Research Associates, 5 Framington Dr., Thornhill, Ontario, Canada.
 18. Bathe, K. J., "ADINA - A Finite Element Program for Automatic Dynamic Incremental Nonlinear Analysis", Report No. AE 81-1, 1982, Adina Engineering, 71 Elton Ave., Watertown, Mass. 02172.

19. Peterson, R. E., Stress Concentration Factors, John Wiley and Sons, 1974.
20. "Design Handbook for Honeycomb Sandwich Structures," Technical Services Bulletin TSB 123, Hexcel, March 1970.
21. Tennyson, R. C., Hansen, J. S., Heppler, G. R., Mabson, G., Wharram, G., Street, K. N., "Computation of Influence of Defects on Static and Fatigue Strength of Composites", Proc. AGARD 56th Meeting, Structures and Materials Panel, "Characterization, Analysis and Significance of Defects in Composite Materials", London, U.K., April 1983.

TABLE 1

Material Properties for Graphite/Epoxy

(3M SP288-T300)

<u>E₁₁</u> (psi)	<u>E₂₂</u> (psi)	<u>v₁₂</u>	<u>G₁₂</u> (psi)
20.5×10^6	1.4×10^6	0.26	0.594×10^6

Principle Strength Tensors for Graphite/Epoxy

(3M SP288-T300)

<u>F₁</u> <u>(ksi)</u> ⁻¹	<u>F₁₁</u> <u>(ksi)</u> ⁻²	<u>F₂</u> <u>(ksi)</u> ⁻¹	<u>F₂₂</u> <u>(ksi)</u> ⁻²	<u>F₆</u> <u>(ksi)</u> ⁻¹	<u>F₆₆</u> <u>(ksi)</u> ⁻²
2.482×10^{-3}	4.239×10^{-5}	1.035×10^{-1}	3.936×10^{-3}	0	5.172×10^{-3}

TABLE 2

Ultimate Strains, Stresses and Failure Loads
from the Biaxial Compression Test

	<u>Ultimate Strain ($\mu\epsilon$)</u>	<u>Ultimate Stress (ksi)</u>
Fiber Direction	-8870	-184.7
Matrix Direction	-5700	-11.3

	<u>Testing Machine F (1b.)</u>	<u>Hydraulic Pistons P (1b.)</u>
Ultimate Load	1918	482.

TABLE 3

Biaxial Tests for Evaluating the Interaction Strength Tensors

σ_1 (ksi)	σ_2 (ksi)	
161.5	-17.4	B_{12} test
187.2	7.0	Tension-Tension test
-184.7	-11.3	Compression-Compression test

TABLE 4
Strength Tensors for Graphite/Epoxy

(3M SP288-T300)

Principle Strength Tensors:

F_1 $(\text{ksi})^{-1}$	F_{11} $(\text{ksi})^{-2}$	F_2 $(\text{ksi})^{-1}$	F_{22} $(\text{ksi})^{-1}$	F_6 $(\text{ksi})^{-1}$	F_{66} $(\text{ksi})^{-2}$
-2.482×10^{-3}	4.239×10^{-5}	1.035×10^{-1}	3.936×10^{-3}	0	5.172×10^{-3}

Interaction Strength Tensors:

F_{12} $(\text{ksi})^{-2}$	F_{112} $(\text{ksi})^{-3}$	F_{122} $(\text{ksi})^{-3}$	F_{166} $(\text{ksi})^{-3}$	F_{266} $(\text{ksi})^{-3}$
-2.233×10^{-4}	-2.898×10^{-7}	-5.079×10^{-6}	-4.170×10^{-6}	-1.026×10^{-4}

Table 5 Comparison of Principal Tensor Polynomial Strength Parameters
for Glass/Epoxy Material (3M, 1003)

Case	Strength Parameters				
	F_1 $(\text{KSI})^{-1}$	F_{11} $(\text{KSI})^{-2}$	F_2 $(\text{KSI})^{-1}$	F_{22} $(\text{KSI})^{-2}$	F_{66} $(\text{KSI})^{-2}$
No hole ($d/W = 0$)	-3.076×10^{-3}	9.398×10^{-5}	2.344×10^{-1}	2.270×10^{-2}	2.142×10^{-2}
$d/W = 0.25$ Experiment only	-8.013×10^{-3}	4.045×10^{-4}	0.382	6.090×10^{-2}	8.000×10^{-2}
$d/W = 0.25$ Point stress -characteristic distance* from tests	-6.520×10^{-3}	3.397×10^{-4}	0.386	7.500×10^{-2}	8.300×10^{-2}

* $\ell_T = 0.07"$, $\ell_C = 0.09"$, $\ell_S = 0.10"$.

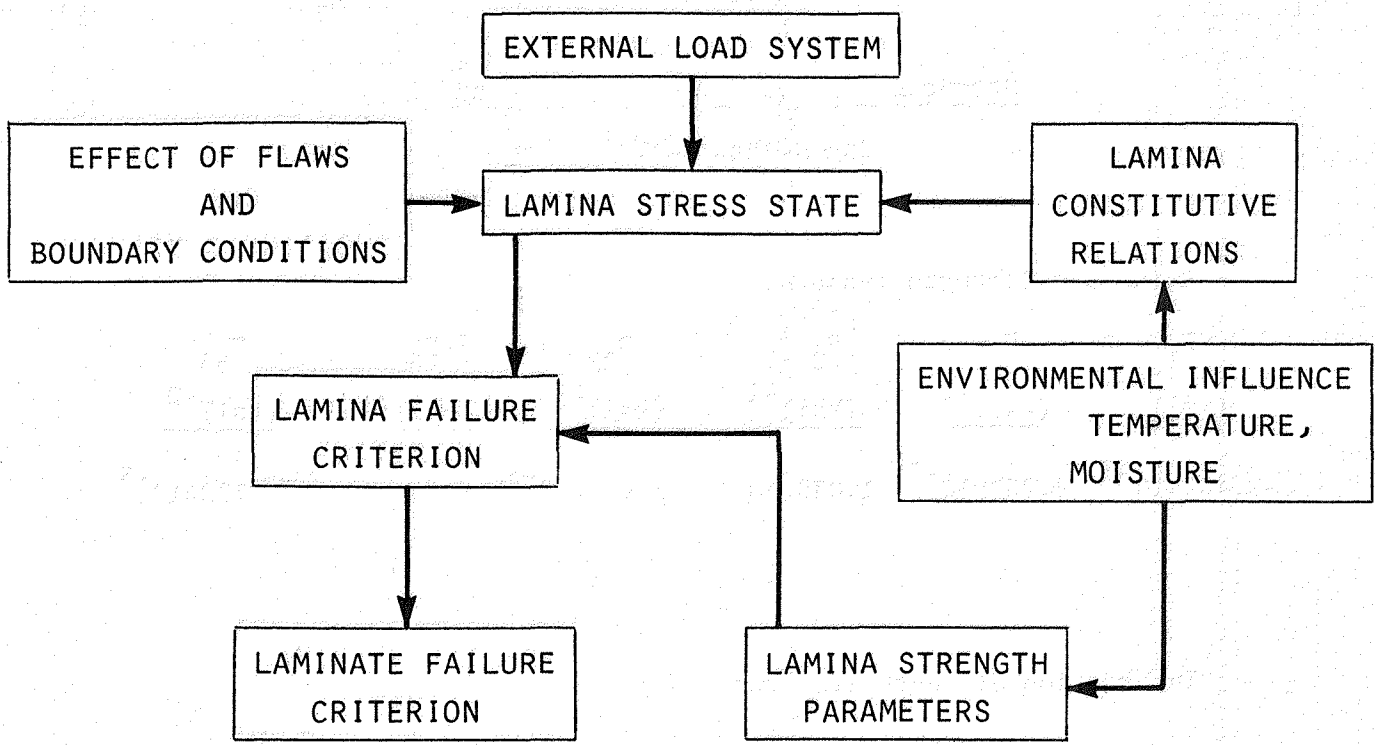


FIG. 1: CALCULATION PROCEDURE FOR DETERMINING STATIC AND FATIGUE STRENGTH OF LAMINATED STRUCTURES.

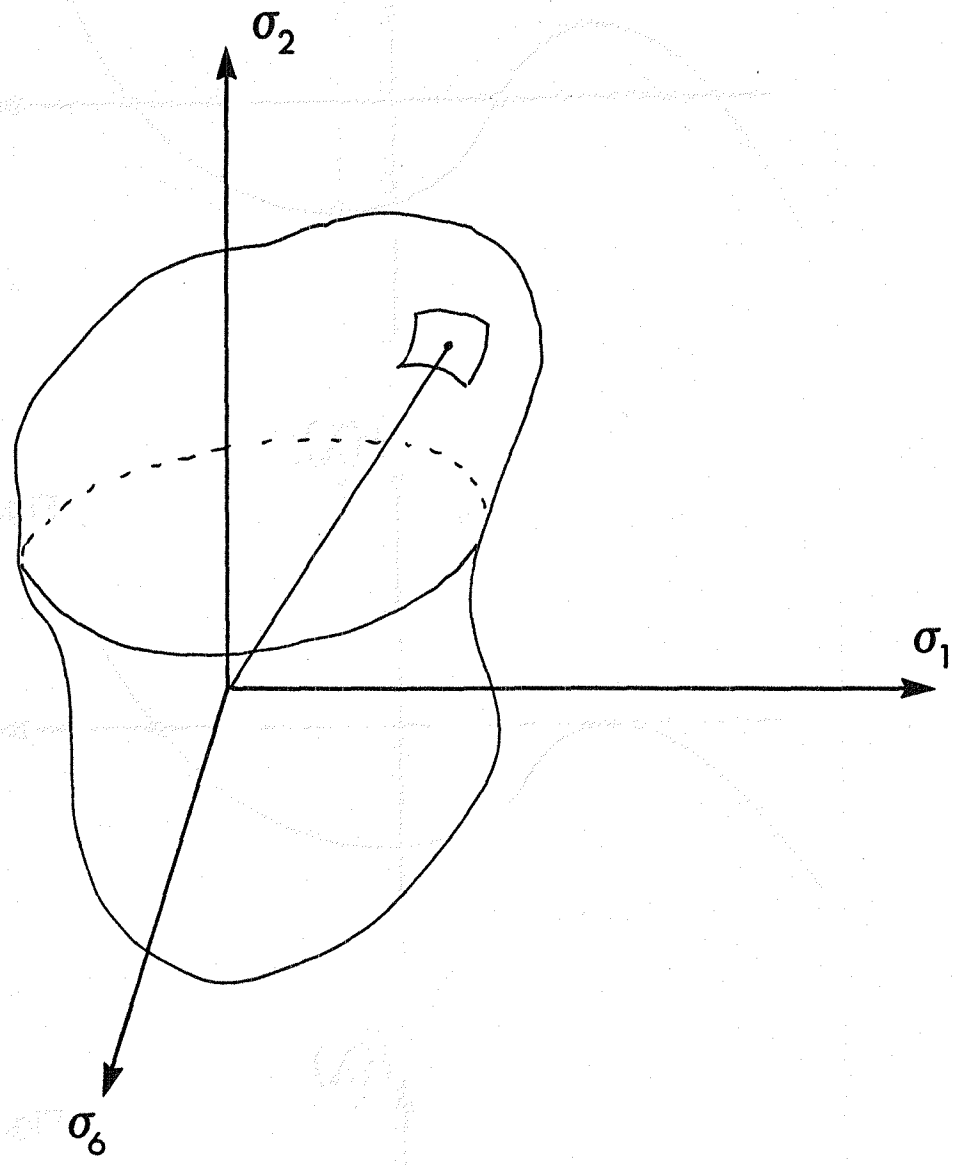


FIGURE 2: Arbitrary Failure Surface in Stress Space

Fig. 3a

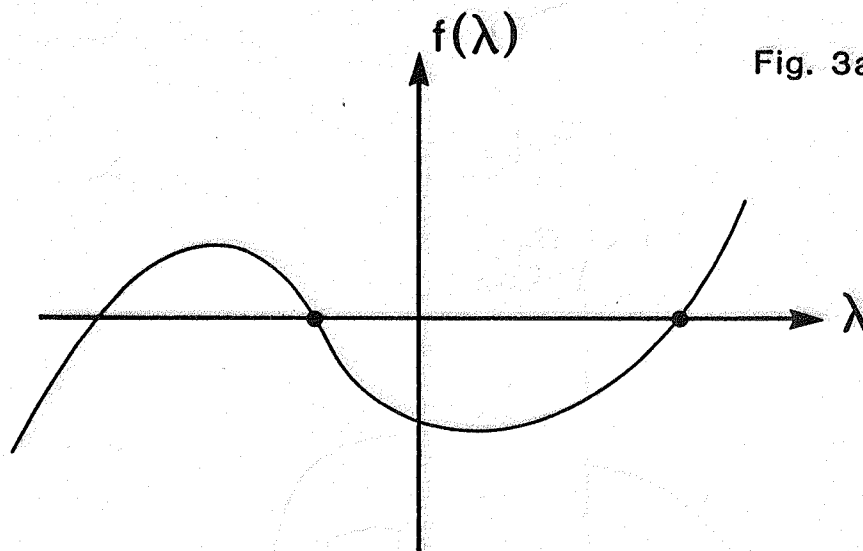


Fig. 3b

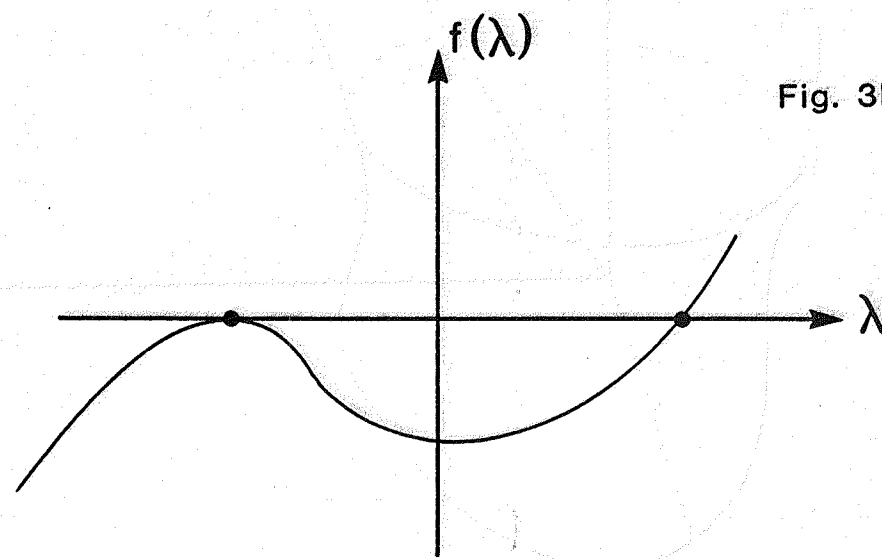
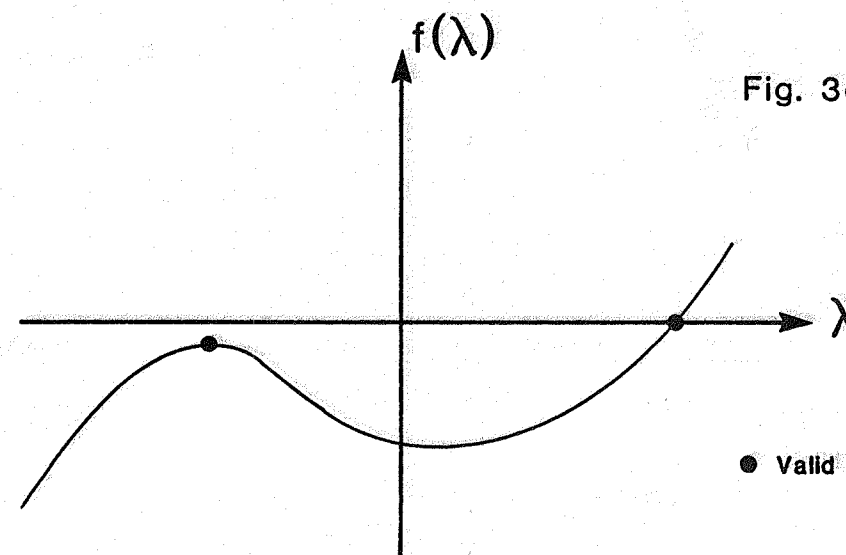


Fig. 3c



● Valid Failure Roots

FIGURE 3: Roots of the Cubic Polynomial

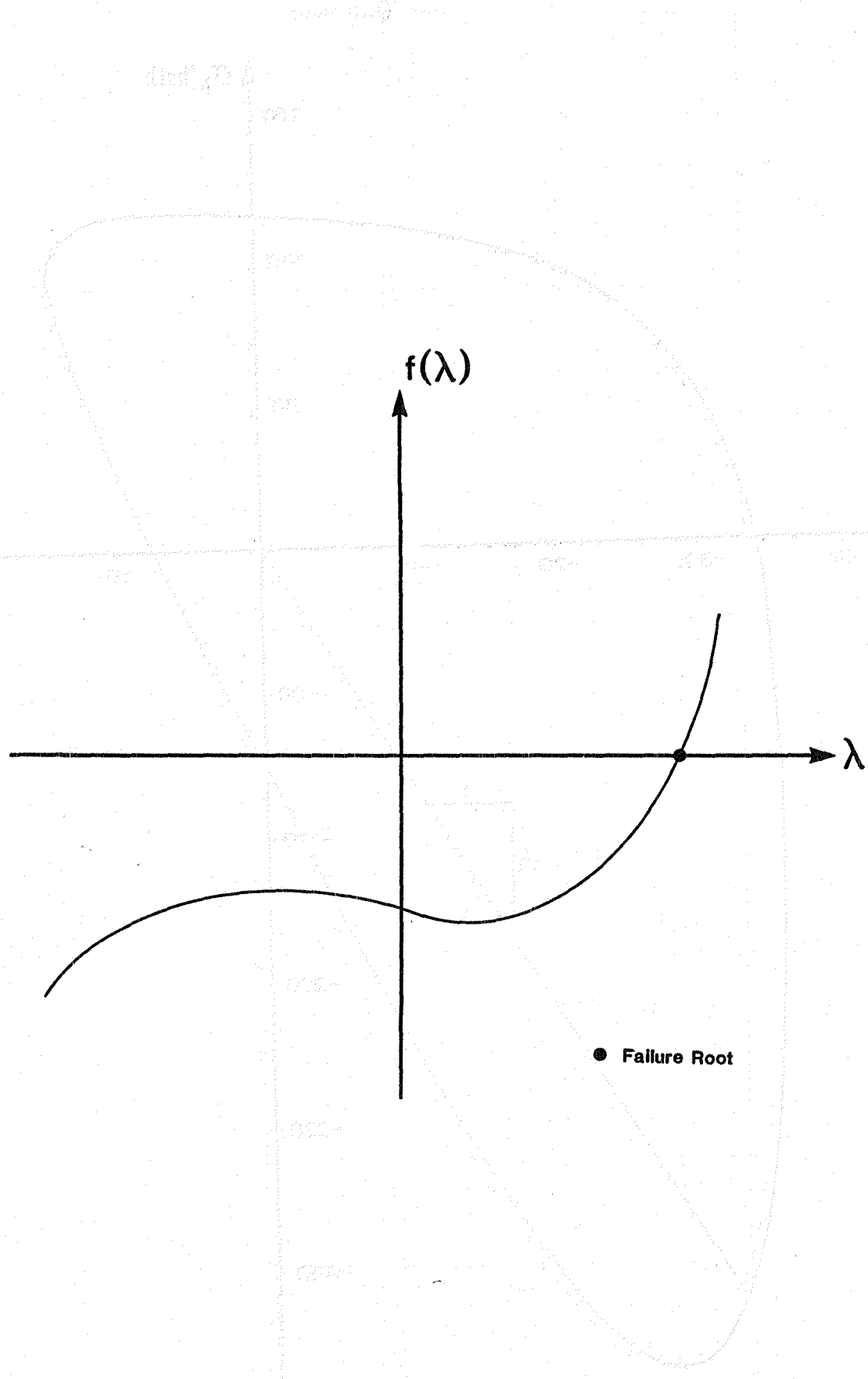


FIGURE 4: Ambiguous Complex Root of the Cubic Polynomial

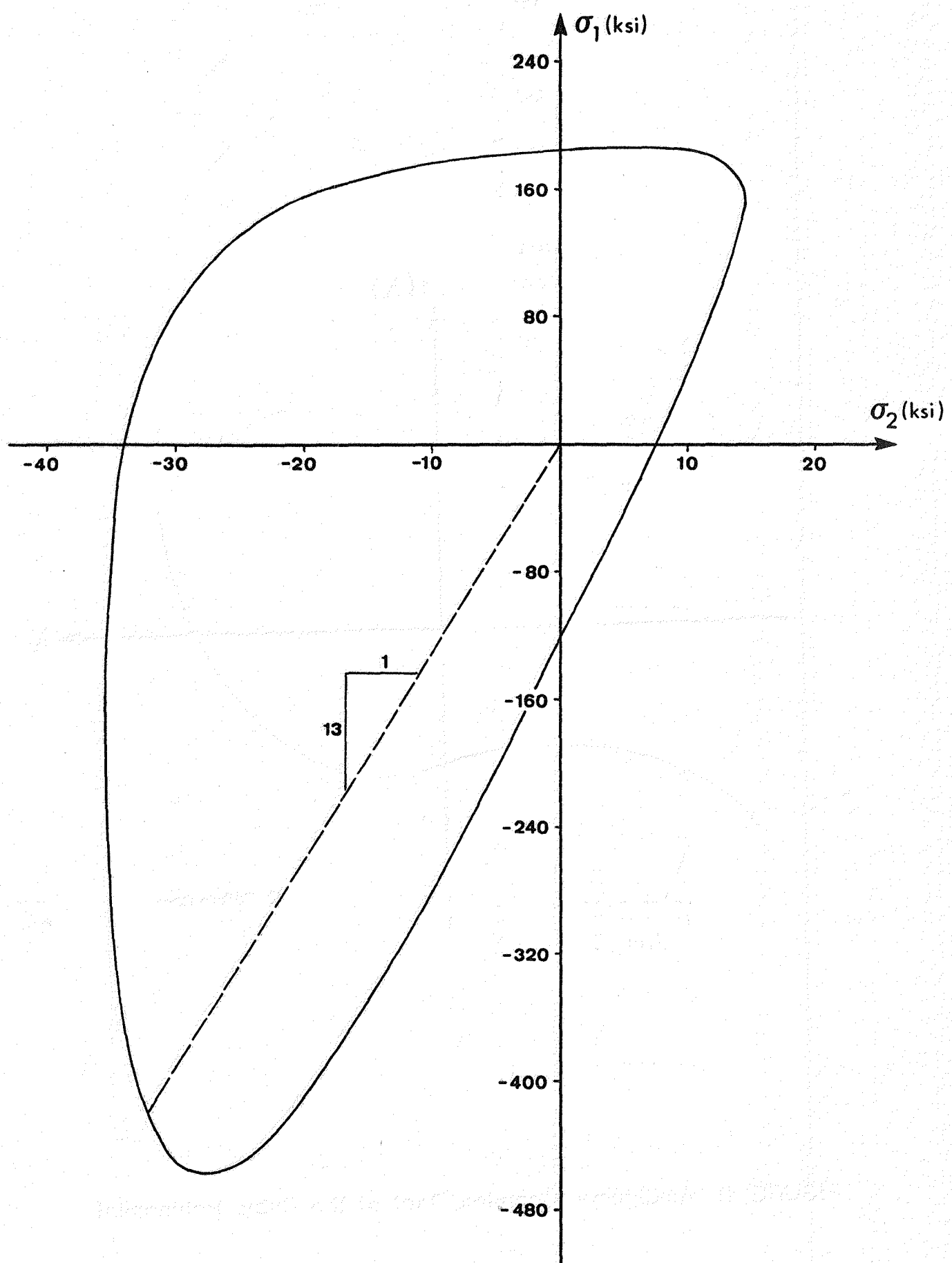


FIGURE 5: Planar Failure Surface from Numerical Experiment

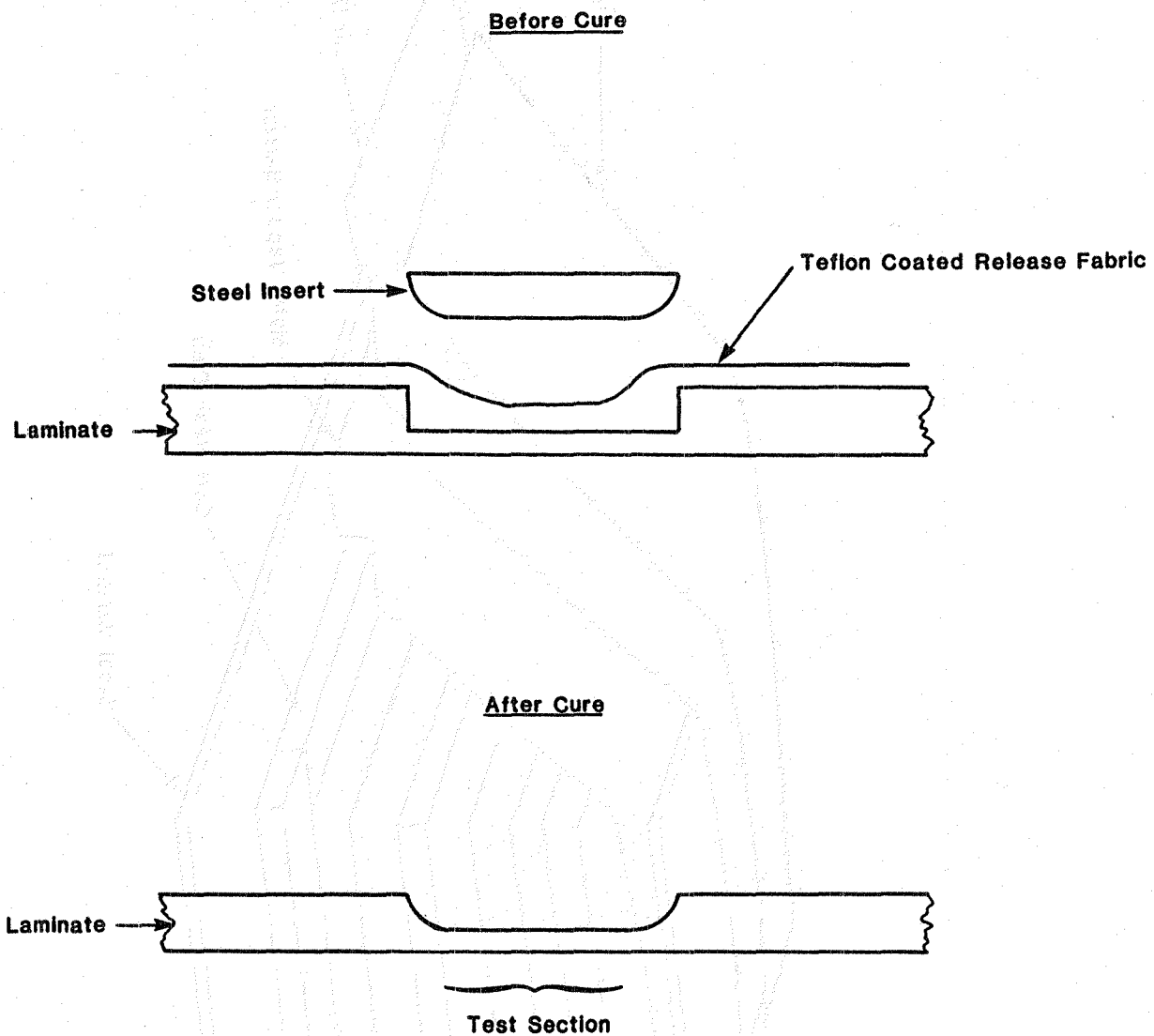


FIGURE 6: Test Section Insert for Fabrication

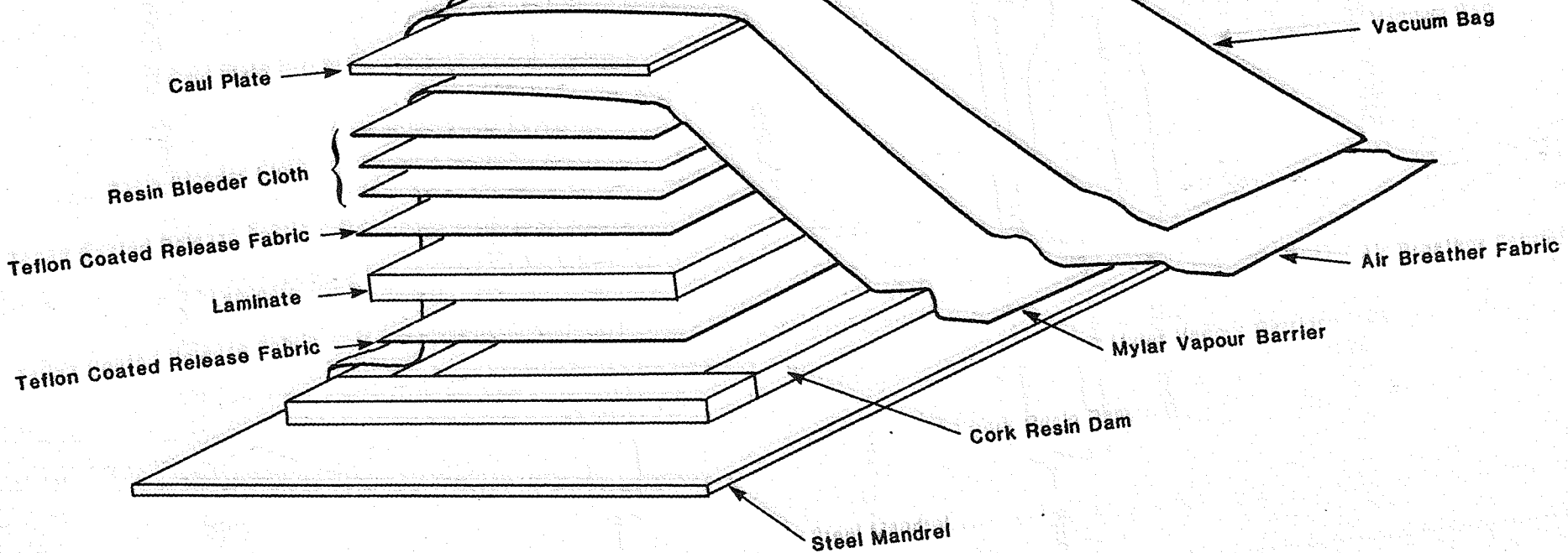


FIGURE 7: Laminate Fabrication Layup

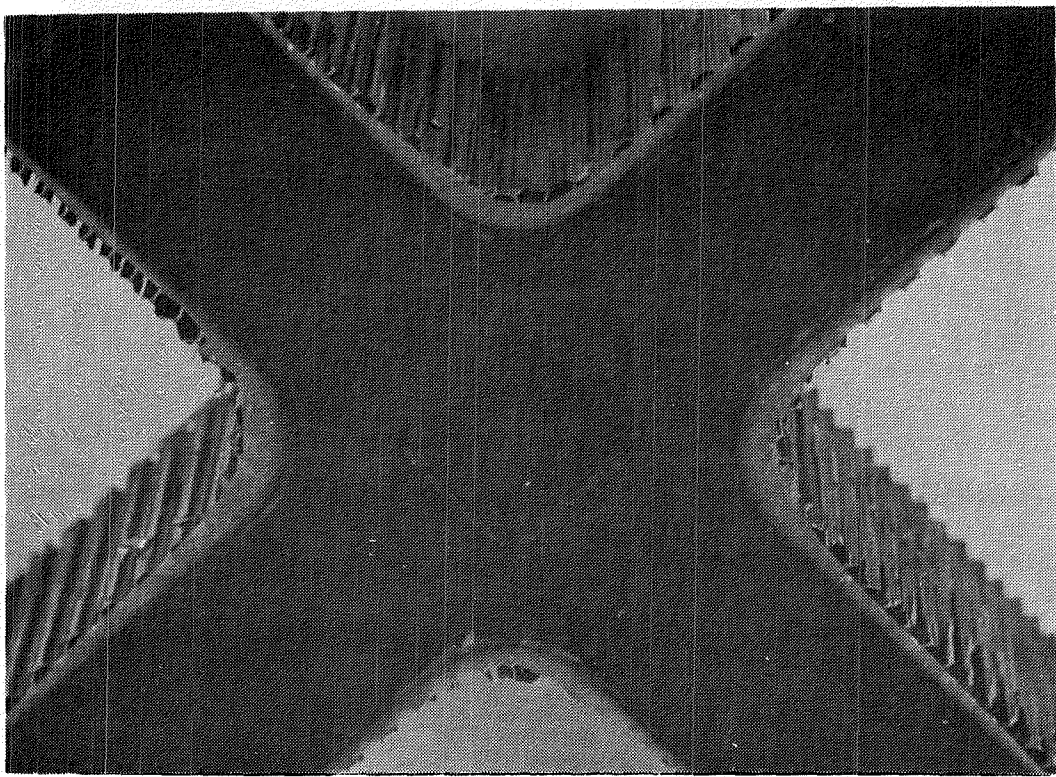


FIGURE 8: Photograph of Cross-Beam GRE Test Section

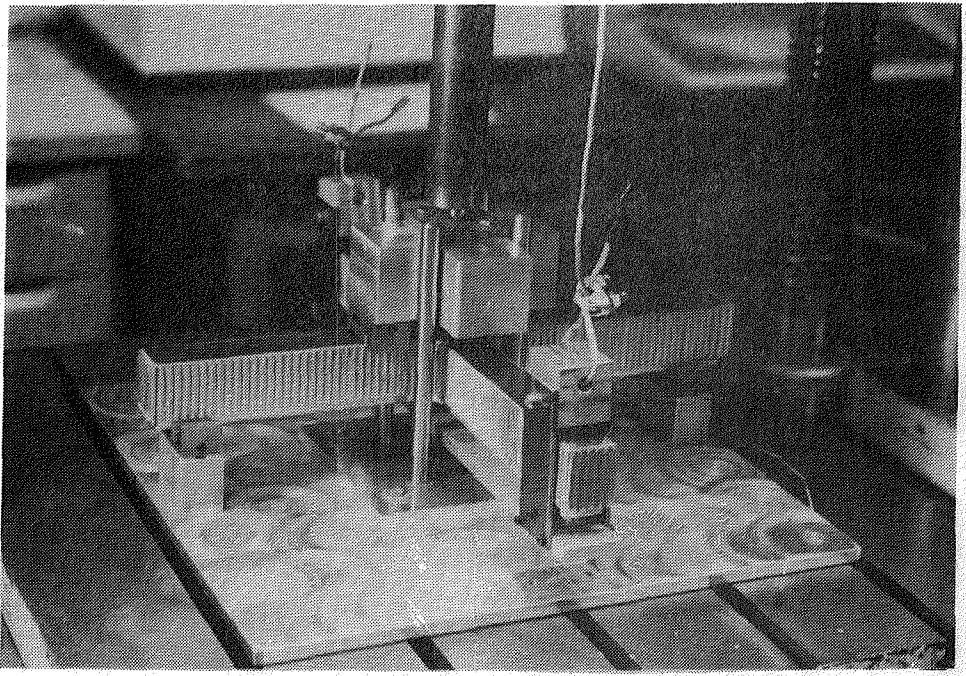


FIGURE 9: Close-Up View of Biaxial Compression Apparatus

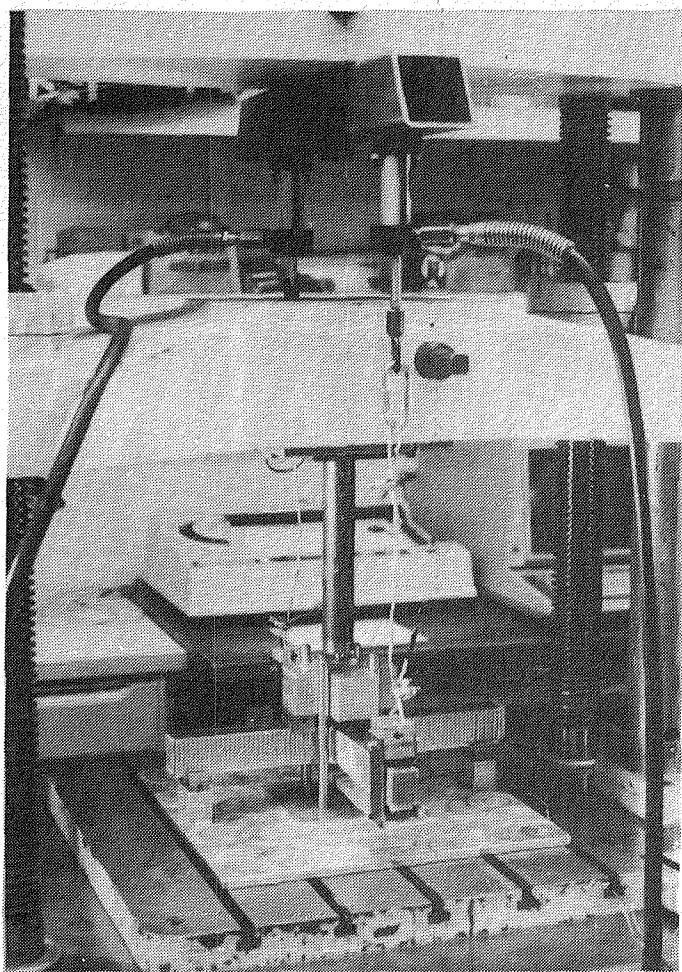


FIGURE 10: Test Set-Up for Biaxial Compression using Dual Independent Loading System

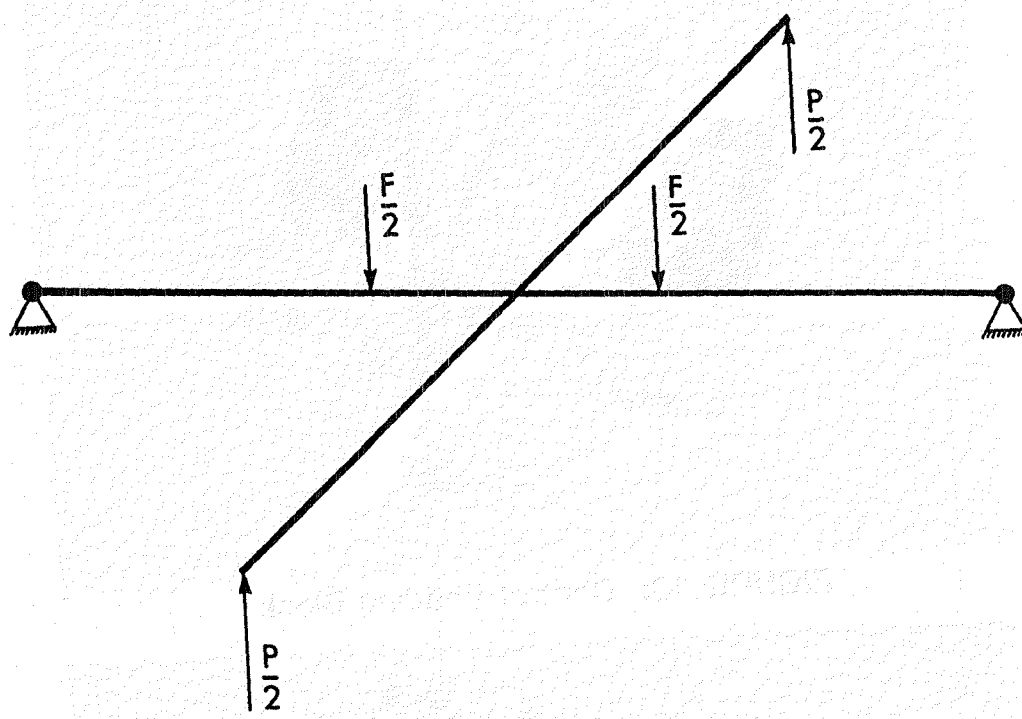


FIGURE 11: Loading Schematic of Cross-Beam

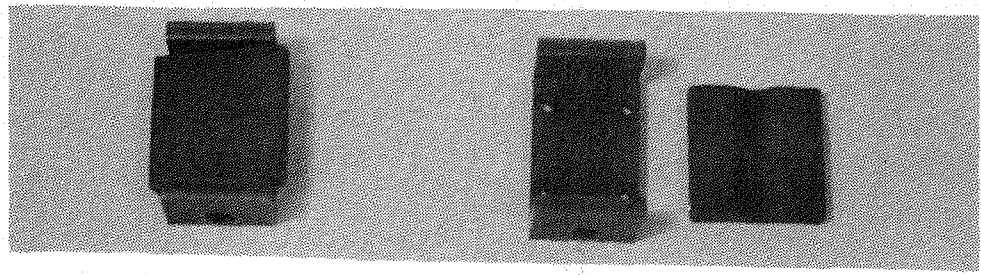


FIGURE 12: Simple Support Pads

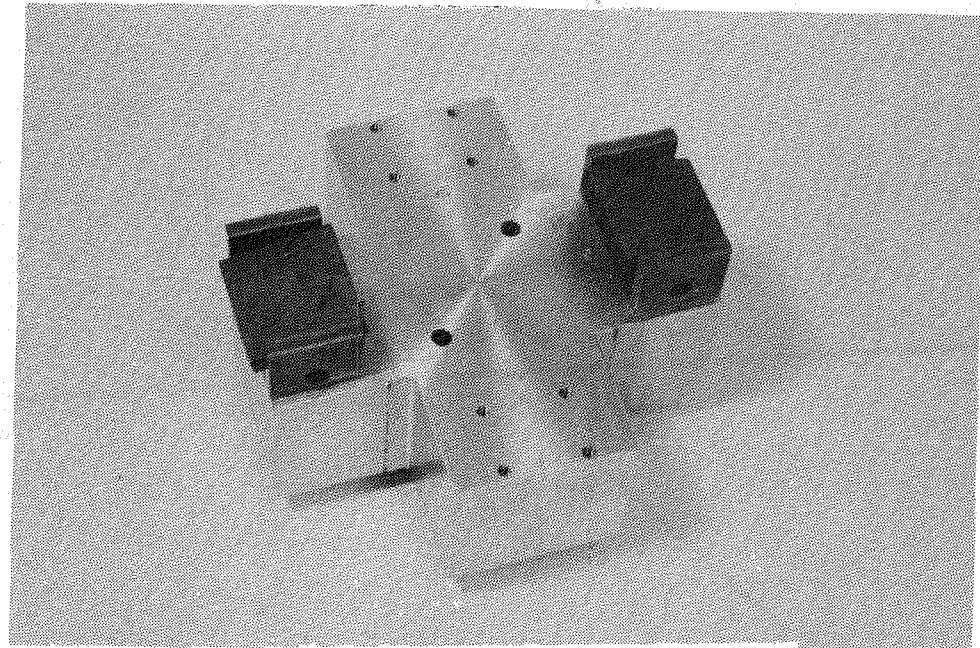


FIGURE 13: Central Loading Block

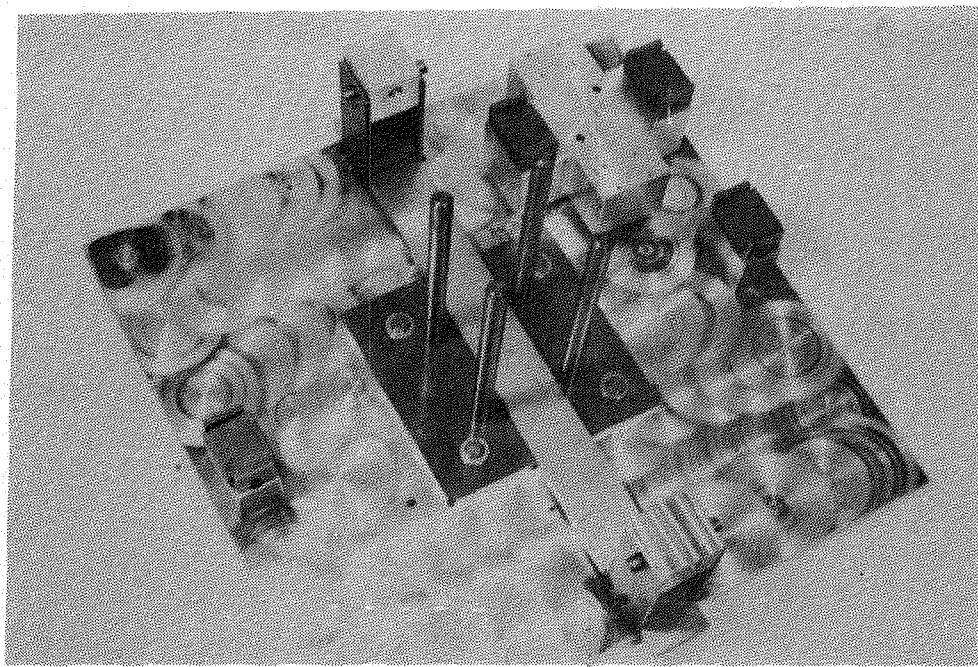


FIGURE 14: Guide Post Arrangement

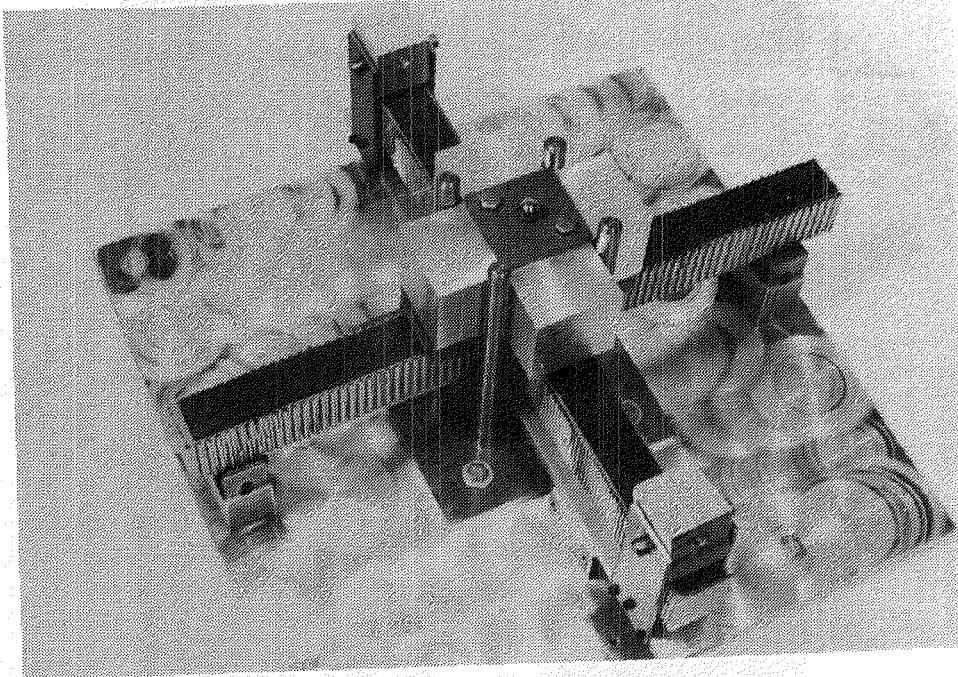
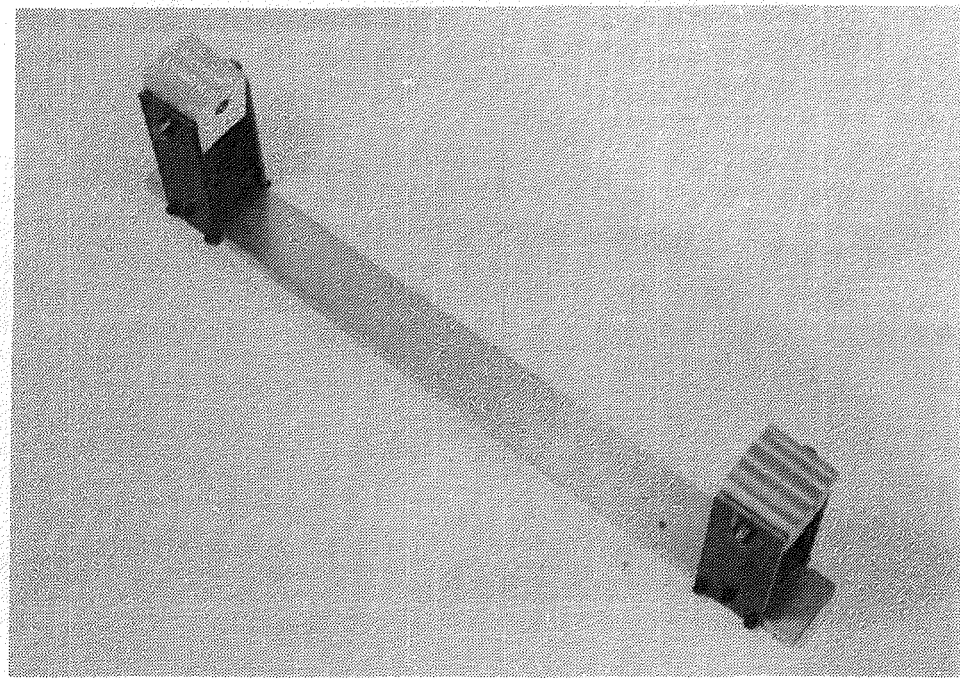


FIGURE 15: Test Setup for Four Point Beam Loading



**FIGURE 16: Load Bar Used for Independent Loading
of Second Beam Arm**

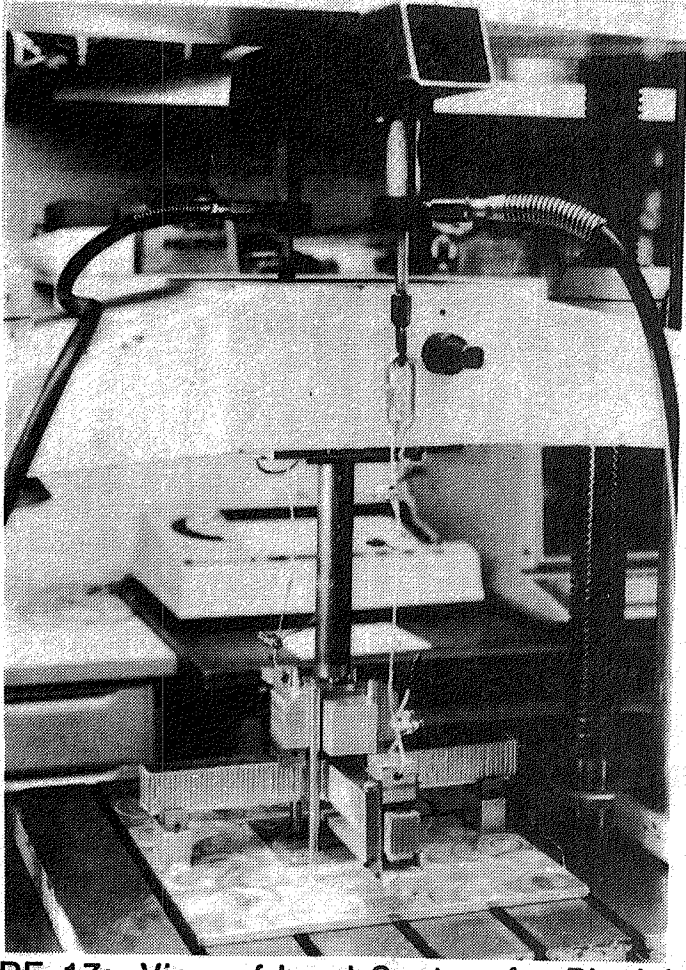


FIGURE 17: View of Load System for Biaxial Test

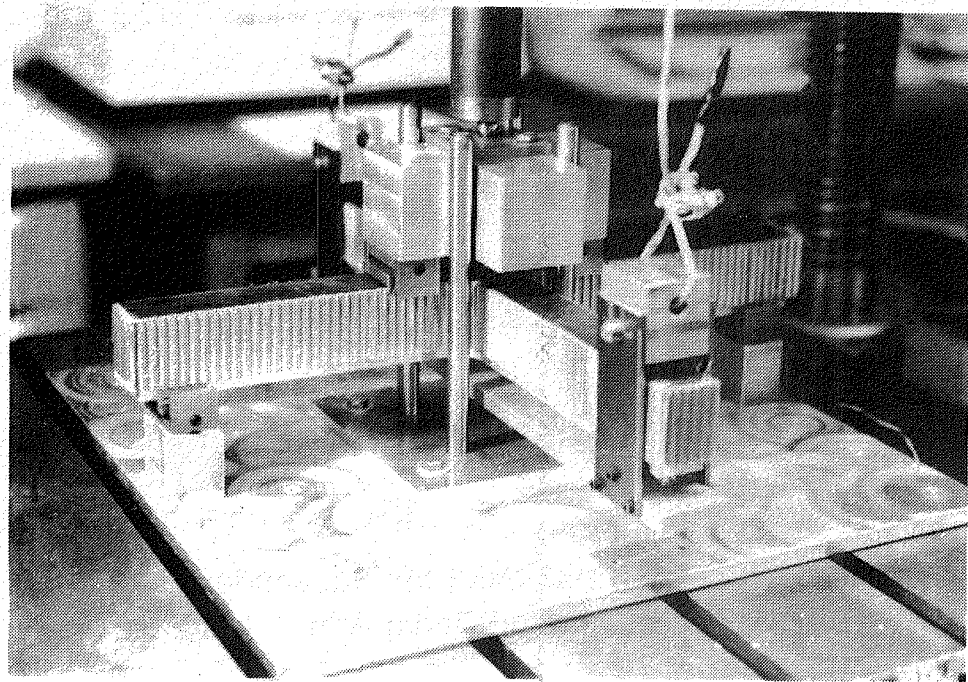


FIGURE 18: Close-Up View of Biaxial Test Rig
with Independent Loading Capability

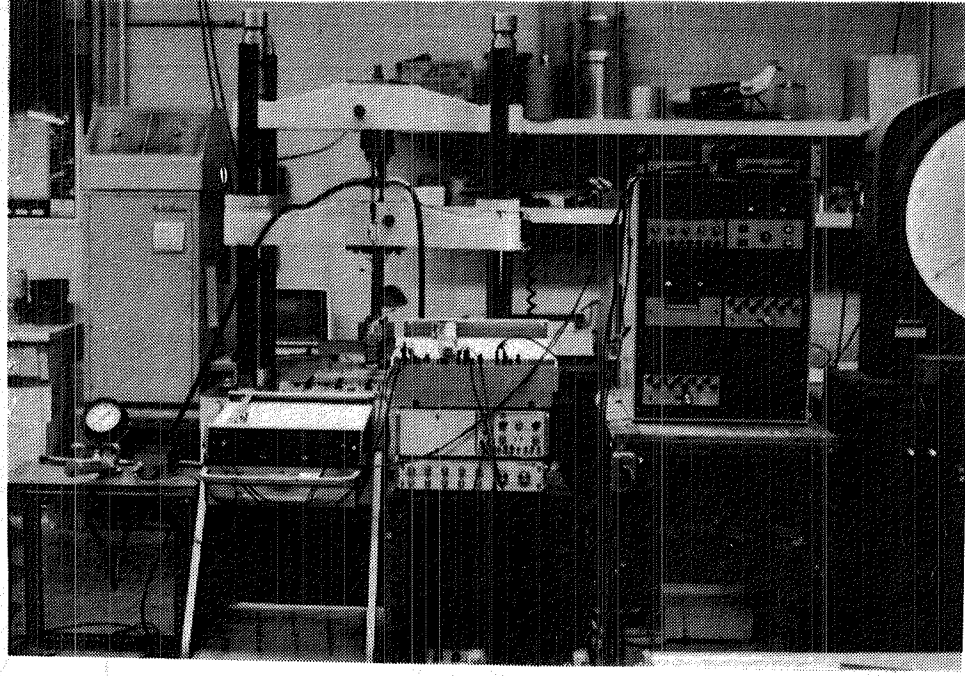


FIGURE 19: Experimental Set-Up for Performing Biaxial Compression Tests

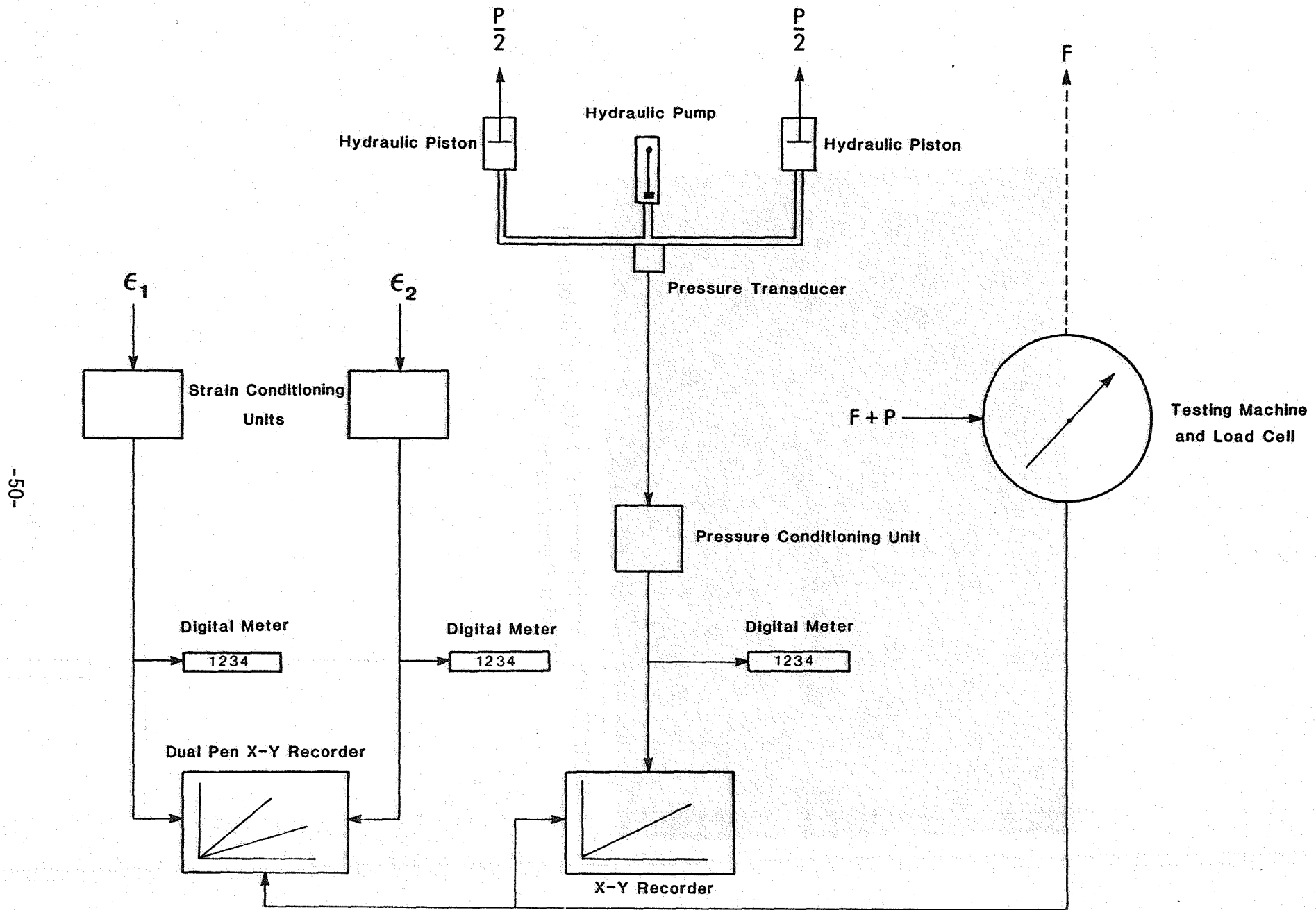


FIGURE 20: Schematic of Experimental Setup

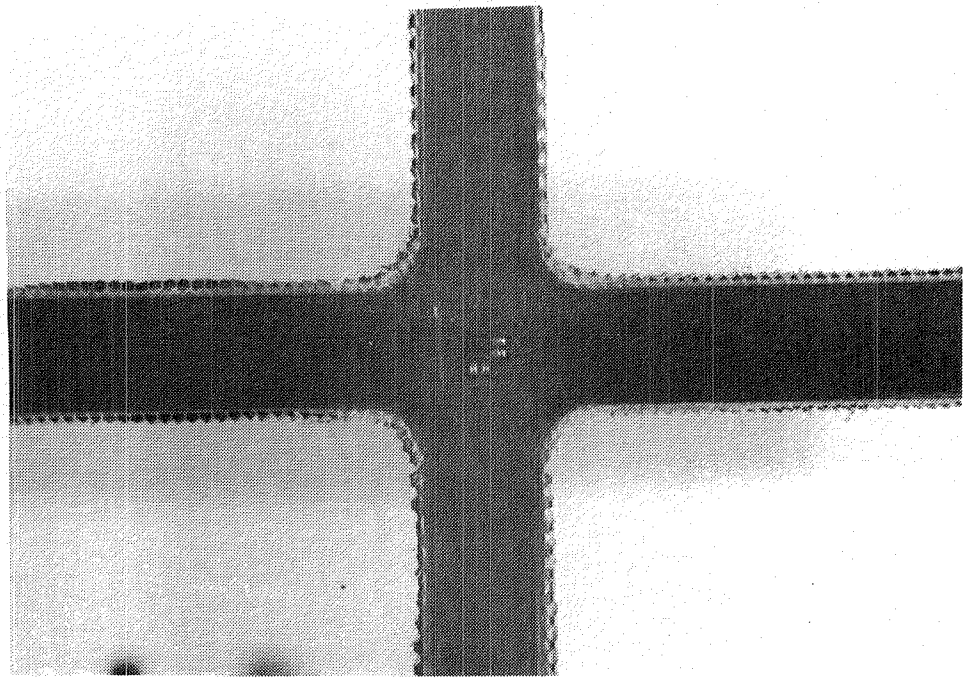


FIGURE 21: Overall View of Failed Test Section in
Biaxial Compression Beam Experiment

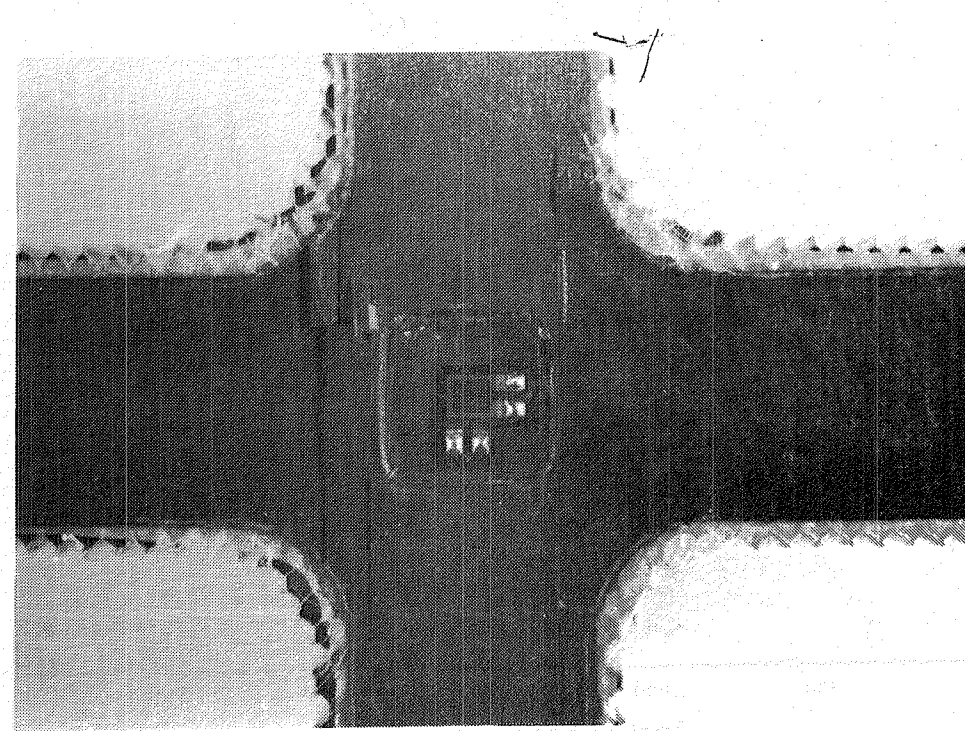


FIGURE 22: Close-Up View of Failed Section
Note: Failure first occurred in test section
and then spread to beam edges .

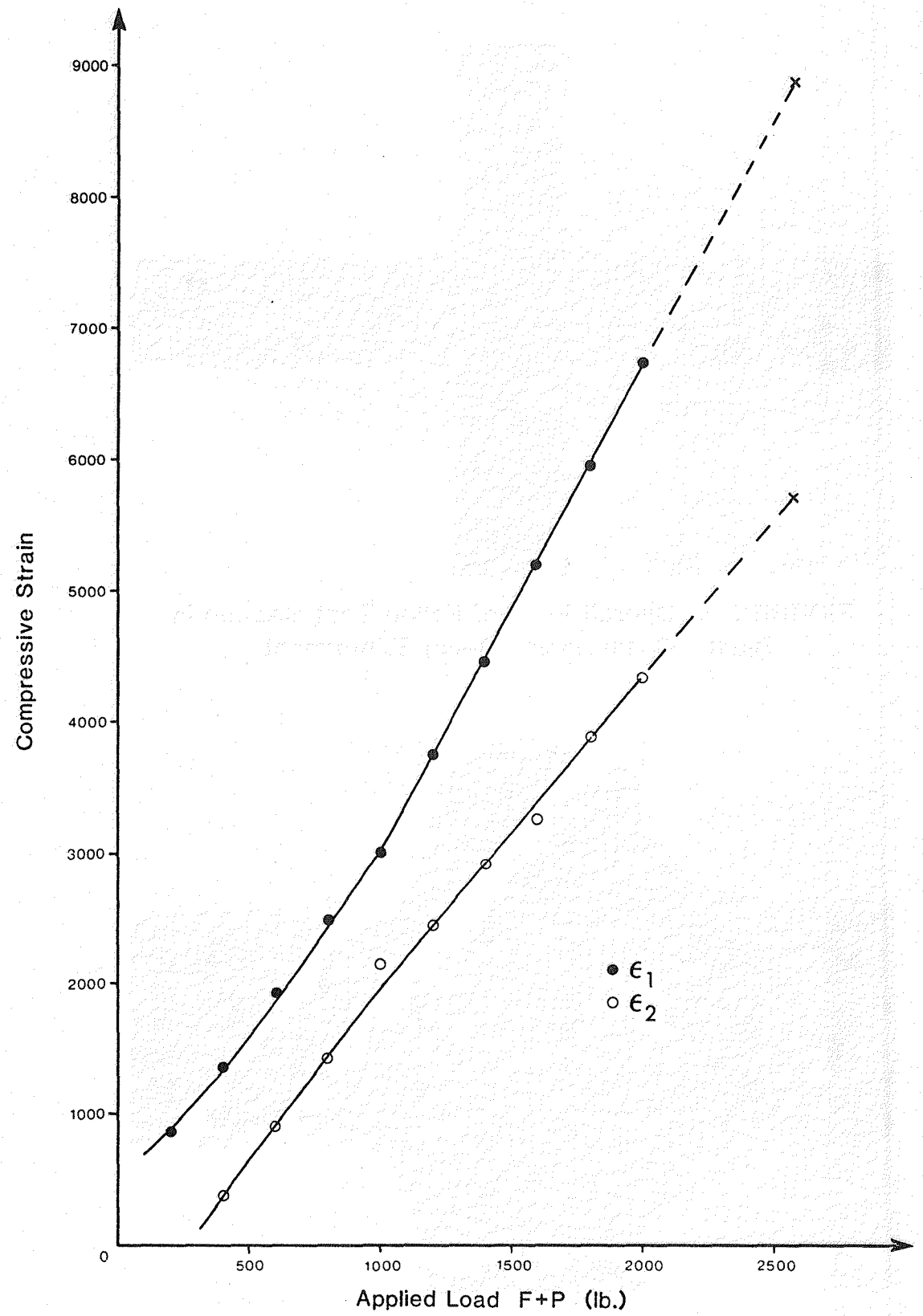


FIGURE 23: Load-Strain Response of Cross-Beam

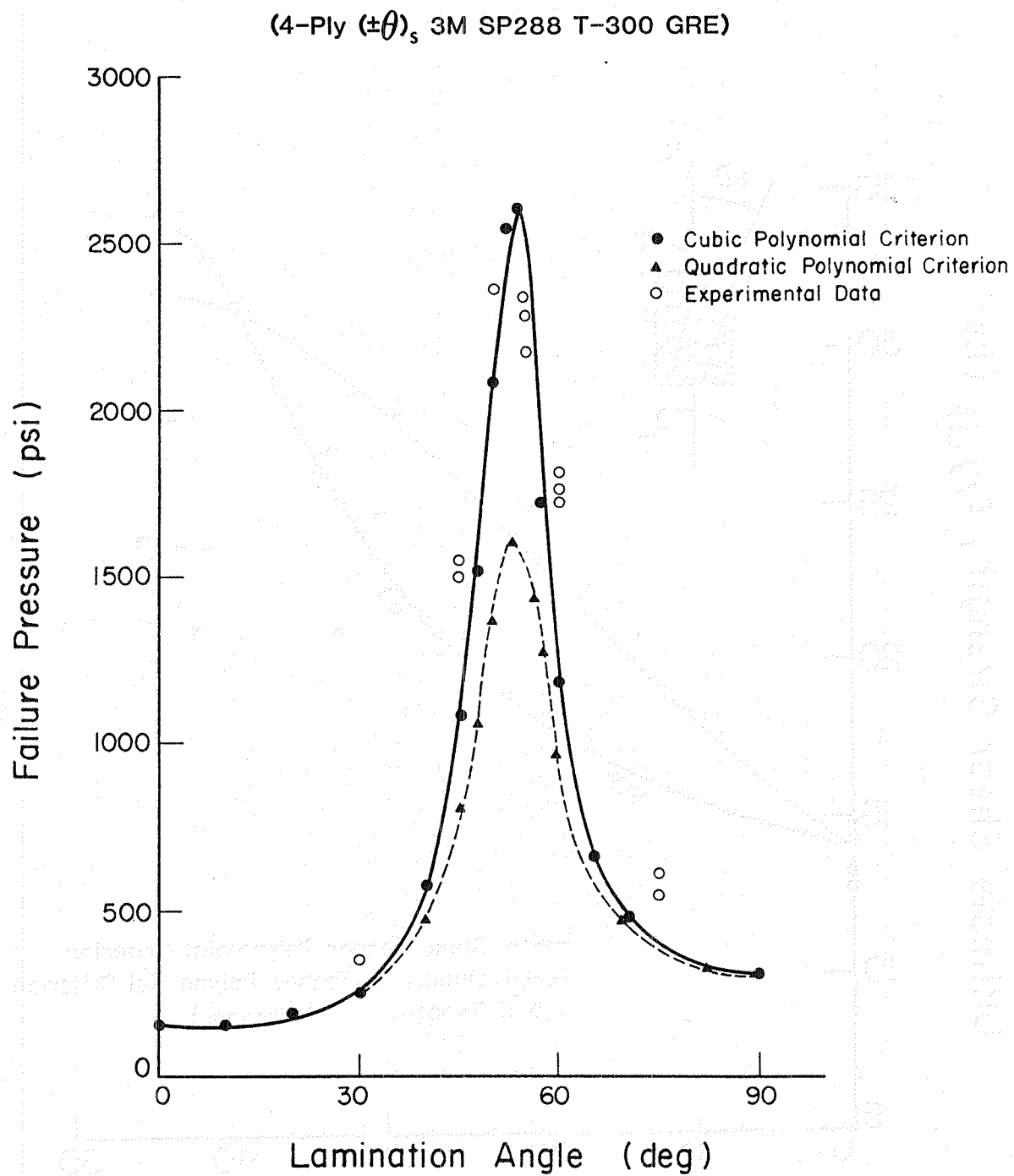


FIGURE 24: Internal Pressure Failure of Symmetric Balanced
Laminated Tubes

(4-Ply SP288 T-300 GRE)

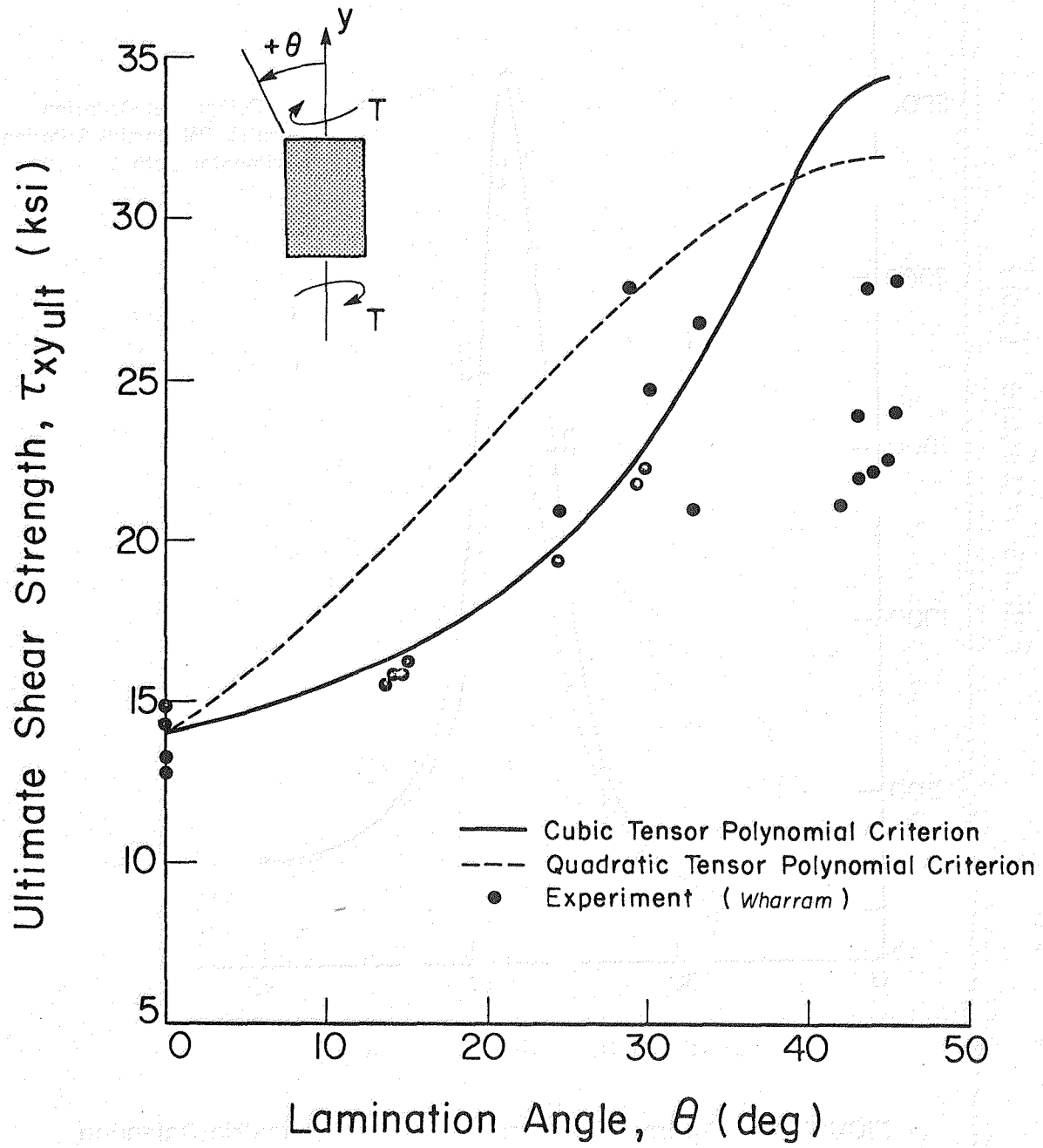


FIGURE 25: Torsional Failure of Off-Axis Laminated Tubes

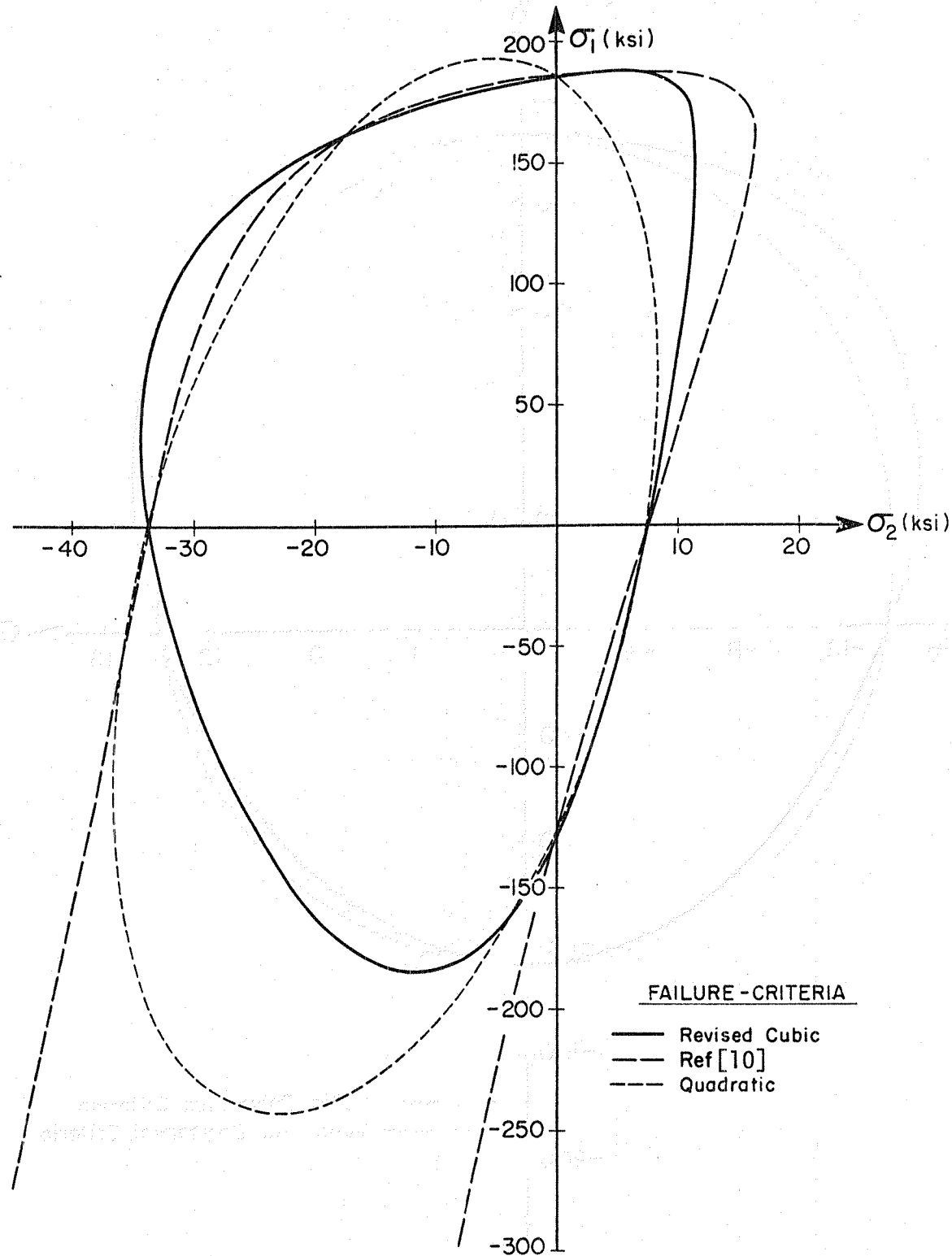


FIGURE 26: Planar Failure Surface, $\sigma_6 = 0$

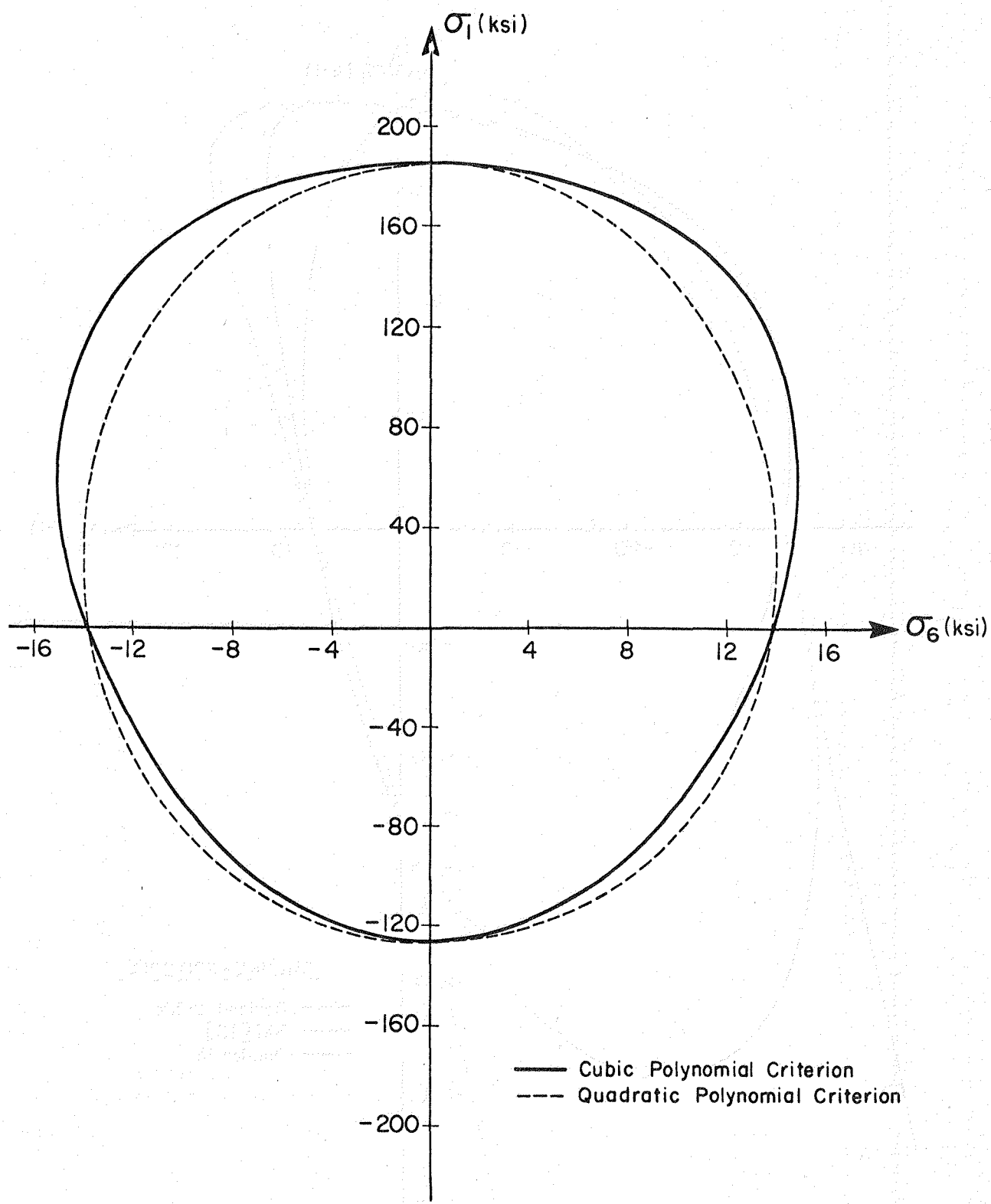


FIGURE 27: Planar Failure Surface, $\sigma_2=0$

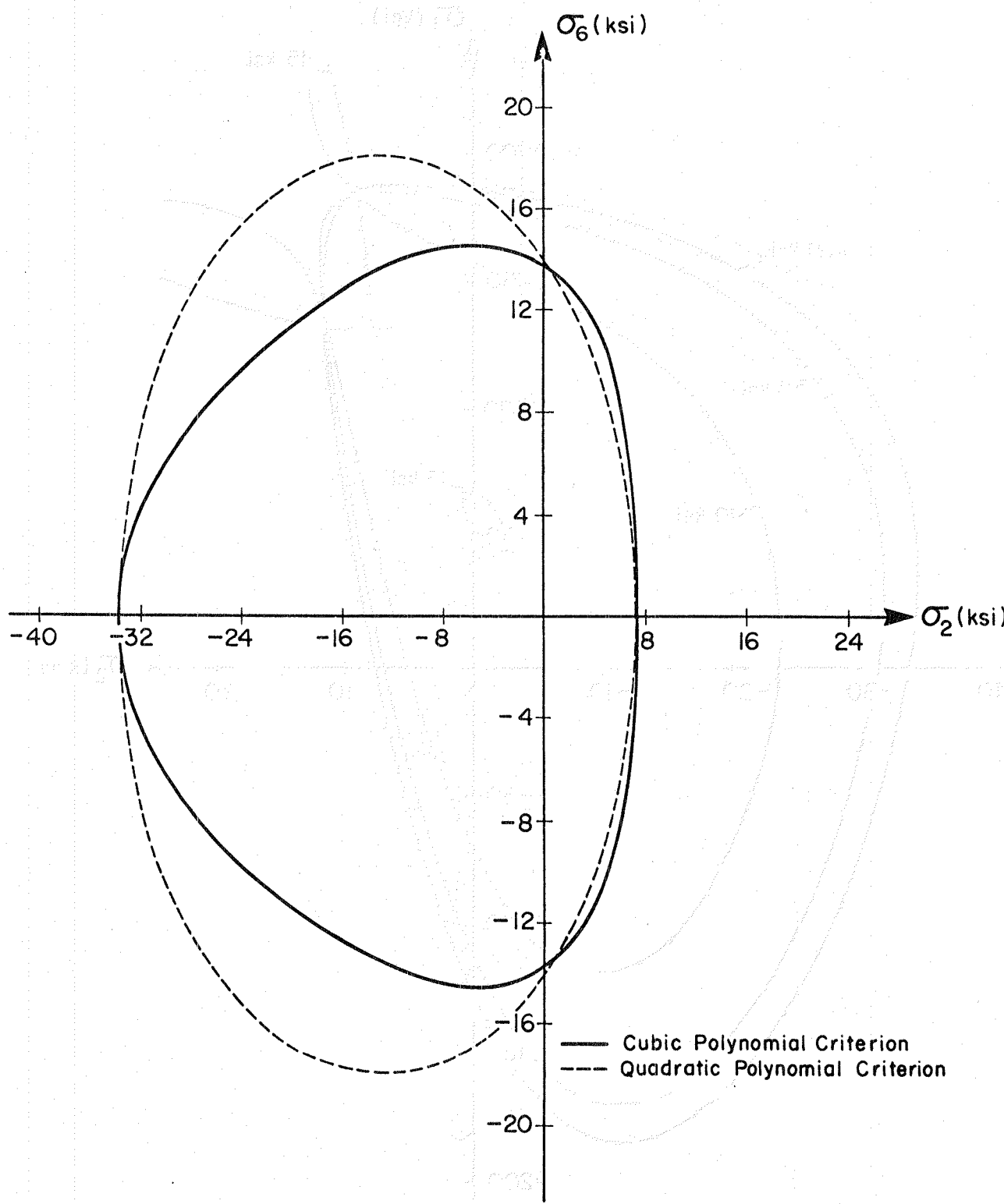


FIGURE 28: Planar Failure Surface, $\sigma_1=0$

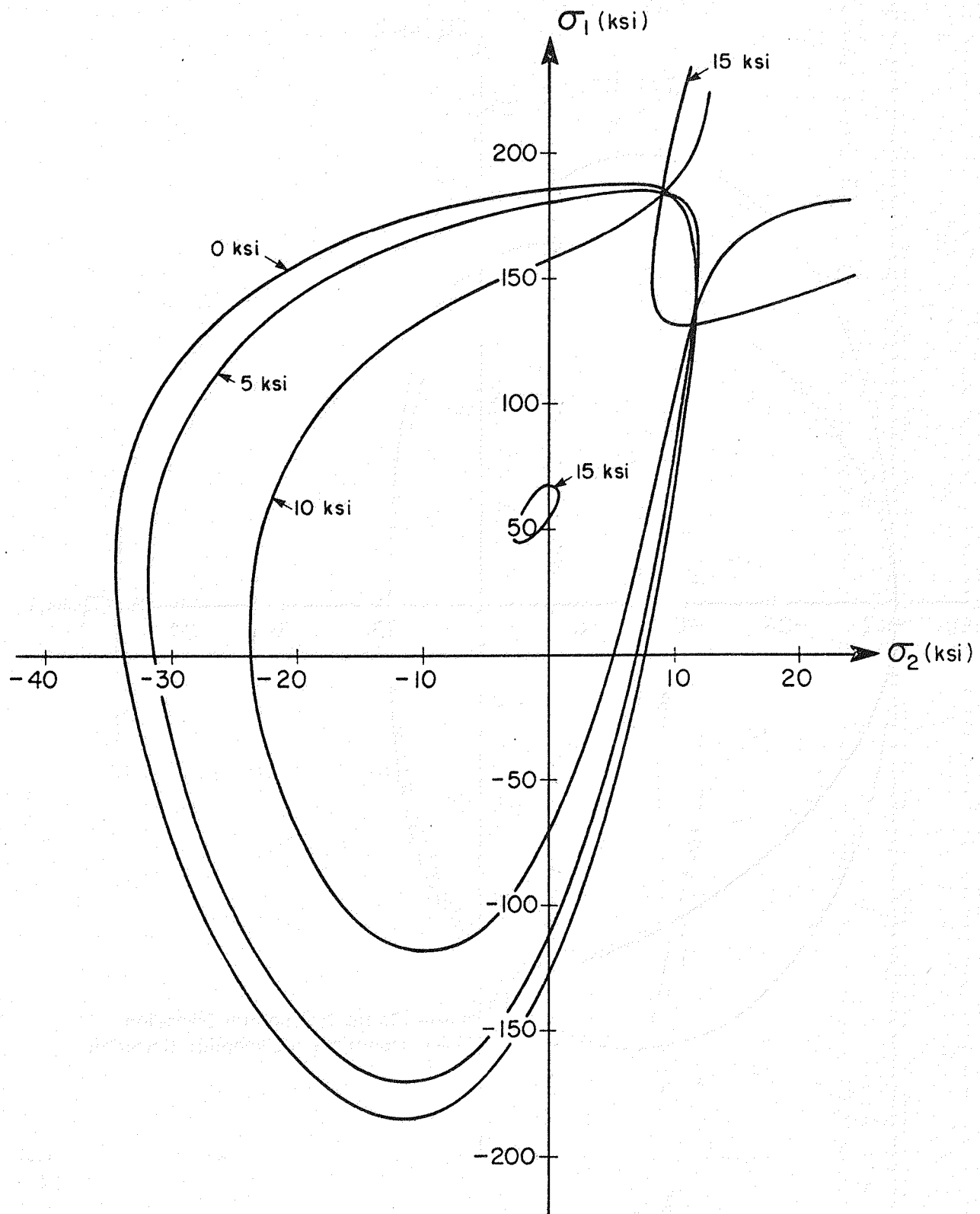


FIGURE 29: Failure Surface Contours for Varying σ_6

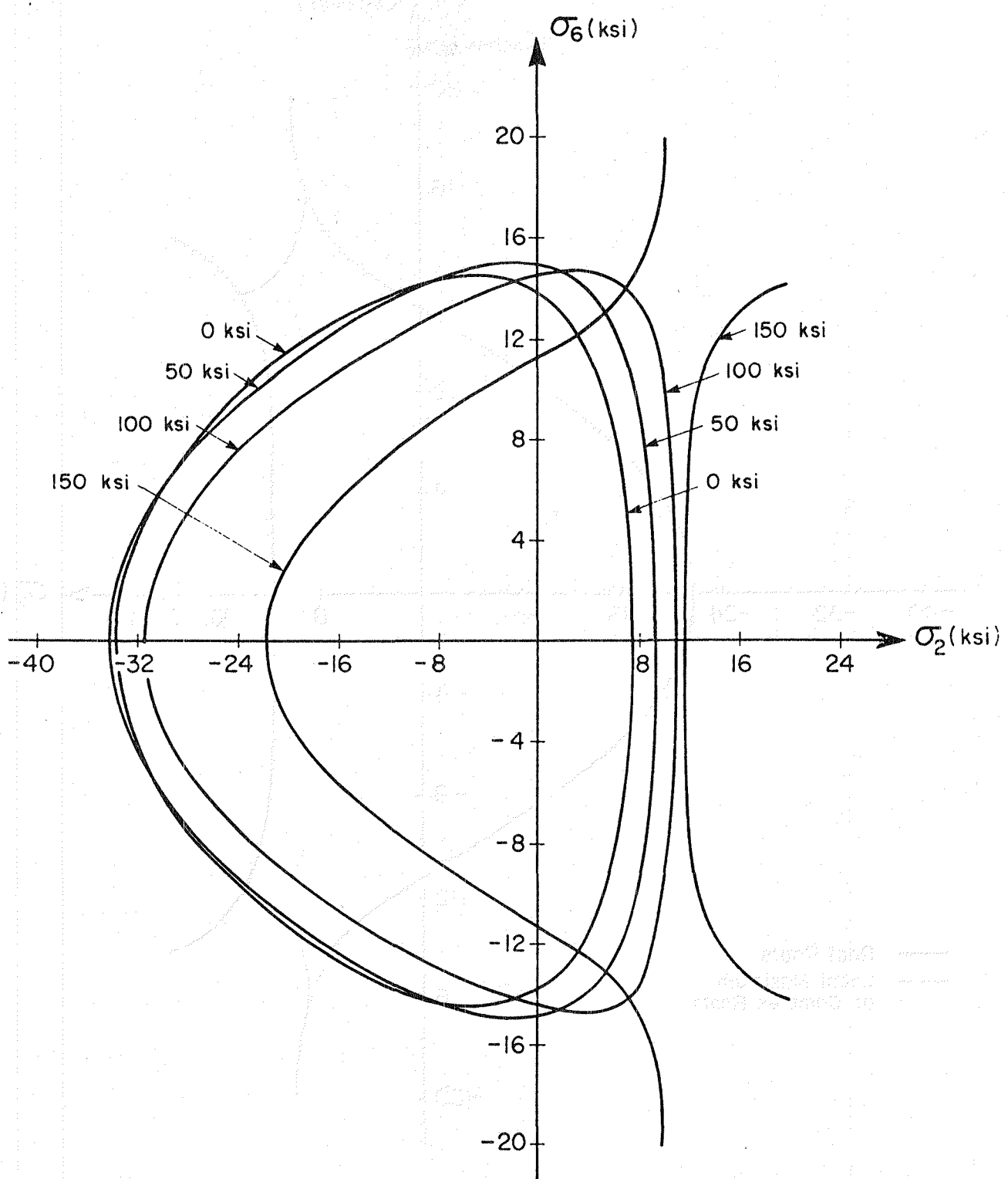


FIGURE 30: Failure Surface Contours for Varying σ_1

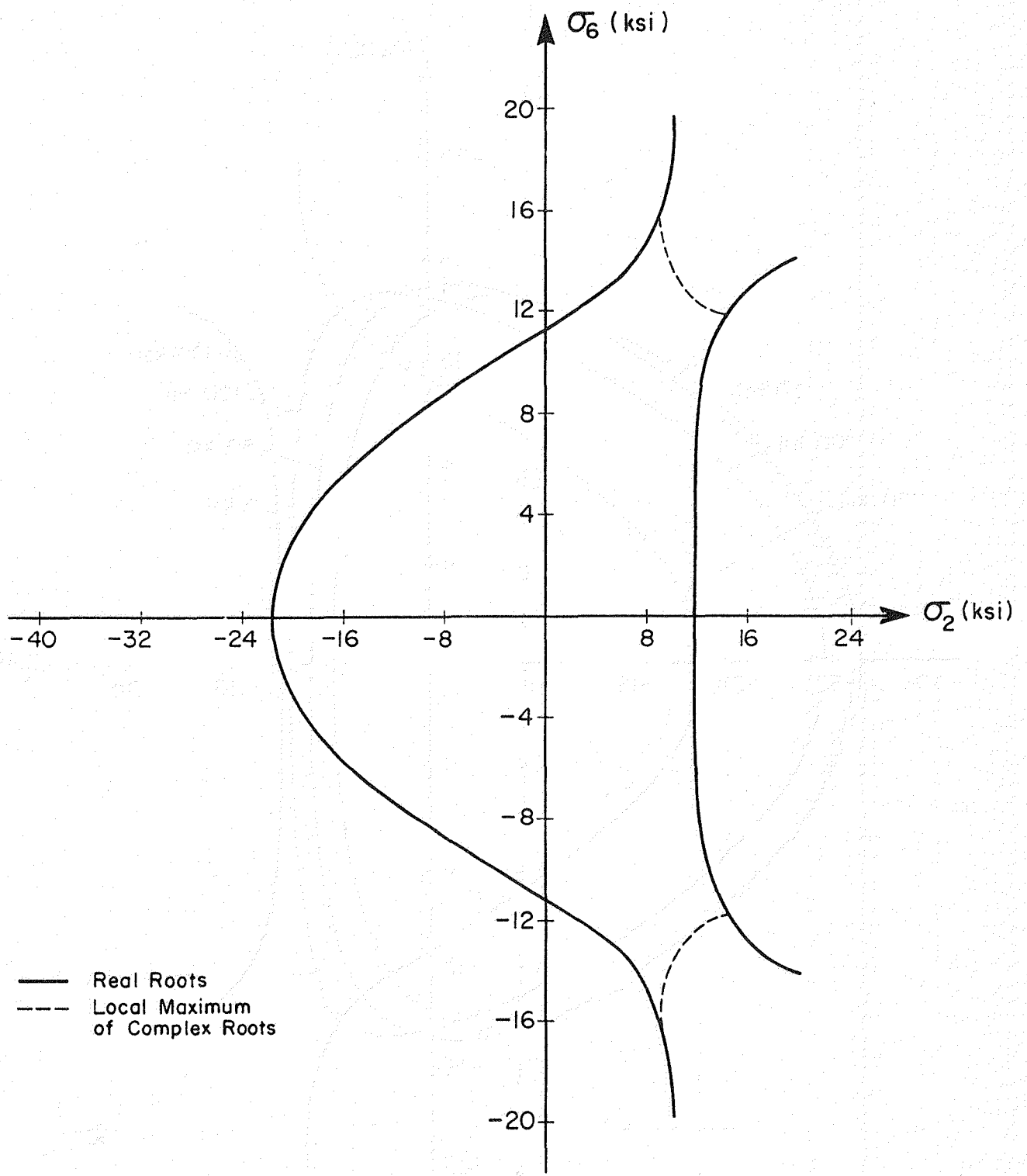


FIGURE 3.1: Planar Failure Surface for $\sigma_1 = 150$ ksi

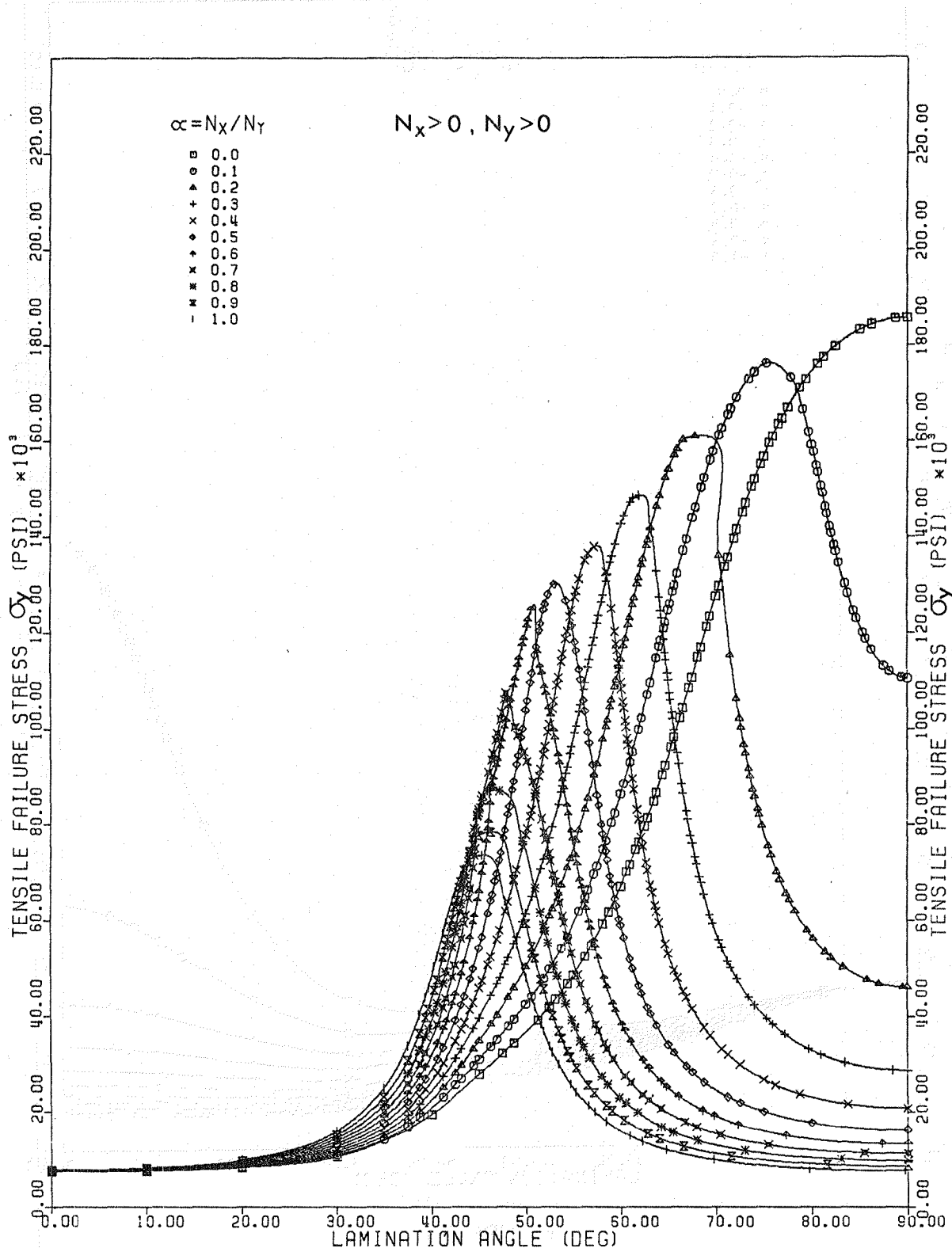


FIGURE 32
 BIAXIAL FAILURE PROFILES FOR $(\pm\theta)_s$ LAMINATES
 [3M SP288-T300 GRE]
 CUBIC TENSOR POLYNOMIAL THEORY

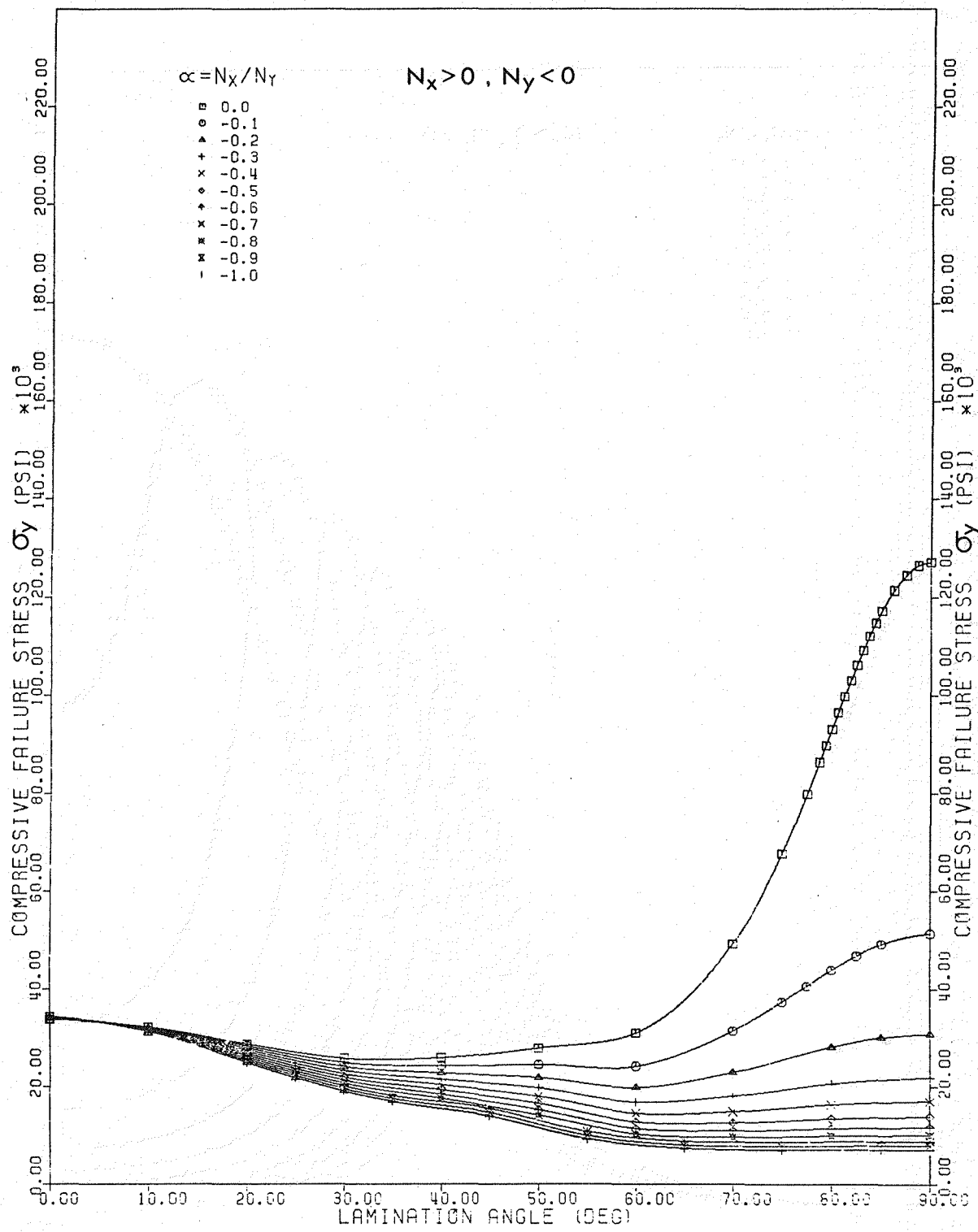


FIGURE 33

BIAXIAL FAILURE PROFILES FOR $(\pm\theta)_s$ LAMINATES
 [3M SP288-T300 GRE] CUBIC TENSOR POLYNOMIAL THEORY

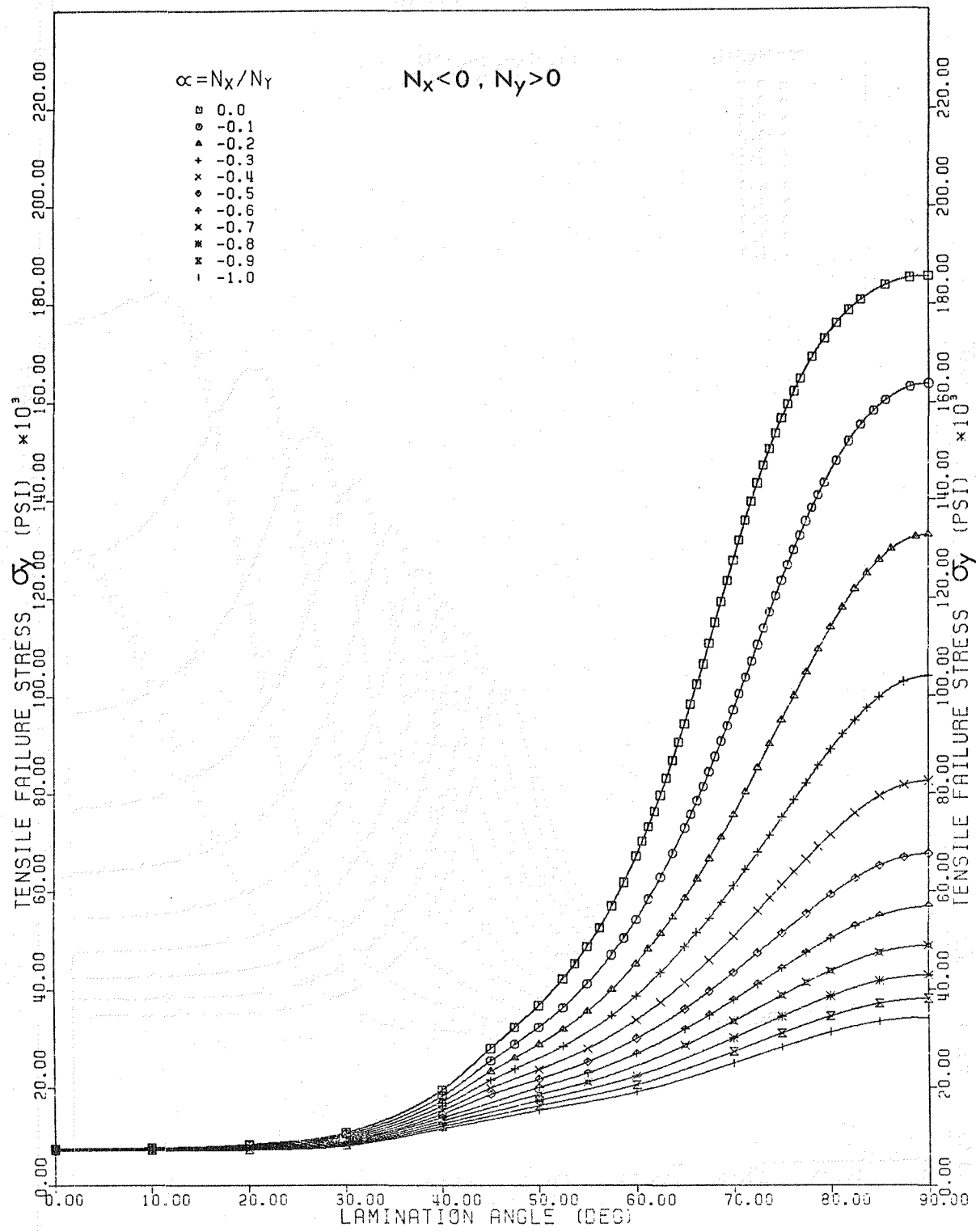


FIGURE 34
 BIAXIAL FAILURE PROFILES FOR $(\pm\theta)_s$ LAMINATES
 [3M SP288-T300 GRE]
 CUBIC TENSOR POLYNOMIAL THEORY

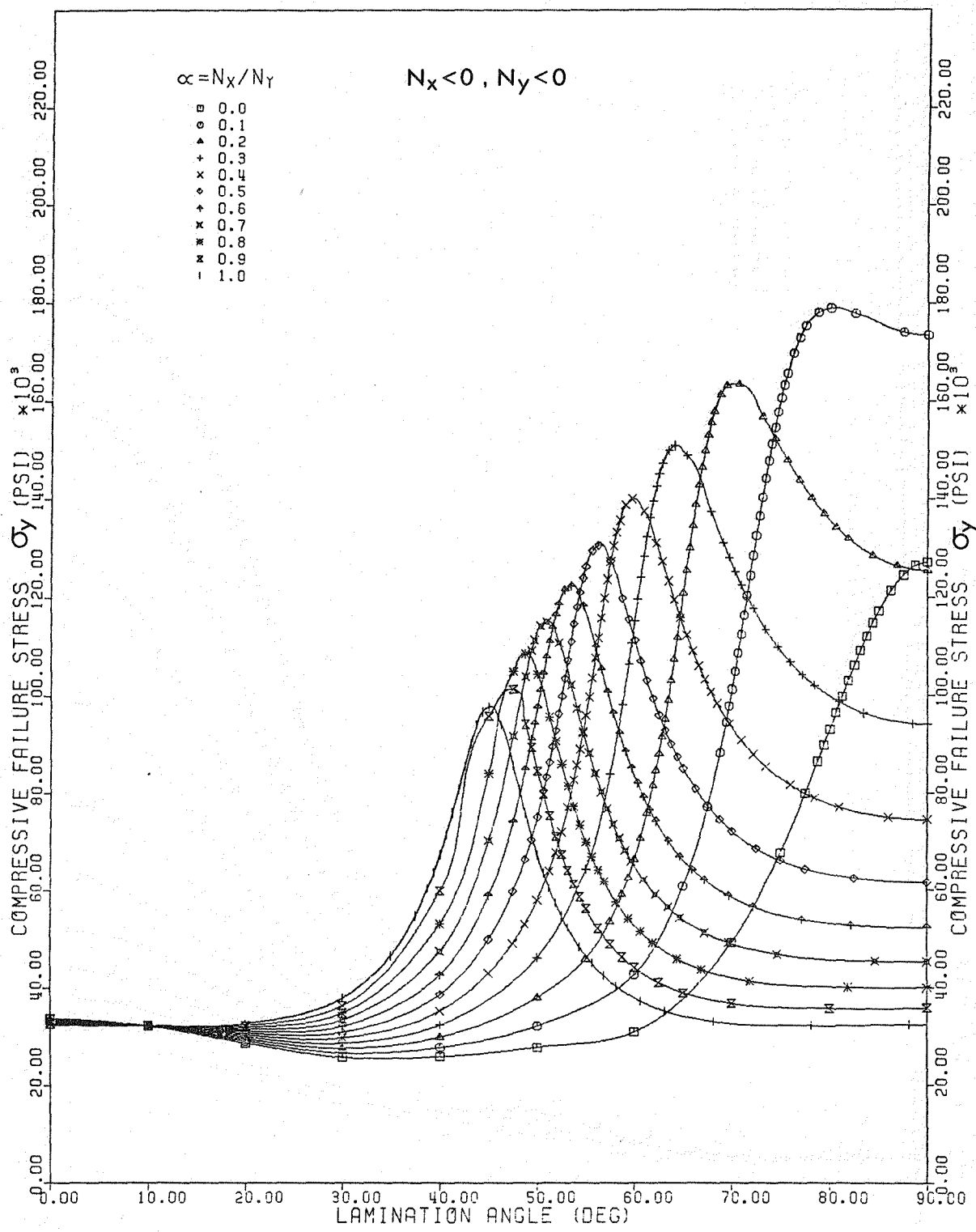


FIGURE 35
BIAXIAL FAILURE PROFILES FOR $(\pm\theta)_s$ LAMINATES
[3M SP288-T300 GRE]
CUBIC TENSOR POLYNOMIAL THEORY

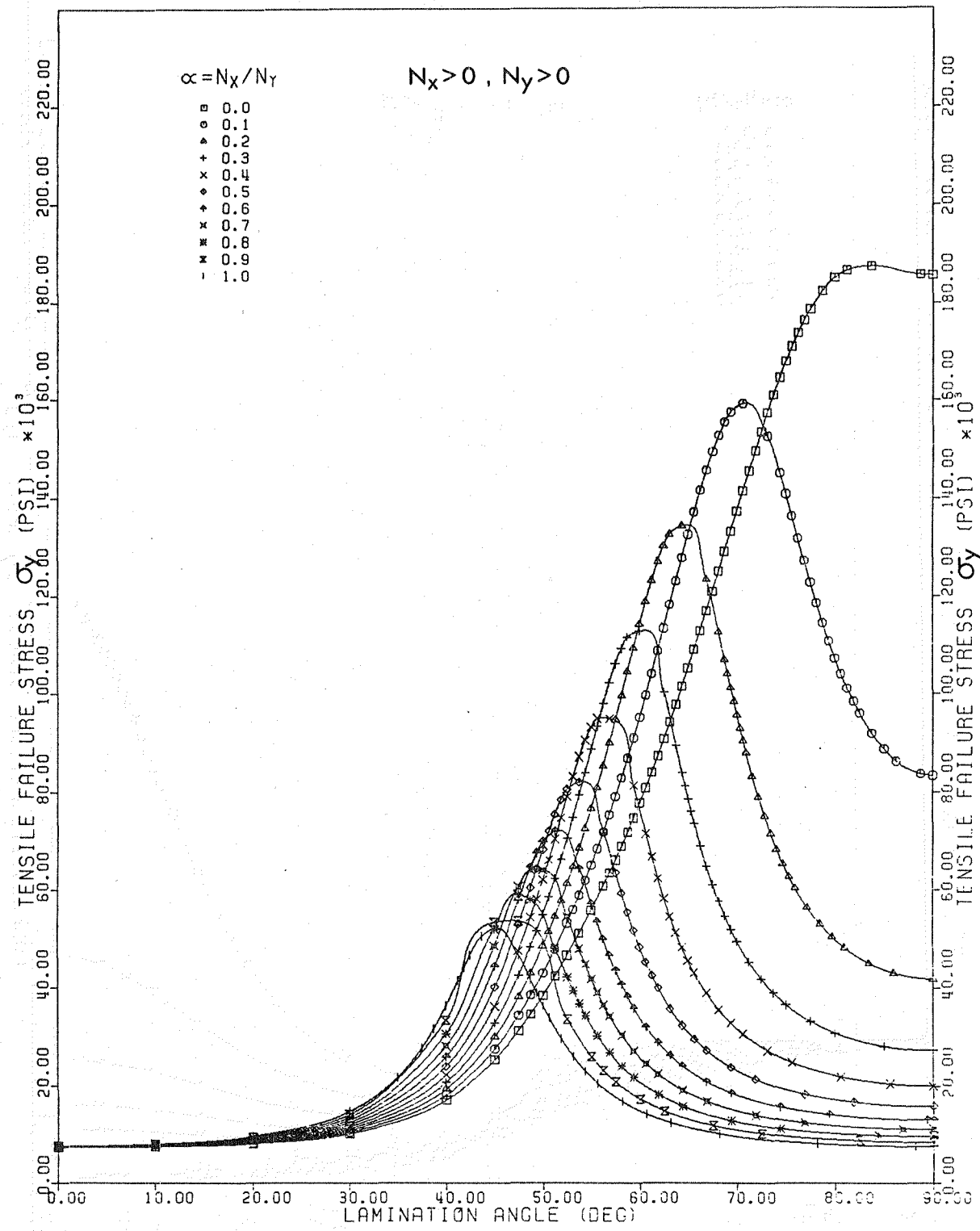


FIGURE 36
 BIAXIAL FAILURE PROFILES FOR $(\pm\theta)_s$ LAMINATES
 [3M SP288-T300 GRE]
 QUADRATIC TENSOR POLYNOMIAL THEORY

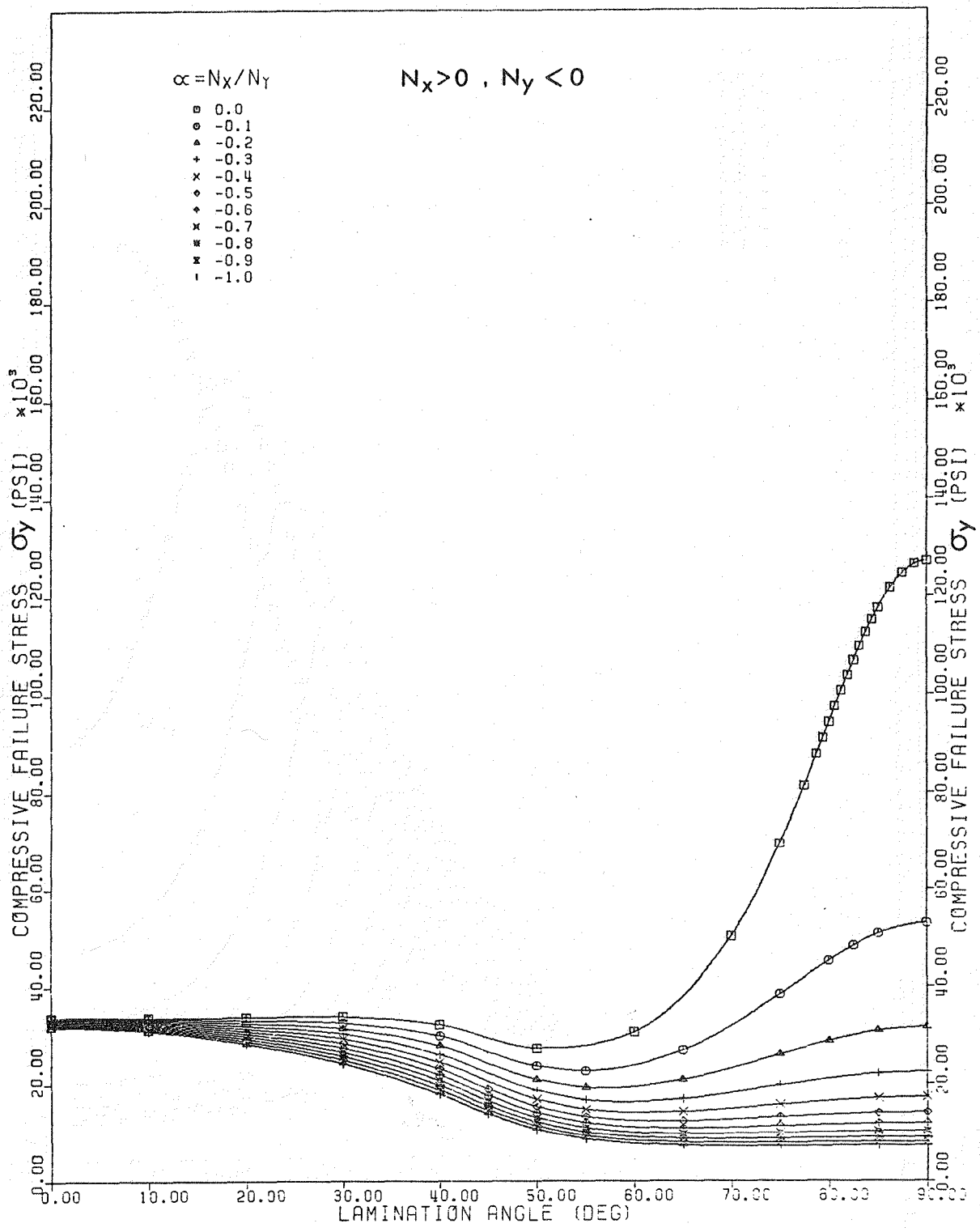


FIGURE 37

BIAXIAL FAILURE PROFILES FOR $(\pm\theta)_s$ LAMINATES

[3M SP288-T300 GRE]

QUADRATIC TENSOR POLYNOMIAL THEORY

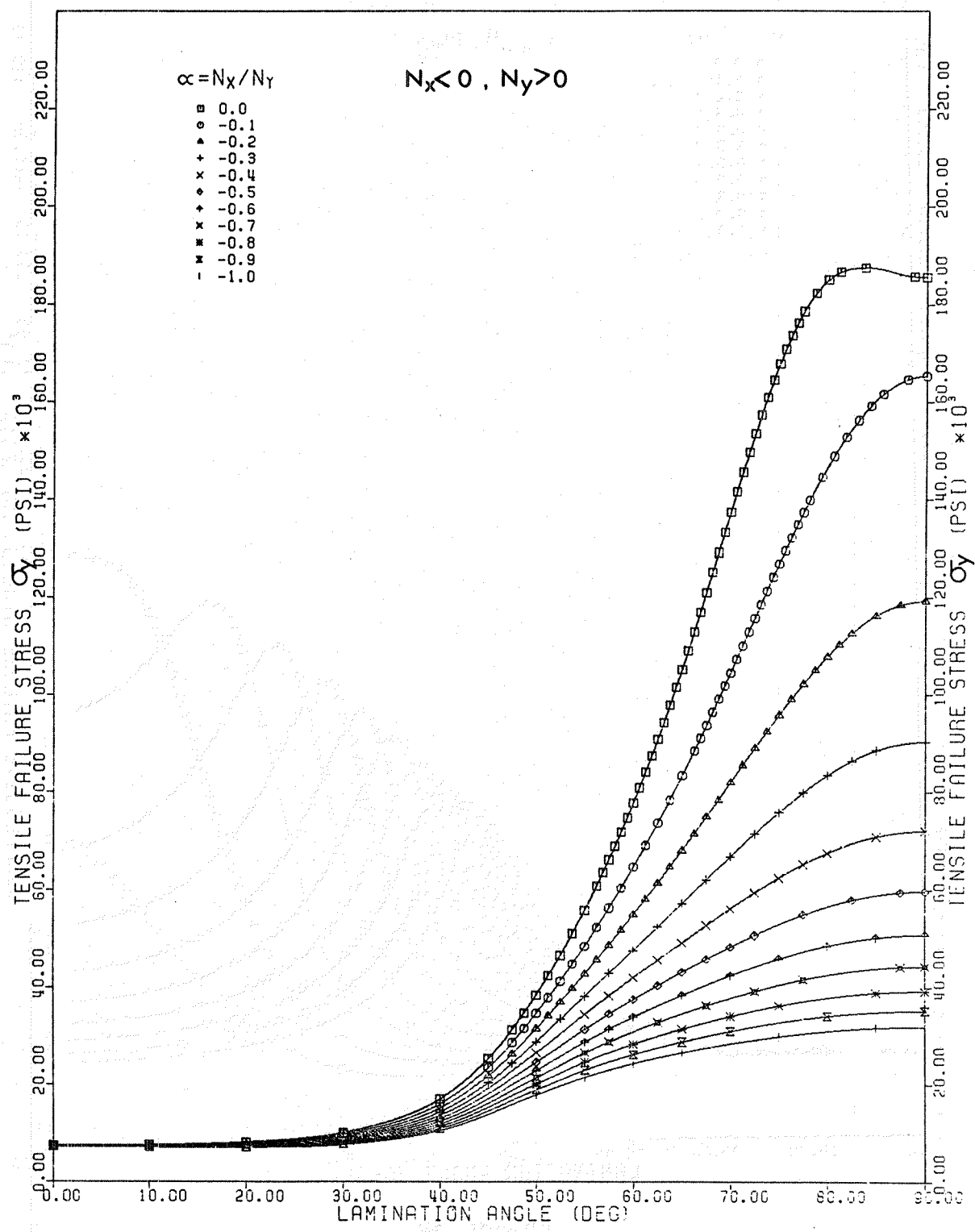


FIGURE 38
 BIAXIAL FAILURE PROFILES FOR $(\pm\theta)_s$ LAMINATES
 [3M SP288-T300 GRE] ALUMINUM
 QUADRATIC TENSOR POLYNOMIAL THEORY

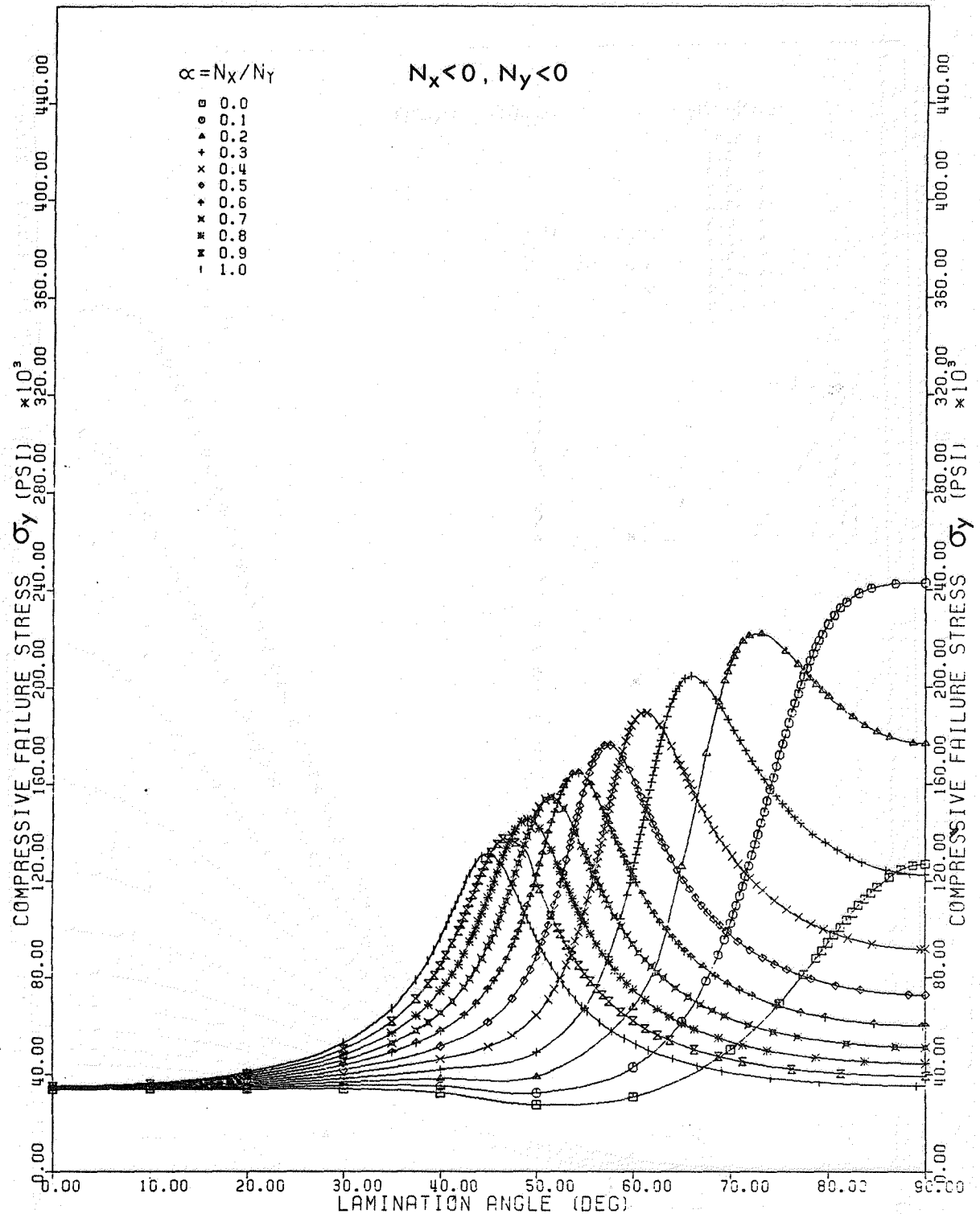


FIGURE 39
BIAXIAL FAILURE PROFILES FOR $(\pm\theta)_s$ LAMINATES
[3M SP288-T300 GRE]
QUADRATIC TENSOR POLYNOMIAL THEORY

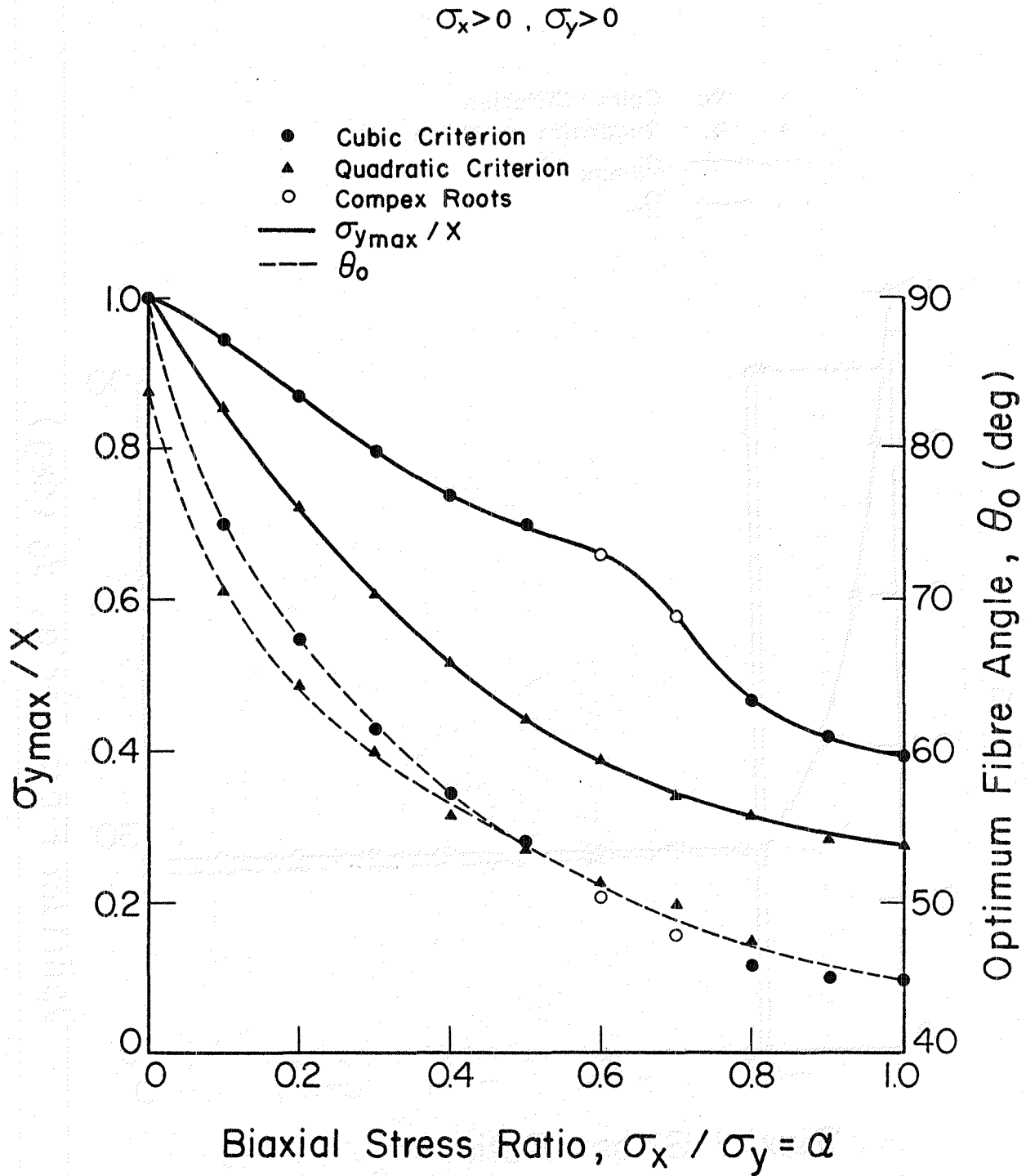


FIGURE 40: Locus of Maximum Strength and Optimum Fiber Angle for Symmetric Balanced Laminates

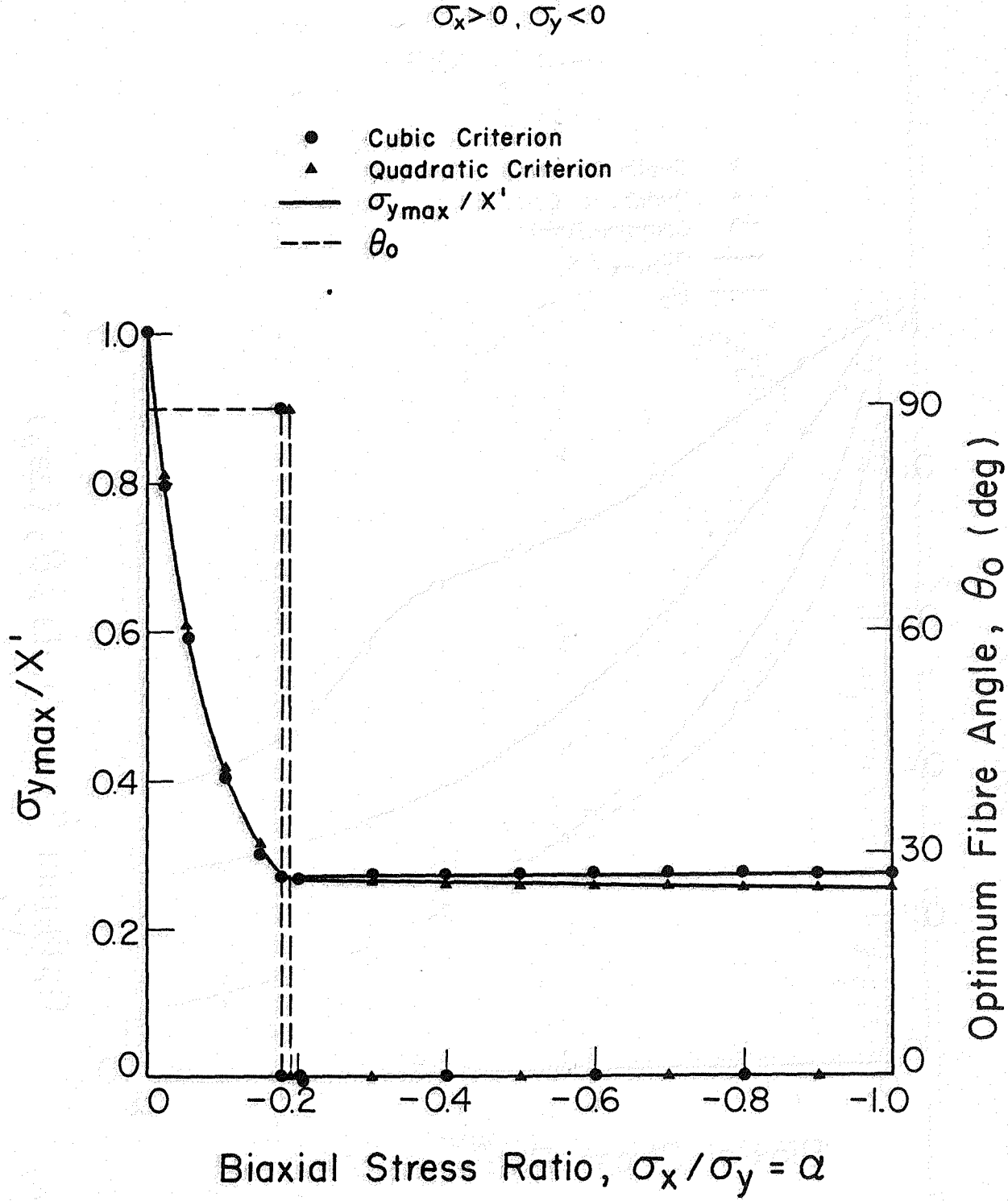


FIGURE 4.1: Locus of Maximum Strength and Optimum Fiber Angle for Symmetric Balanced Laminates

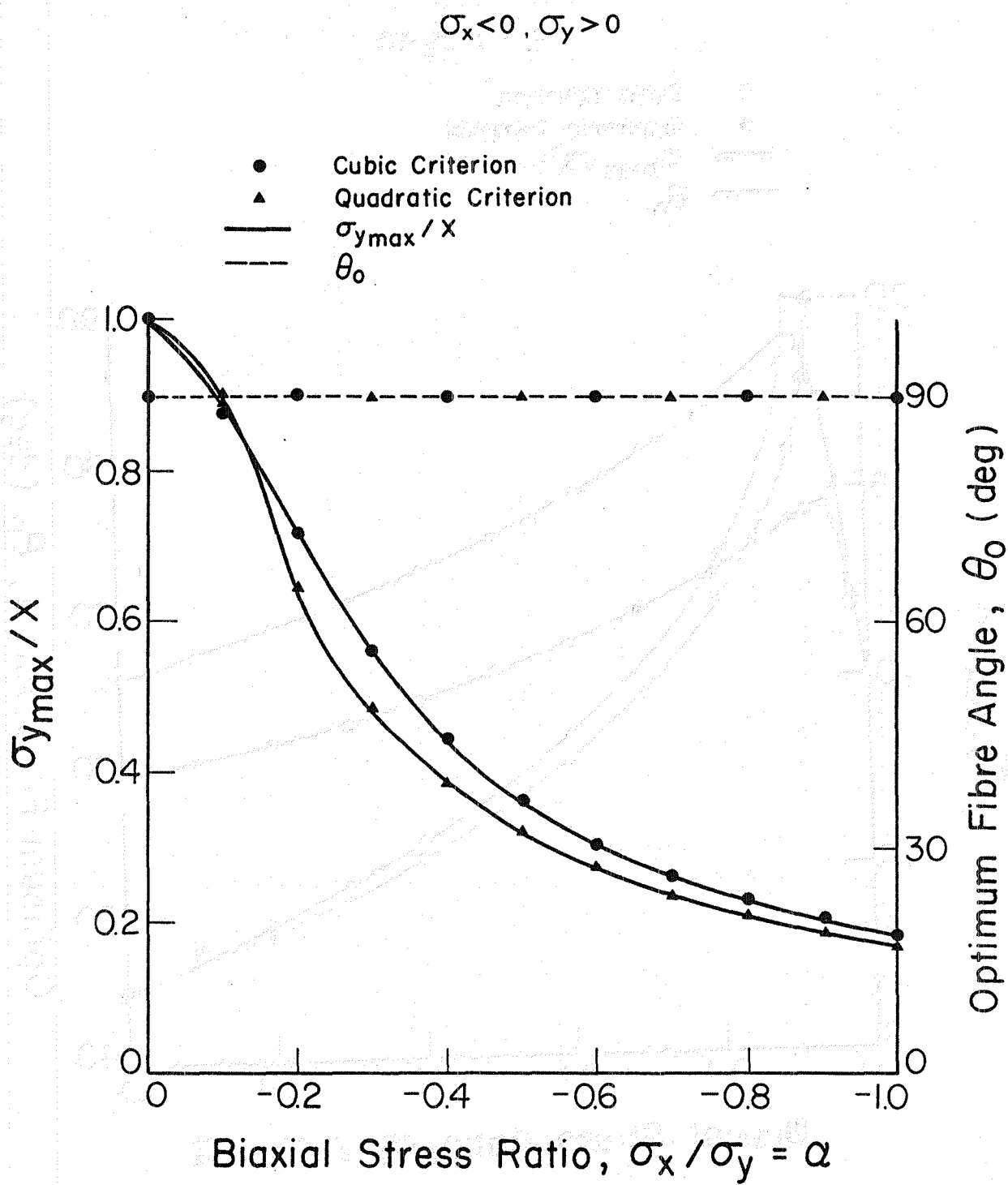


FIGURE 42: Locus of Maximum Strength and Optimum Fiber Angle for Symmetric Balanced Laminates

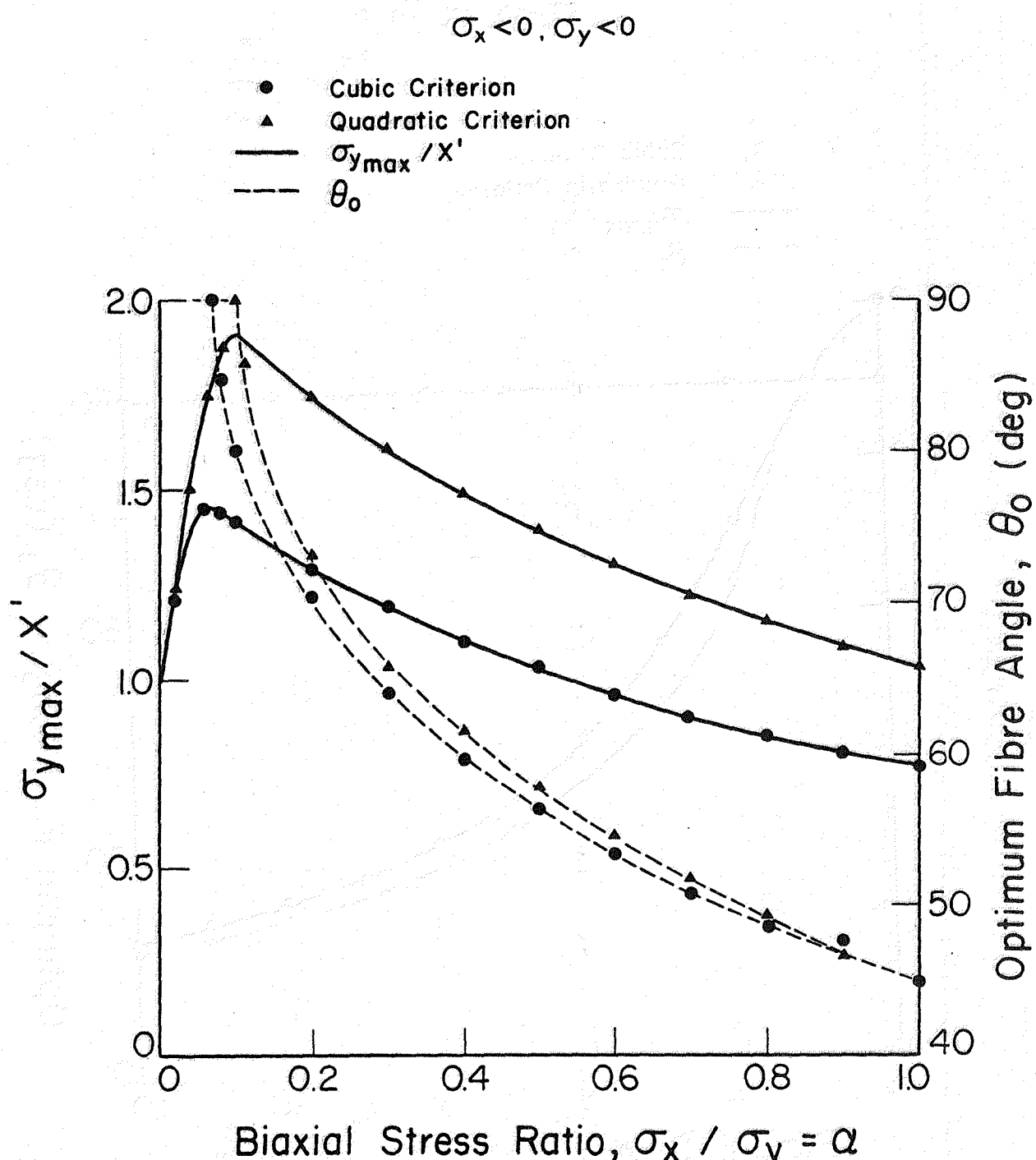
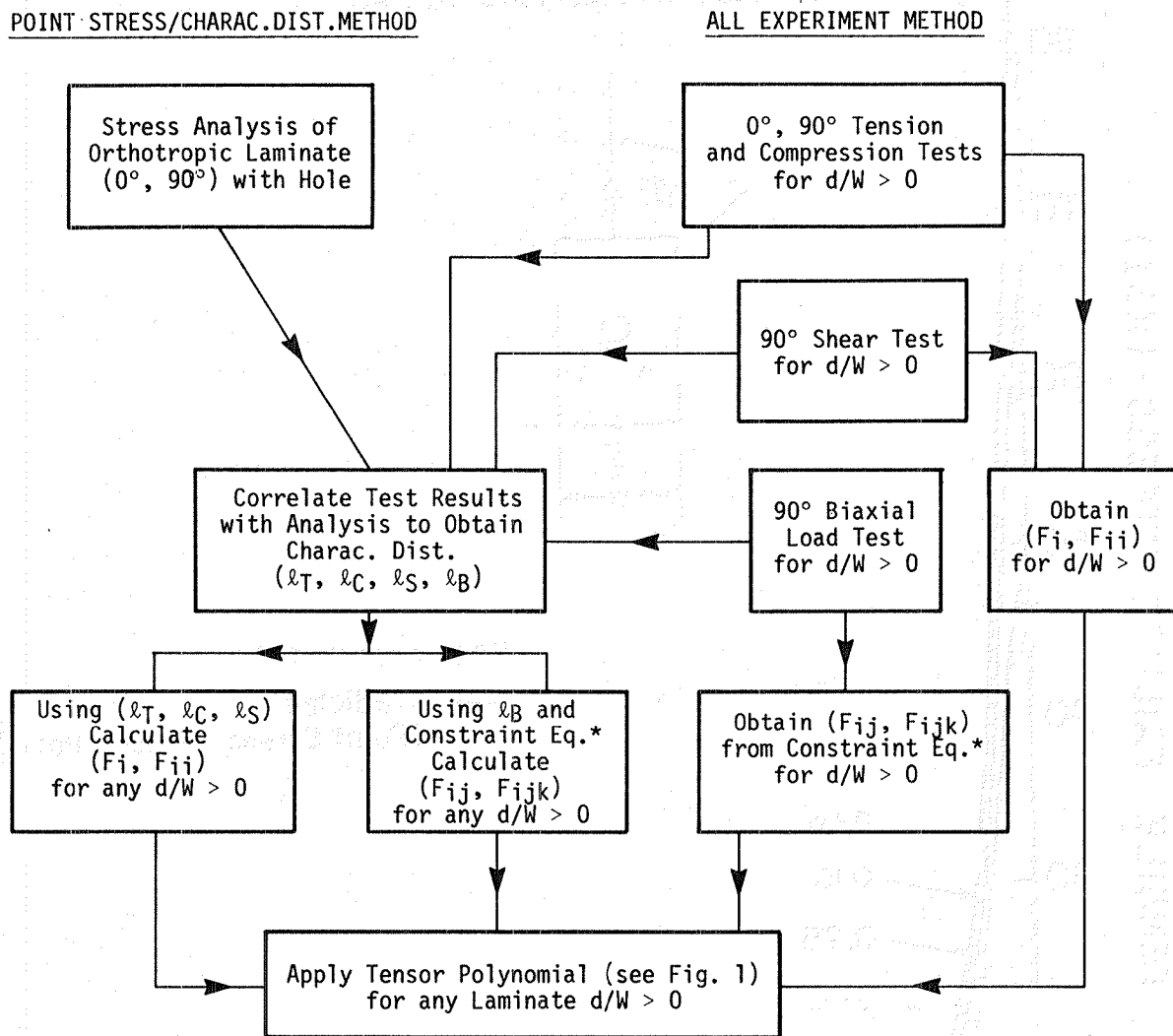


FIGURE 43: Locus of Maximum Strength and Optimum Fiber Angle for Symmetric Balanced Laminates



*see Ref. [11]

Fig. 44 Methods of Failure Analysis for Laminates with Holes

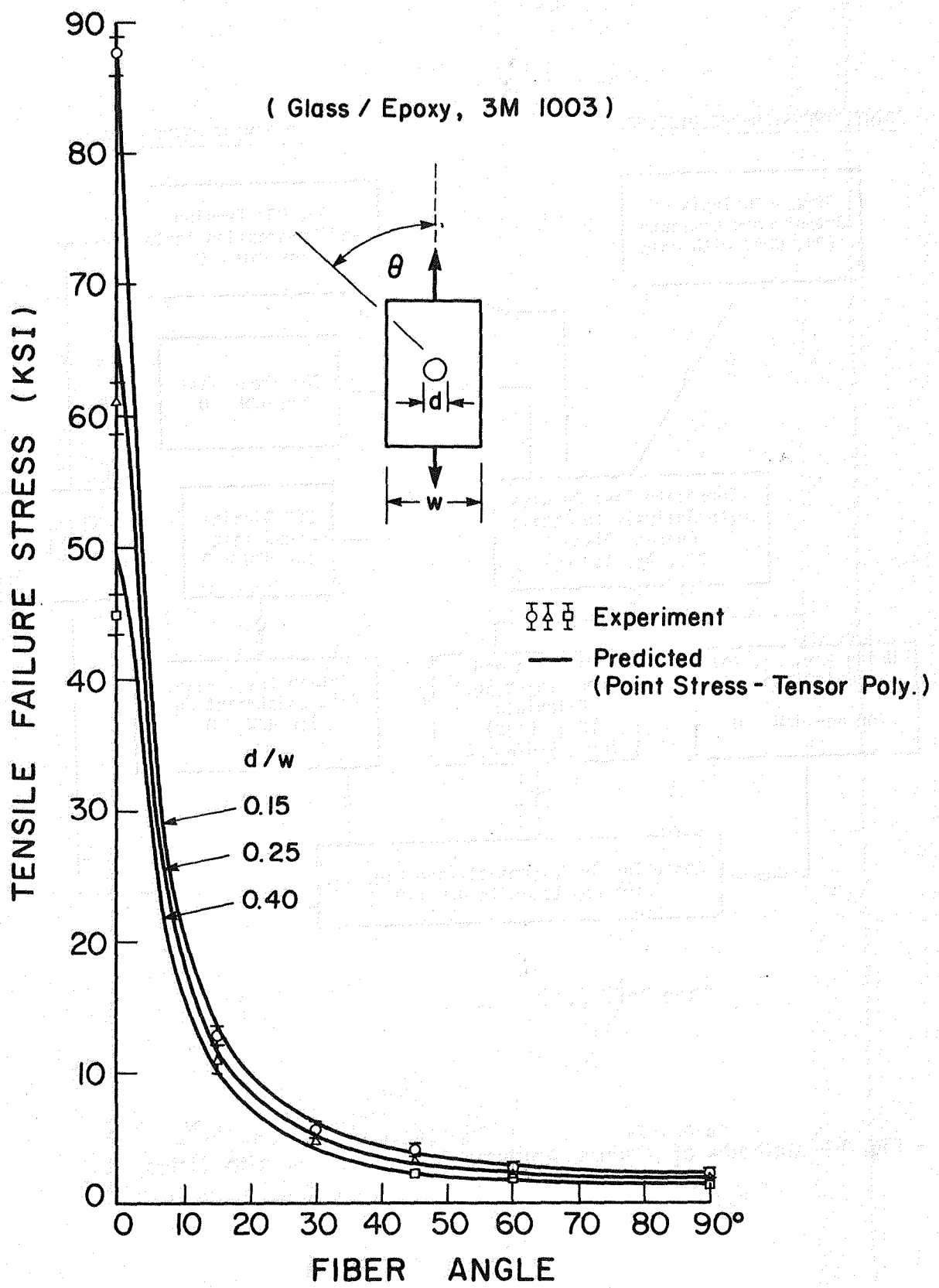


Fig.45 Failure Stress Comparisons for Off-Angle Laminates with Circular Holes

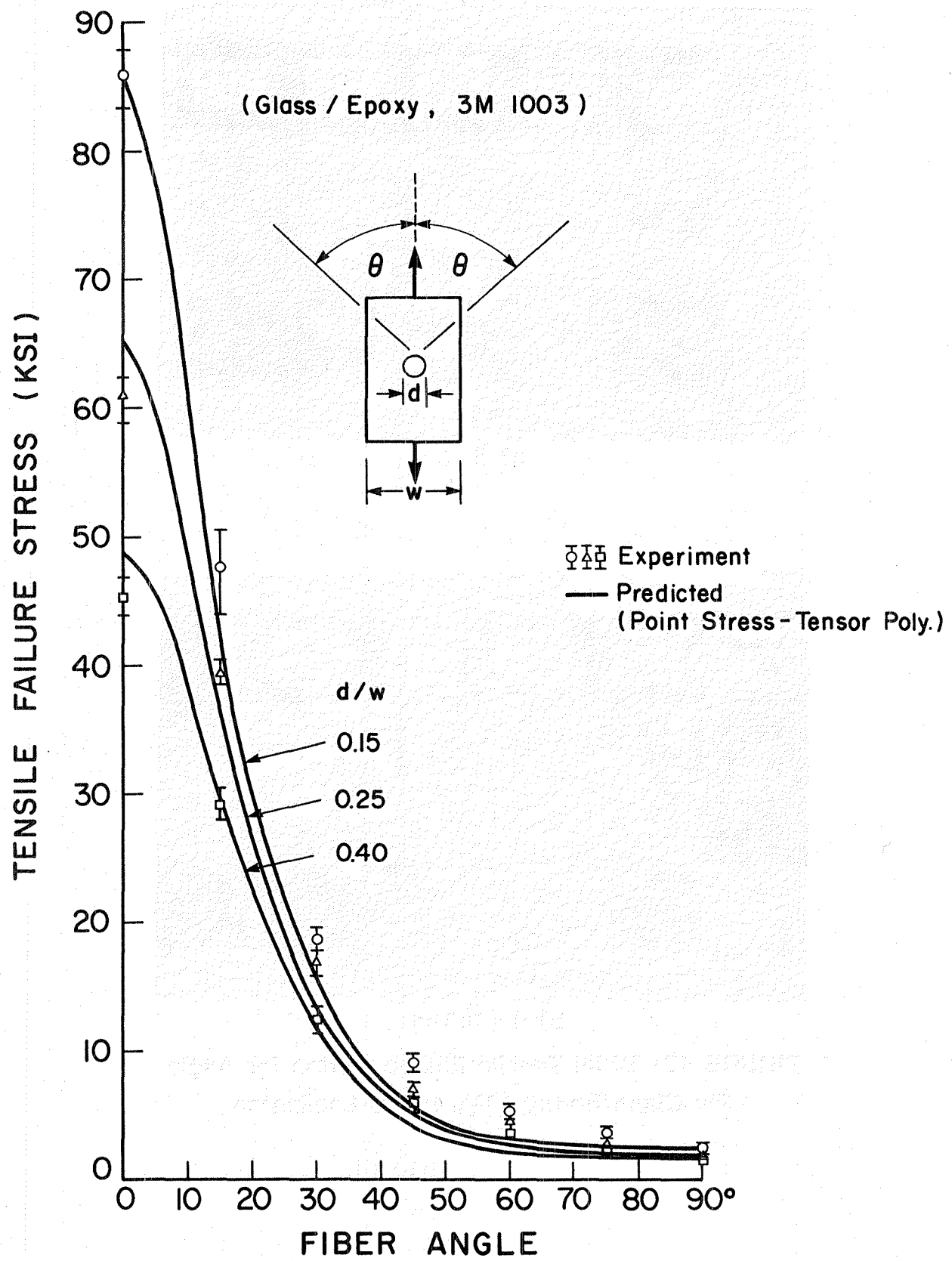
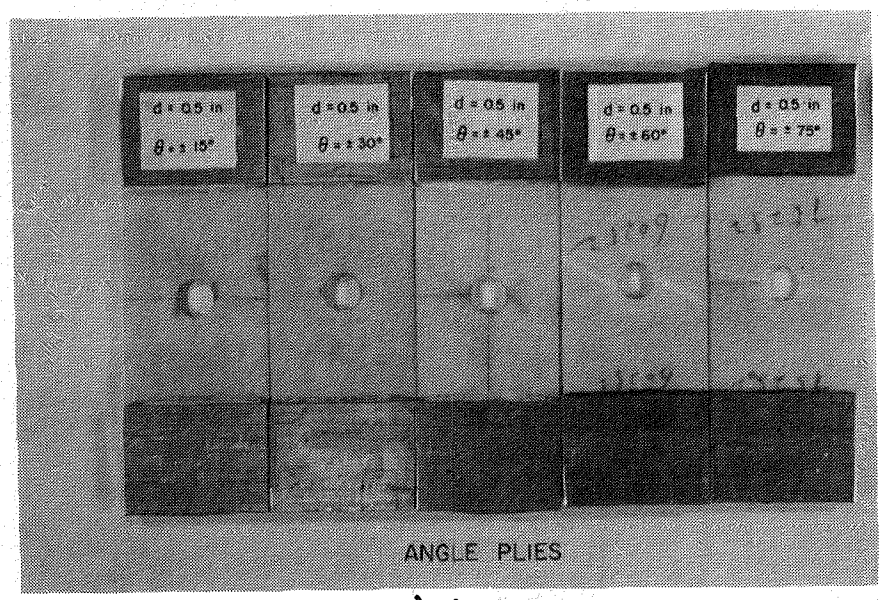
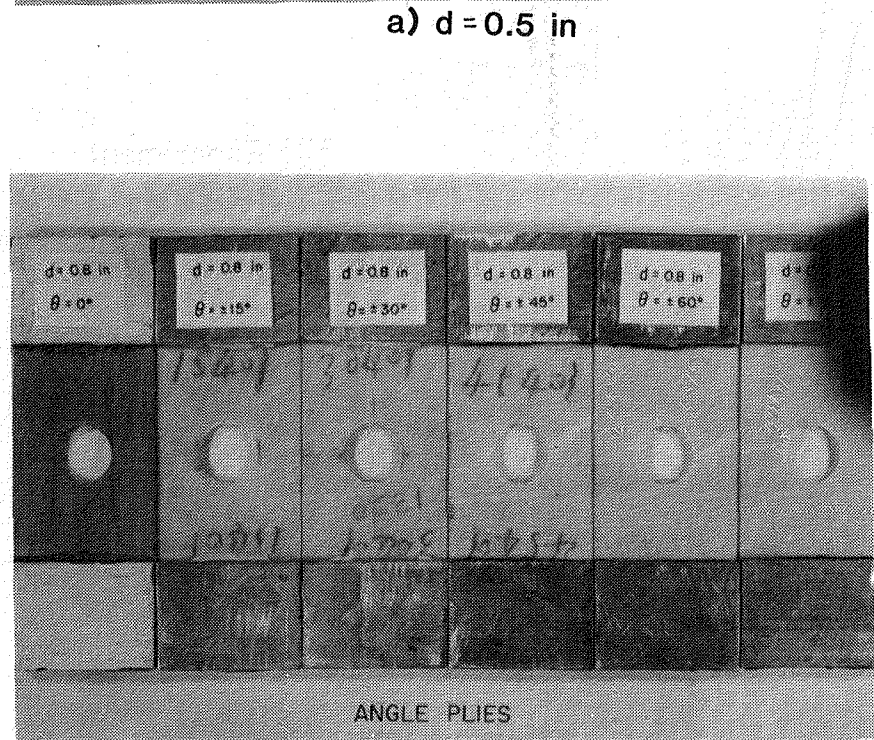


Fig.46 Failure Stress Comparisons for Angle Ply Laminates Containing Circular Holes



ANGLE PLIES

a) $d = 0.5$ in



ANGLE PLIES

b) $d = 0.8$ in

FIGURE 47: Initial Tensile Failure Modes for Angle Ply Glass/Epoxy (3M, 1003) Laminates

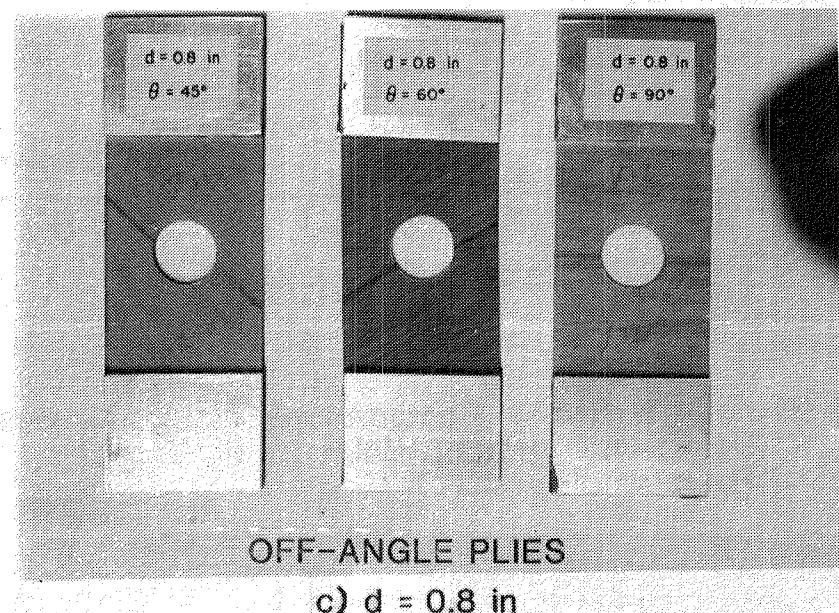
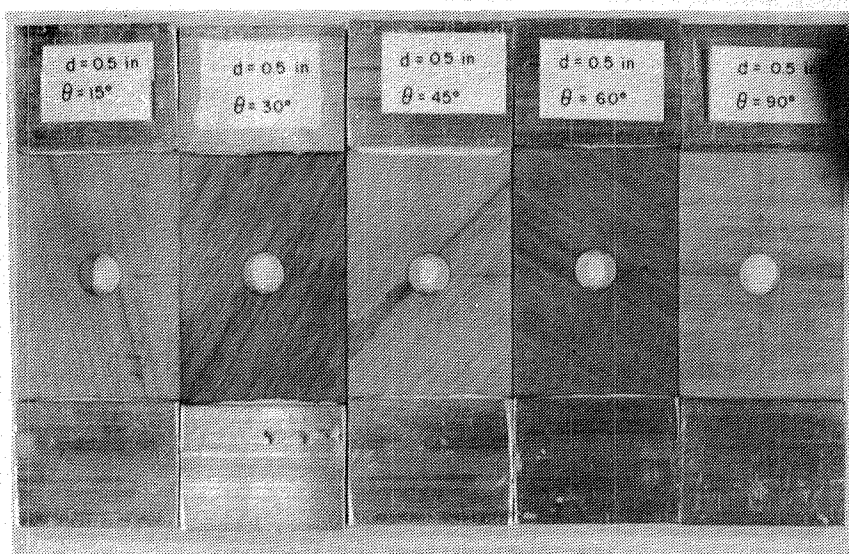
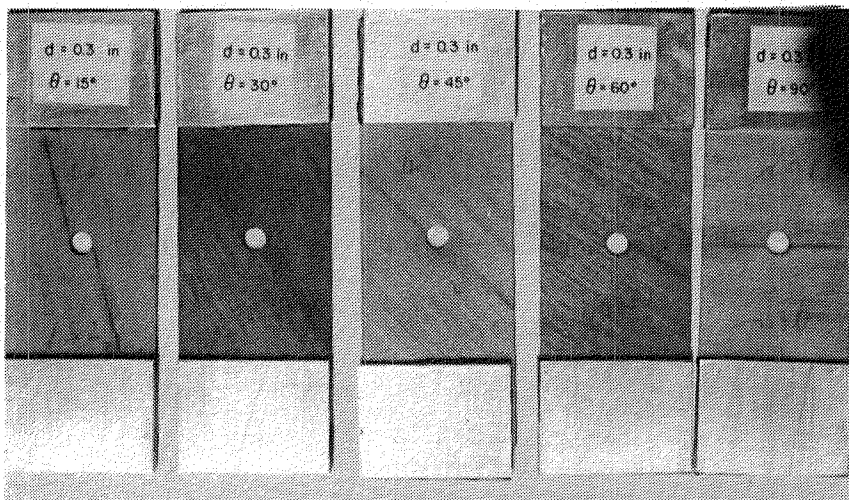


FIGURE 48: Initial Tensile Failure Modes for Off-Angle Glass/Epoxy, (3M, 1003) Laminates Containing Circular Holes

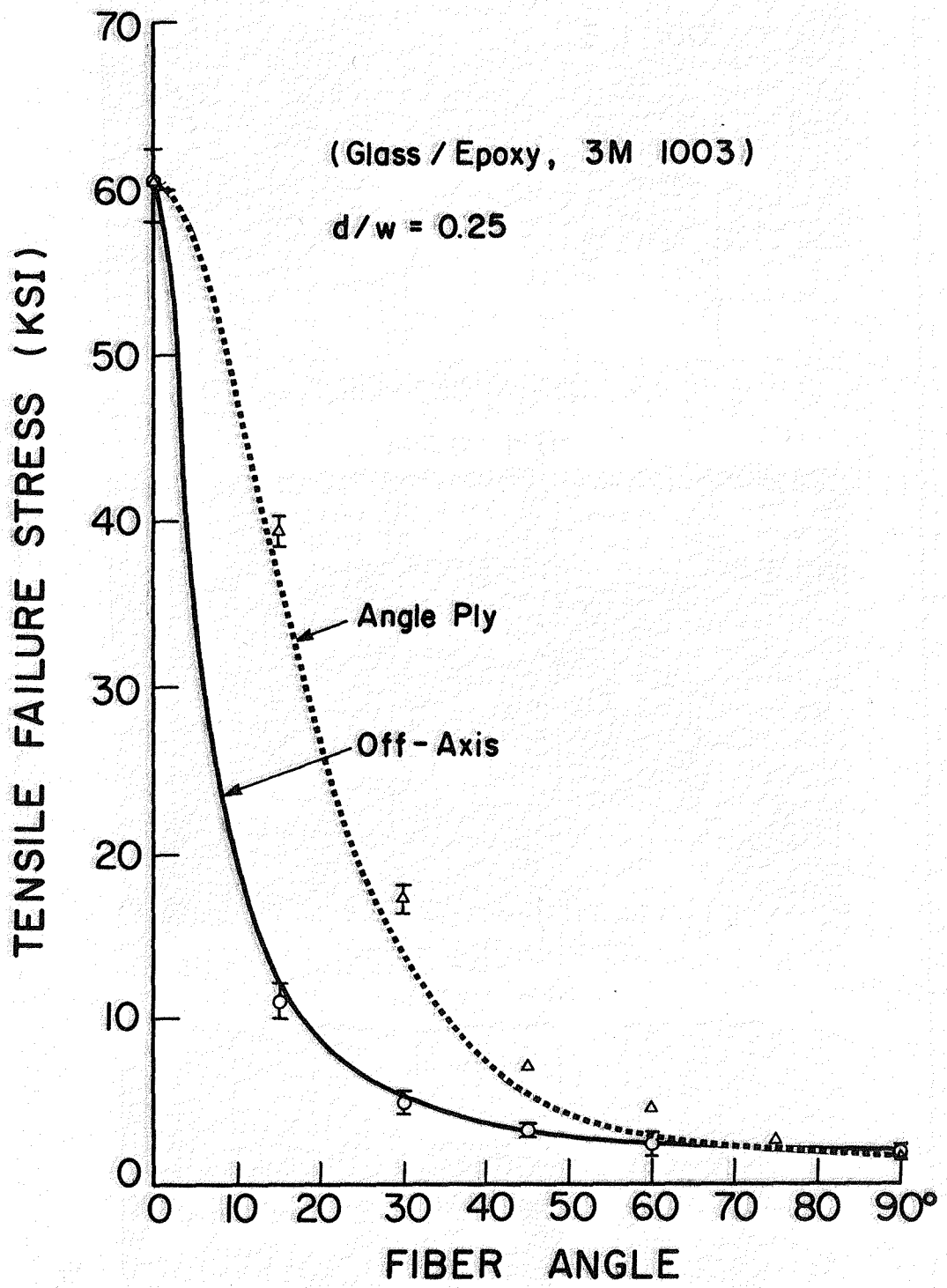


Fig. 49 Failure Stress Comparisons for Laminates Containing Circular Holes Using Tensor Polynomial.

Appendix A

Application of Strength Criterion

to Fatigue Life Prediction

The purpose of this Appendix is to illustrate how the phenomenological form of a static strength criterion can be used to predict fatigue life.

Let us assume that the fatigue life equation can be expressed in the same form as the tensor polynomial failure criterion [Eq. (1)].

However, in this case, the fatigue strength parameters are not constants, but rather are functions of the frequency of loading (n), the number of cycles (N) and the stress ratio $R = \sigma_{\min}/\sigma_{\max}$, i.e., $F = F(n, N, R)$.

The stresses in Eq. (1) shall be regarded as the maximum cyclic principal lamina stresses.

Under simple loading conditions when n and R are constants, then the fatigue strength parameters are only a function of the number of cycles, N . As stated earlier, the quadratic formulation provides good strength predictions for such load cases as uniaxial tension and compression. Consequently, for this limited set of conditions, which are typical in fatigue tests, then the fatigue strength functions necessary to characterize a lamina, are given by

$$F_1 = \frac{1}{X_D(N)} - \frac{1}{X'_D(N)} \quad F_2 = \frac{1}{Y_D(N)} - \frac{1}{Y'_D(N)} \quad F_{11} = \frac{1}{X_D(N) \cdot X'_D(N)} \quad (A.1)$$
$$F_{22} = \frac{1}{Y_D(N) \cdot Y'_D(N)} \quad F_{66} = \frac{1}{S_D(N)^2}$$

To determine the remaining quadratic interaction term would require a biaxial fatigue test. However, for non-biaxial loading, it has been found that F_{12} contributes little to the static strength prediction. In any case, fatigue tests must be conducted on 0° and 90° samples for given R values to determine the fatigue functions contained in Eqs. (A.1). This involves tension and compression fatigue tests in both the fiber (1)

and transverse (2) directions, as well as pure shear in the 1-2 plane.

A preliminary attempt using this approach, including all of the above 'fatigue functions', is contained in Ref. (21).

APPENDIX B

STRESS DIFFUSION IN AN ALUMINUM

CROSS-BEAM IN BENDING

As a first check on the ability of ADINA to adequately model the biaxial load state, the diffusion of stresses in the test section area of an aluminum cross-beam was studied. An aluminum beam, to be placed under uniaxial bending, was instrumented with strain gauges at the locations shown in Fig. B-1. The purpose of the gauges was to record the decrease in axial strain along the unloaded arm of the cross-beam. The beam was loaded uniaxially in the compression rig, and the strains were recorded at several loads. These values are listed in Table B-1.

The finite element model of the cross-beam is shown in Fig. B-2. It can be seen that, owing to symmetry, only one quarter of the beam was analysed. The element type that was selected for the ADINA analysis was the plate/shell element. To model the uniaxial bending loads, nodes 13 to 16 were constrained to behave as a simple support, and out of plane loads were applied at nodes 1 to 4. The relevant results of this analysis are summarized in Table B-2. Notice that since the program calculates the stresses in the elements at the Gaussian Integration points, the surface stresses in the beam were linearly extrapolated from these values.

Figure B-3 graphs the comparisons between ADINA and the experimental results. It plots the axial strains as a function of distance perpendicular to the loaded arm of the cross-beam. The experimental points were obtained from the values listed in Table B-1 by removing the zero offset in the load-strain response caused by some initial slack in the testing apparatus.

Figure B-3 shows the excellent correlation that was found to exist between the experimental and analytical results. It is also interesting to note that the stress field diffuses about one beam width along the unloaded arm of the cross-beam.

TABLE B-1

Experimental Data for Uniaxial Bending of Aluminum Cross-Beam

Total Load Applied (lb.)	Strains ($\mu\epsilon$)					
	ϵ_0	ϵ_1	ϵ_2	ϵ_3	ϵ_4	ϵ_5
0	0	0	0	0	0	0
2.5	-75	-63	-43	-27	-13	-130
5.0	-105	-87	-62	-35	-18	-184
7.5	-143	-120	-83	-50	-24	-250
10.0	-168	-139	-99	-56	-28	-294
12.5	-197	-165	-114	-69	-32	-344
15.0	-230	-190	-136	-78	-37	-401
17.5	-259	-217	-152	-89	-42	-452
20.0	-290	-239	-171	-98	-47	-507
22.5	-322	-266	-188	-111	-53	-561
25.0	-353	-290	-208	-120	-58	-617
27.5	-385	-320	-228	-131	-63	-671
30.0	-415	-340	-245	-141	-67	-724

TABLE B-2

ADINA Results for Uniaxial Bending of Cross-Beam

Element No.	Node No.	Stress of Integ. Pts.(psi)		Surface Strains ($\mu\epsilon$)	
		σ_x	σ_y	ϵ_x	ϵ_y
3	37	177.2	1262.	-35	210
4	37	67.84	1140.	-48	194
	41	49.86	1093.	-48	187
	45	-1.699	819.7	-42	142
	49	-37.91	529.1	-34	94
5	49	-21.95	388.4	-24	68
	53	-24.20	189.8	-14	34
	57	-11.20	67.23	-5	12

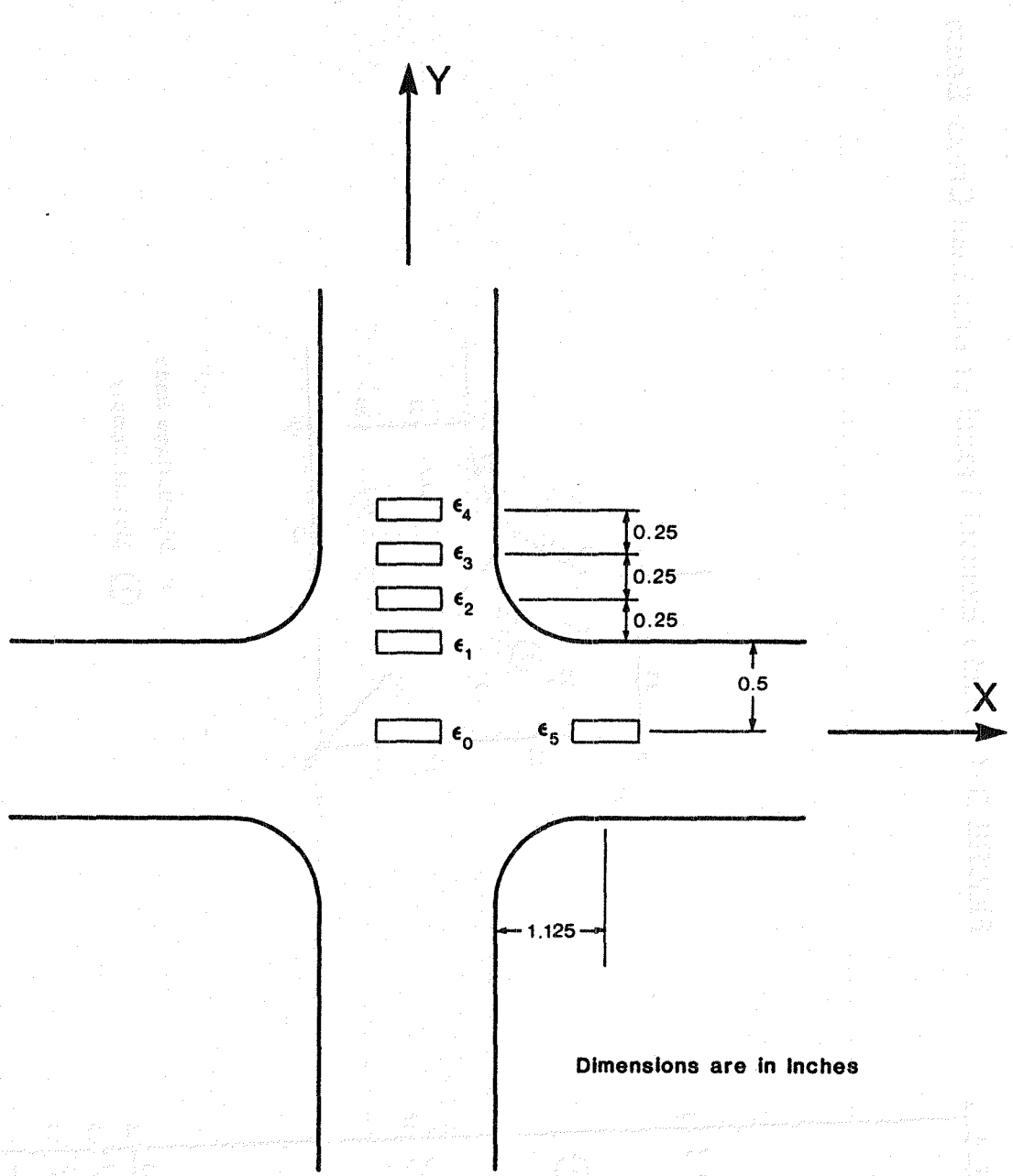


FIGURE B-1: Strain Gauge Configuration

FIGURE B-2: Finite Element Model of Aluminum Cross-Beam

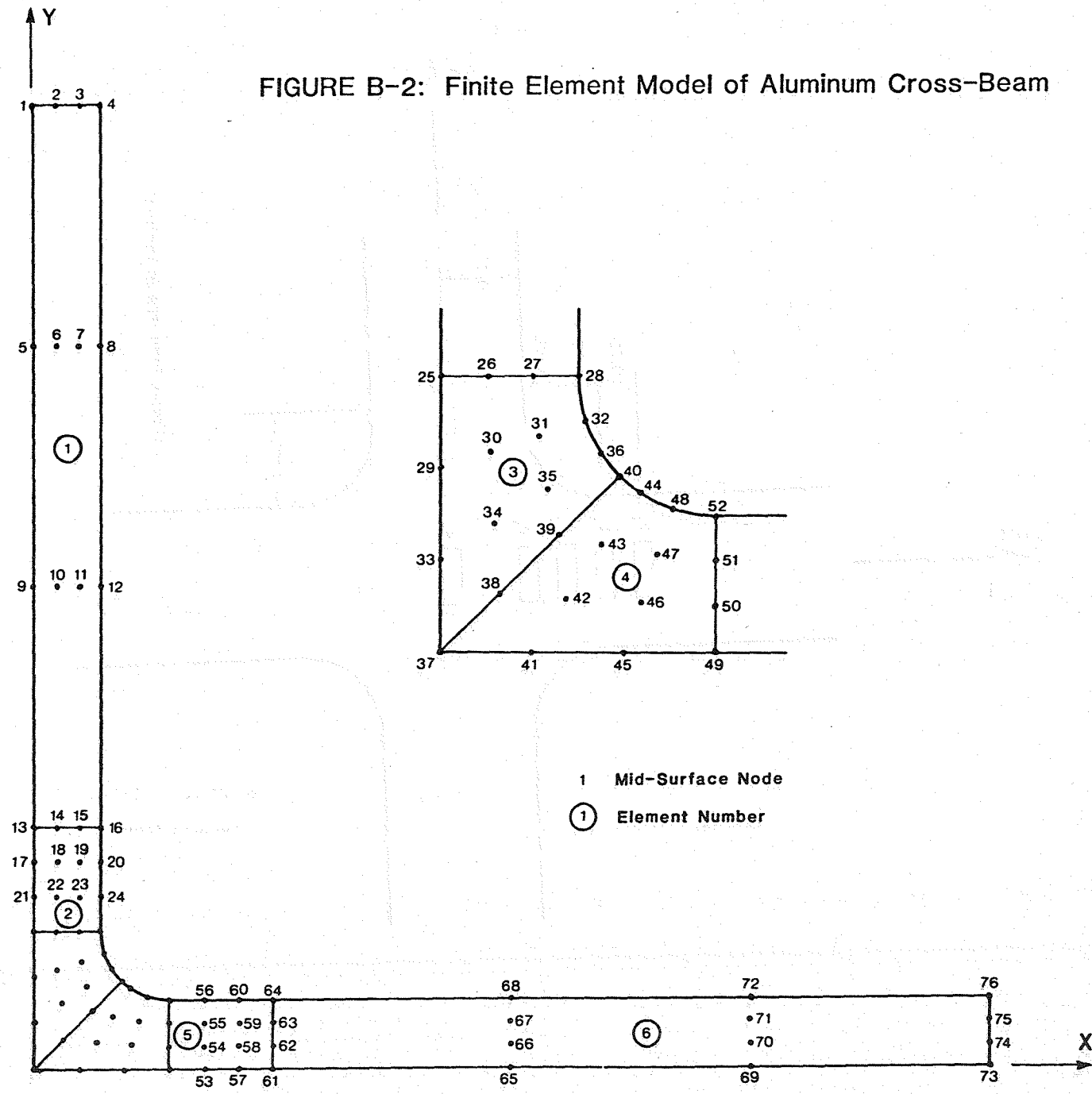
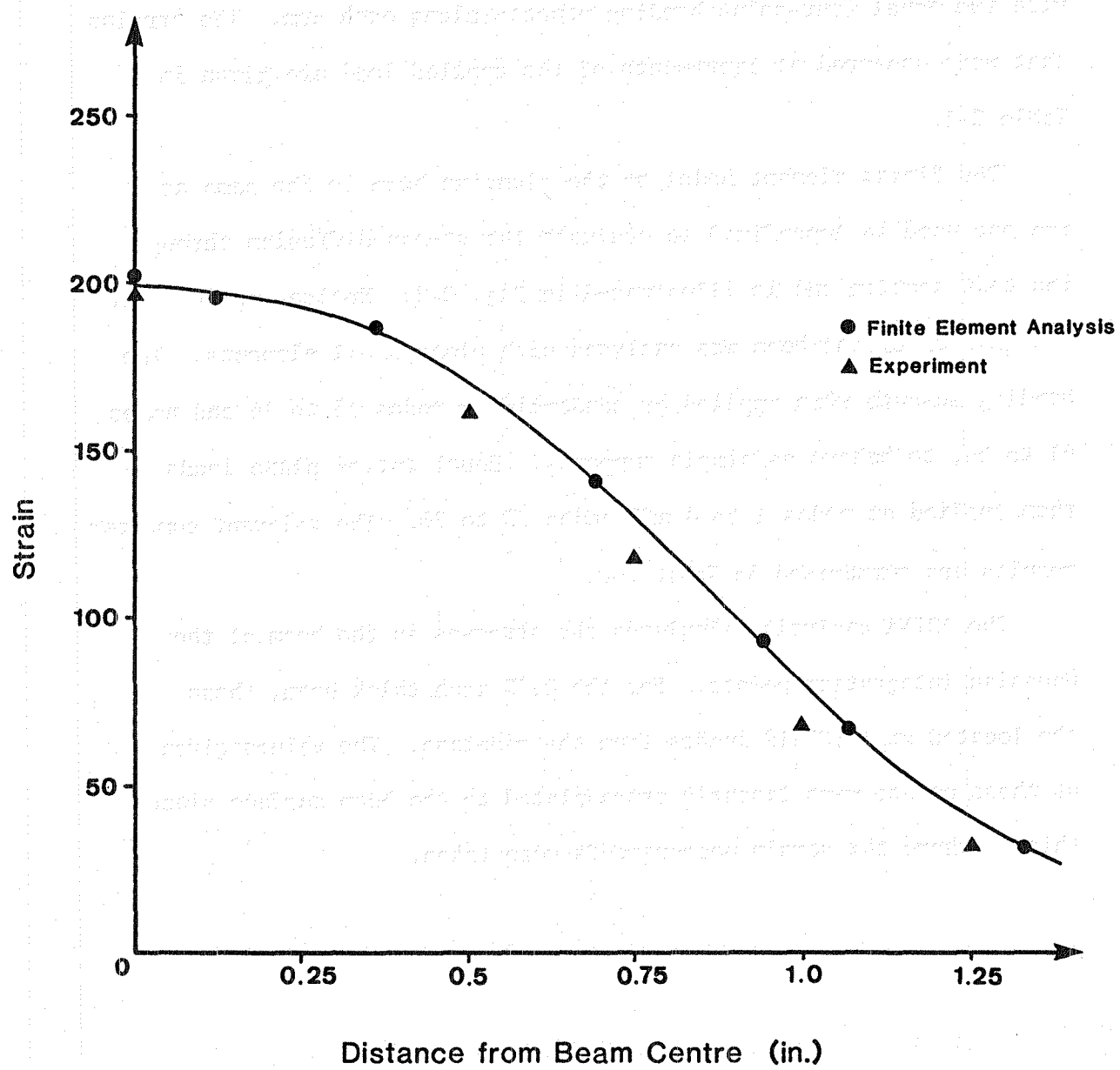


FIGURE B-3: Uniaxial Bending of Aluminum Cross-Beam



APPENDIX C

BIAXIAL BENDING OF ALUMINUM CROSS-BEAM

The second check case of ADINA involved the biaxial bending of the aluminum cross-beam. The beam was instrumented with strain gauges in the locations shown in Fig. C-1. The beam was then stressed with two equal four-point bending moments along each arm. The strains that were measured at increments of the applied load are given in Table C-1.

The finite element model of the aluminum beam is the same as the one used in Appendix B to evaluate the stress diffusion through the test section and is illustrated in Fig. C-2. Notice, again, that one quarter of the beam was analysed with plate/shell elements. The bending moments were applied by constraining nodes 13 to 16 and nodes 61 to 64, to behave as simple supports. Equal out of plane loads were then applied at nodes 1 to 4 and nodes 73 to 76. The relevant computer results are summarized in Table C-2...

The ADINA analysis calculates the stresses in the beam at the Gaussian integration points. For the 0.25 inch thick beam, these are located at ± 0.07217 inches from the midplane. The values given at these points were linearly extrapolated to the beam surface since this is where the strain measurements were taken.

Due to the symmetry of the loading and of the sample itself, the stresses will be symmetric in each of the four directions radiating from the cross-beam centre. The transverse and longitudinal strains as a function of distance from the centre are plotted in Fig. C-3. Both experimental and analytical results are shown here for comparison. It can be seen that the correlation between the results is very good, especially when one considers that the strain gauges indicate the average strain over their measuring area.

TABLE C-1

Experimental Data for Biaxial Bending of Aluminum Cross-Beam

Total Load (lb.)	Strains ($\mu\epsilon$)						ϵ_4	ϵ_5
	ϵ_{0x}	ϵ_{0y}	ϵ_1	ϵ_2	ϵ_3	ϵ_4		
0	0	0	0	0	0	0	0	0
5	-33	-40	-17	-7	14	23	-76	
10	-57	-70	-30	0	24	39	-132	
15	-75	-92	-37	-4	31	51	-174	
20	-94	-114	-49	0	39	65	-219	
25	-116	-140	-59	-2	49	80	-271	
30	-137	-164	-70	-2	57	93	-320	
35	-159	-188	-85	-3	66	107	-369	
40	-181	-211	-92	-2	74	121	-420	
45	-204	-235	-104	-5	82	134	-472	
50	-227	-259	-118	-3	91	149	-524	

TABLE C-2

ADINA Results for Biaxial Bending of Cross-Beam

Element No.	Node No.	Stress of Integ. Pts.(psi)		Surface Strains ($\mu\epsilon$)	
		σ_x	σ_y	ϵ_x	ϵ_y
3	37	1317.	1330.	159.	162.
4	37	1330.	1317.	162.	159.
	41	1514.	1196.	200.	128.
	45	1782.	796.6	267.	45.
	49	2067.	502.3	332.	-20.
5	49	2161.	399.0	354.	-43.
	53	2145.	298.0	356.	-60.
	57	2254.	422.1	368.	-44.
	61	2421.	663.0	385.	-11.

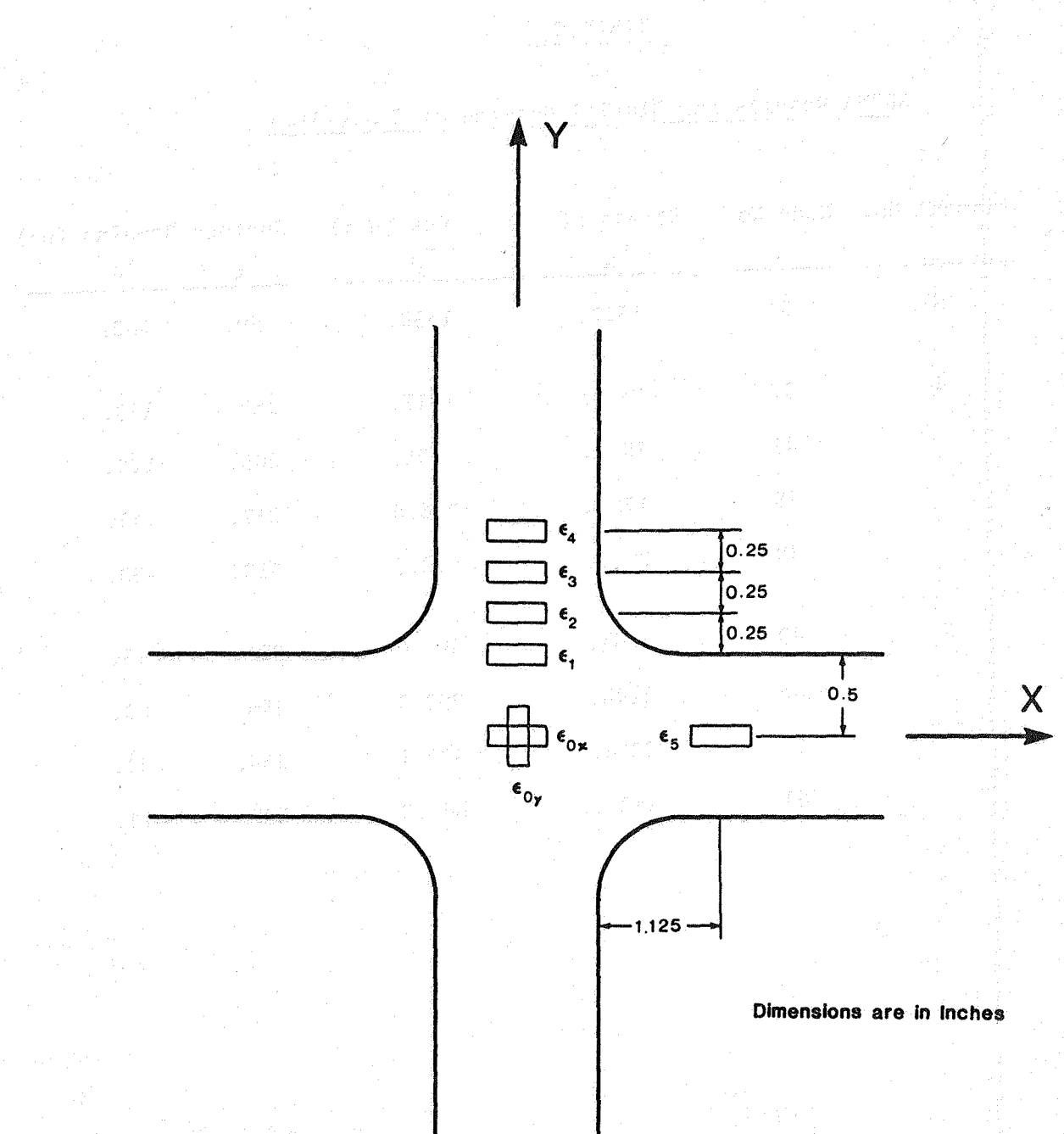


FIGURE C-1: Strain Gauge Configuration

FIGURE C-2: Finite Element Model of Aluminum Cross-Beam

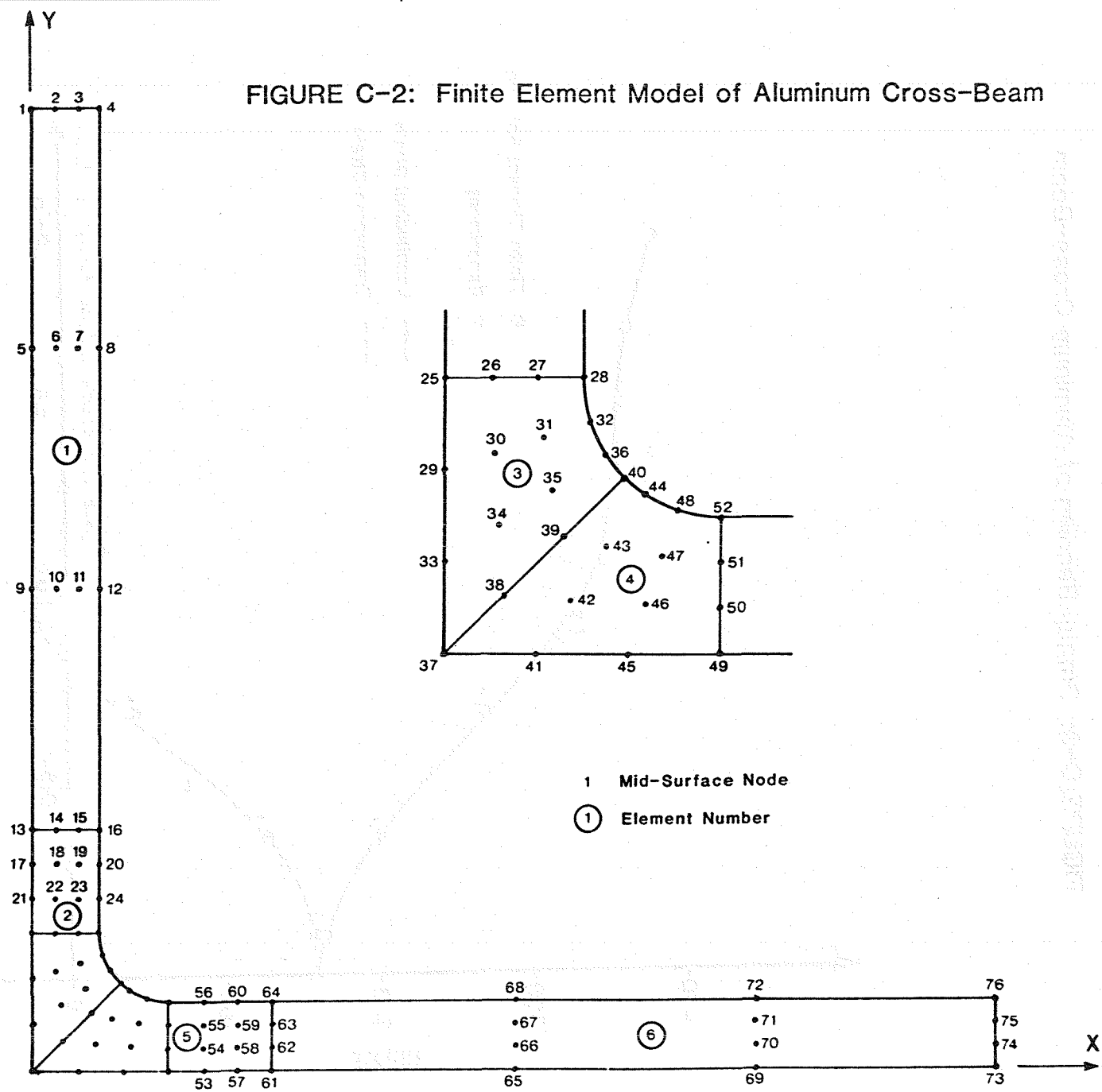
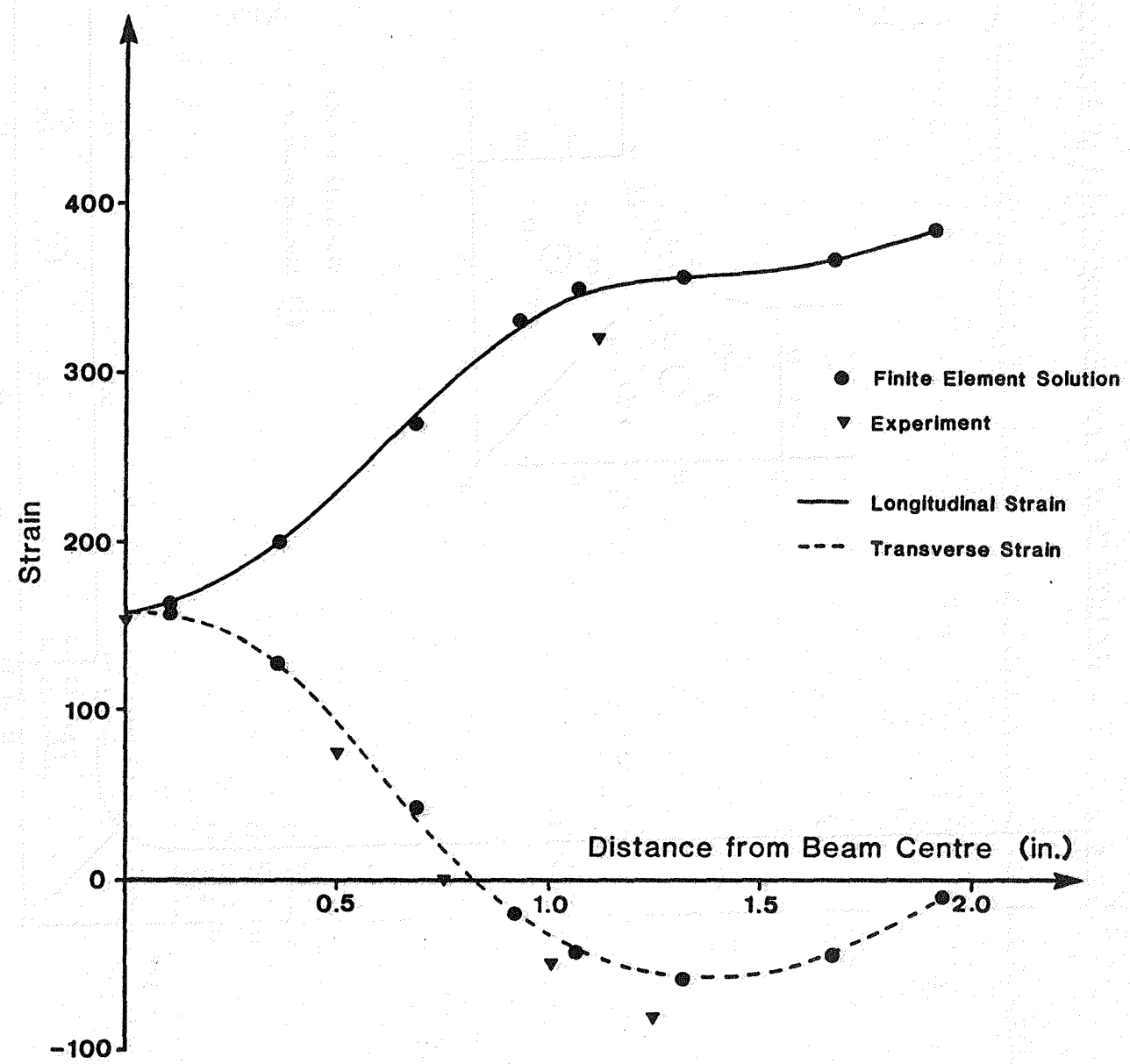


FIGURE C-3: Biaxial Bending of Aluminum Cross-Beam



APPENDIX D

FINITE ELEMENT ANALYSIS OF THE HONEYCOMB

SANDWICH CROSS-BEAM

The finite element model of the honeycomb sandwich cross-beam using ADINA is illustrated in Fig. D-1. The honeycomb was modelled with 3-D elements and the facings with 2-D plate elements. The plate elements have the same node numbering as the upper and lower surfaces of the 3-D elements. They also have the necessary orthotropic material capability for the composite facing. All of the elements are isoparametric and could thus be distorted to follow the contours of the beam. Due to symmetry considerations, only one quarter of the sample was analysed.

Some difficulties were encountered in the correlation between the experimental beam stiffness and the analytical results produced by ADINA. A parameter study was performed to examine the effect of varying the composite modulus and honeycomb thickness on the overall beam stiffness as predicted by the computer program. The results of this study are shown in Table D-1. This table lists the load-strain response of the beam in uniaxial bending as was calculated by ADINA. To bring the analytical results to within ten percent of the experimental values, the honeycomb thickness and composite modulus were required to be modified to the values indicated on the table. As a check on the results, the new parameters were used in a biaxial case shown in Table D-2. It can be seen that with the modified parameters, the difference between experiment and analysis is less

than 10% here also. This is the configuration that was used in all analyses of the cross-beam.

Having established a model of the cross-beam which corresponds to experimental results, a study of the response to various biaxial load ratios was undertaken. The results of this study are shown in Fig. D-2. This figure plots the strain ratio in the test section as a function of the load ratio applied to the beam. Since the desired stress ratio for the biaxial compression experiment was about $\sigma_1/\sigma_2 \approx 13$, the corresponding strain ratio was about $\epsilon_1/\epsilon_2 \approx 1$. Thus the appropriate biaxial load ratio was found to be $P/F \approx 0.25$.

TABLE D-1
Parameter Study of Cross-Beam in Uniaxial Bending

ADINA

Honeycomb Thickness (in)	Composite Stiffness		Load-Strain Response ($\mu\epsilon/1b.$)			
	E_{11}	E_{22}	X-Loading		Y-Loading	
			ϵ_x/F	ϵ_y/F	ϵ_x/F	ϵ_y/F
1.625	20.5	1.4	-5.74	4.25	4.10	-28.0
2.0	20.5	1.4	-4.48	3.88	3.51	-22.0
2.0	19.0	1.4	-4.77	4.11	3.72	-22.2
2.0	19.0	1.8	-4.74	3.80	3.43	-19.7
*2.0	18.5	1.8	-4.84	3.87	3.51	-19.7

EXPERIMENT

-	-	-	-5.37	3.69	3.49	-18.5
---	---	---	-------	------	------	-------

*Final Modifications

TABLE D-2

Parameter Study of Cross-Beam in Biaxial Bending

ADINA

Honeycomb Thickness (in.)	Composite Stiffness E_{11} ($\times 10^6$ psi)	Composite Stiffness E_{22}	Load-Strain Response ($\mu\epsilon/1b.$) ϵ_x/F	Load-Strain Response ($\mu\epsilon/1b.$) ϵ_y/F
---------------------------------	---	---------------------------------	--	--

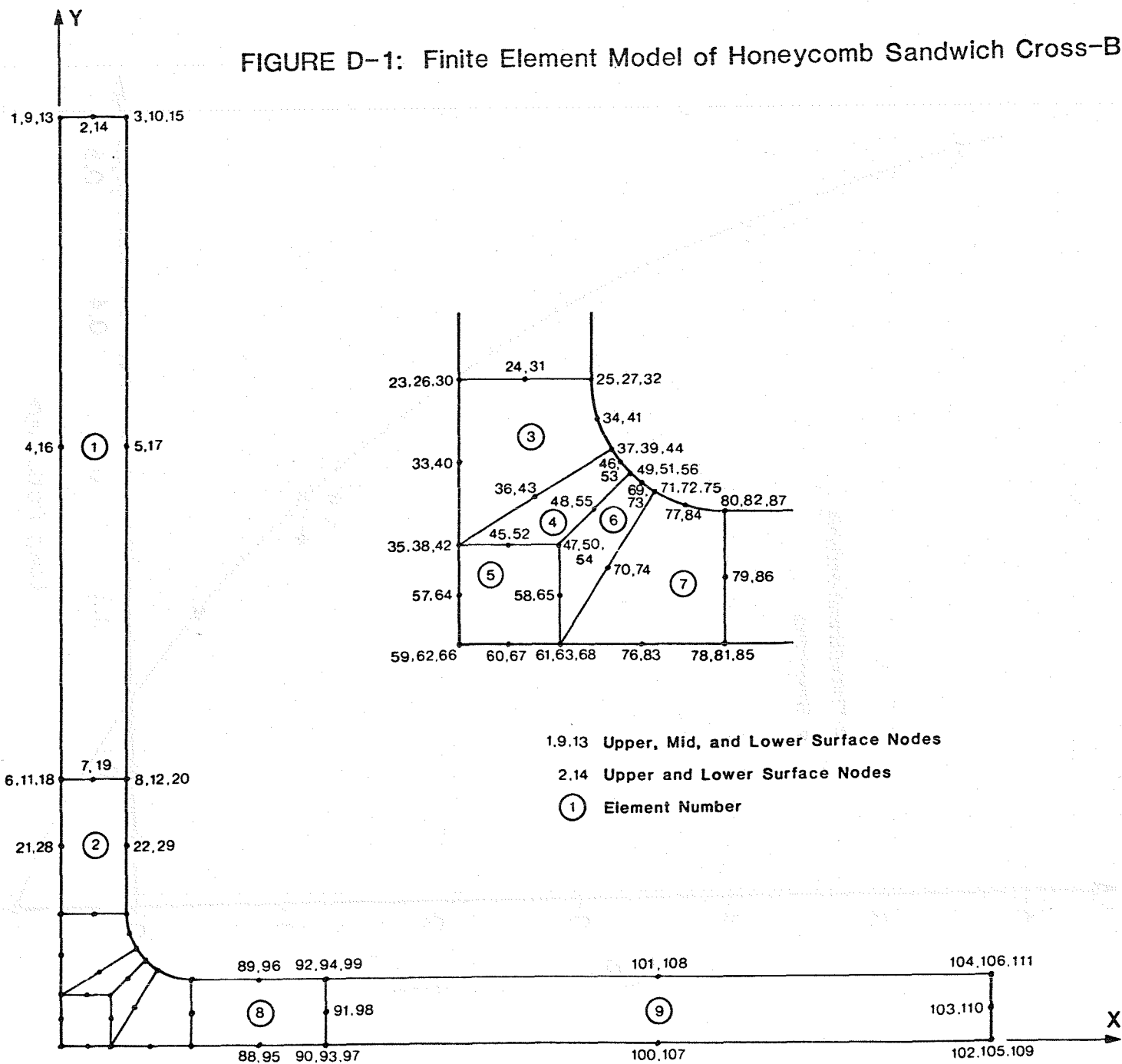
1.625	20.5	1.4	-5.80	4.3
*2.0	18.5	1.8	-4.56	3.34

EXPERIMENT

	-	-	-5.00	3.13
--	---	---	-------	------

***Modified Values**

FIGURE D-1: Finite Element Model of Honeycomb Sandwich Cross-Beam



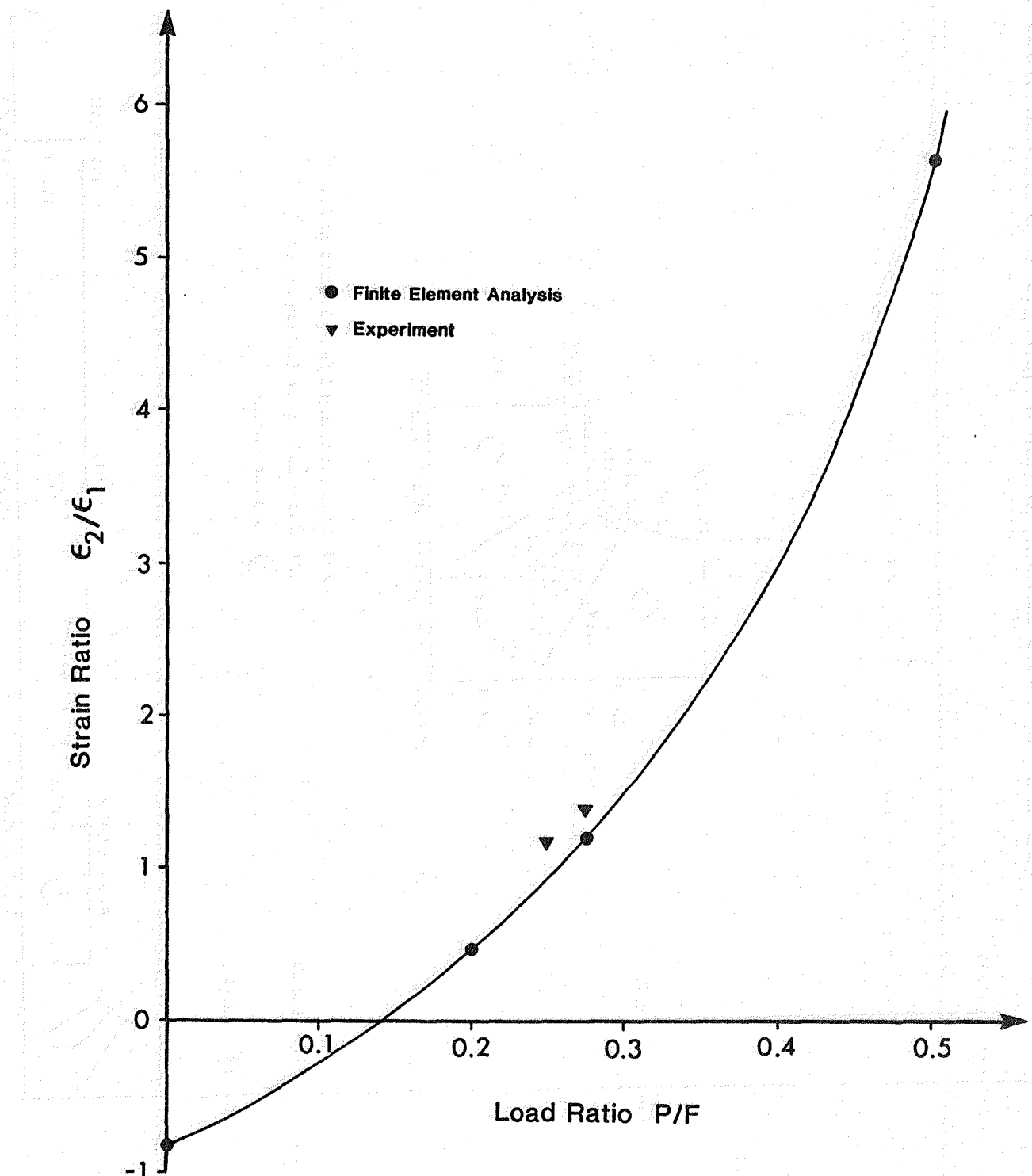


FIGURE D-2: Biaxial Compression of Honeycomb Sandwich Cross-Beam

APPENDIX E

CROSS-BEAM ANALYSIS USING BEAM THEORY

The design of the cross-beam required the knowledge of the stresses and loads that would be applied to the sample at failure. This was necessary to ensure that premature failure of the honeycomb, for example, did not occur before material failure of the composite. The cost of the finite element analysis was prohibitive for this initial design process, so beam theory was used.

The assumption that was made was that the analysis of the cross-beam could be separated into the analysis of two separate single beams in bending, with some constraint and compatibility requirements. It was also assumed that the interaction area between the two beams could be represented by a constant continuous load. The forces acting on the two beams are illustrated in Fig. E-1.

Each of the beams can be separated into three distinct sections, as shown. Analysing the first beam only, and observing the force balance in Fig. E-2a, the curvature, slope and displacement are

$$\left. \frac{d^2 w}{dx^2} \right|_1 = - \frac{F_1 x}{\Sigma(EI)_1} \quad (E.1a)$$

$$\left. \frac{dw}{dx} \right|_1 = \frac{1}{\Sigma(EI)_1} \left(k_1 - \frac{F_1 x^2}{2} \right) \quad (E.1b)$$

$$w|_1 = \frac{1}{\Sigma(EI)_1} \left(k_2 + k_1 x - \frac{F_1 x^3}{6} \right) \quad (E.1c)$$

where k_1 and k_2 are integration constants. Similarly, for section 2, from Fig. E-2b

$$\frac{d^2w}{dx^2} \Big|_2 = \frac{1}{(\Sigma EI)_1} [(F_2 - F_1)x - F_2 \ell_1] \quad (E.2a)$$

$$\frac{dw}{dx} \Big|_2 = \frac{1}{(\Sigma EI)_1} \left[k_3 - F_2 \ell_1 x + (F_2 - F_1) \frac{x^2}{2} \right] \quad (E.2b)$$

$$w \Big|_2 = \frac{1}{(\Sigma EI)_1} \left[k_4 + k_3 x - \frac{F_2 \ell_1 x^2}{2} + (F_2 - F_1) \frac{x^3}{6} \right] \quad (E.2c)$$

And finally for section 3, from Fig. E-2c

$$\frac{d^2w}{dx^2} \Big|_3 = \frac{1}{(\Sigma EI)_1} \left\{ -F_2 \ell_1 + (F_2 - F_1)x + p \left[\frac{x^2}{2} - d_1 x + \frac{d_1^2}{2} \right] \right\} \quad (E.3a)$$

$$\frac{dw}{dx} \Big|_3 = \frac{1}{(\Sigma EI)_1} \left\{ k_5 - F_2 \ell_1 x + (F_2 - F_1) \frac{x^2}{2} + p \left[\frac{x^3}{6} - d_1 \frac{x^2}{2} + \frac{d_1^2 x}{2} \right] \right\} \quad (E.3b)$$

$$w \Big|_3 = \frac{1}{(\Sigma EI)_1} \left\{ k_6 + k_5 x - F_2 \ell_1 \frac{x^2}{2} + (F_2 - F_1) \frac{x^3}{6} + p \left[\frac{d_1^4}{24} - \frac{d_1 x^3}{6} + \frac{d_1^2 x^2}{4} \right] \right\} \quad (E.3c)$$

where k_3 , k_4 , k_5 and k_6 are integration constants. The zero slope condition at the beam centre gives

$$k_5 = F_2 \ell_1 L_1 - (F_2 - F_1) \frac{L_1^2}{2} - p \left[\frac{L_1^3}{6} - \frac{d_1 L_1^2}{2} + \frac{d_1^2 L_1}{2} \right] \quad (E.4)$$

Slope compatibility between sections 1 and 2, and between sections 2 and 3 gives

$$k_1 = k_3 - \frac{F_2 \ell_1^2}{2} \quad (E.5)$$

$$k_3 = k_5 + \frac{pd_1^3}{6} \quad (E.6)$$

Displacement compatibility between the sections 2 and 3 gives

$$k_6 = k_4 + k_3 d_1 - k_5 d_1 - p \frac{d_1^4}{8} \quad (E.7)$$

Zero displacement at load point F_2 ($x=\ell_1$) gives

$$k_2 = \frac{F_1 \ell_1^3}{6} - k_1 \ell_1 \quad (E.8)$$

and

$$k_4 = (2F_2 + F_1) \frac{\ell_1^3}{6} - k_3 \ell_1 \quad (E.9)$$

Equations (E.4) to (E.9) can be solved for the six interation constants, k_i . A similar set of equations can be obtained for the second beam. It only remains to find the relationships between the forces, F_i and p .

Equating displacements between the ends ($x=0$) of the two beams gives

$$F_1 \left[\frac{\ell_1(\ell_1^2 - 3L_1^2)}{6(\Sigma EI)_1} \right] + F_2 \left[\frac{\ell_1 \ell_3^2}{8(\Sigma EI)_1} \right] + F_3 \left[\frac{-\ell_2(\ell_2^2 - 3L_2^2)}{6(\Sigma EI)_2} \right] \\ + F_4 \left[\frac{-\ell_2 \ell_3^2}{8(\Sigma EI)_2} \right] + p \left[\frac{w^3}{48} \right] \left[\frac{\ell_1}{(\Sigma EI)_1} + \frac{\ell_2}{(\Sigma EI)_2} \right] = 0 \quad (E.10)$$

Equating displacements between the beams at the beam centres gives

$$F_1 \left[\frac{\ell_1^3 - 3\ell_1 L_1^2 + 2L_1^3}{6(\Sigma EI)_1} \right] + F_2 \left[\frac{-\ell_3^3}{24(\Sigma EI)_1} \right] + F_3 \left[\frac{-\ell_2^3 + 3\ell_2 L_2^2 - 2L_2^3}{6(\Sigma EI)_2} \right] \\ + F_4 \left[\frac{\ell_3^3}{24(\Sigma EI)_2} \right] + p \left[\frac{\ell_1 w^3 + 2d_1^4 - 12d_1^2 L_1^2 + 16d_1 L_1^3 - 6L_1^4}{48(\Sigma EI)_1} \right. \\ \left. + \frac{\ell_2 w^3 + 2d_2^4 - 12d_2^2 L_2^2 + 16d_2 L_2^3 - 6L_2^4}{48(\Sigma EI)_2} \right] = 0 \quad (E.11)$$

Assume that the loads acting upon the beam in Fig. E-1 can be separated into the sum of a pressure load and its simple support response, and a four-point bending load, as shown in Fig. E-3. Summing the forces at the load points gives

$$F_1 - F'_1 + C_1 p = 0 \quad (E.12a)$$

$$F_2 - F'_2 + C_2 p = 0 \quad (E.12b)$$

The values of C_1 and C_2 , due to the pressure load, are obtained from Castigliano's first theorem by minimizing the strain energy on that beam. Thus

$$C_2 = \frac{2w\ell_1^3 - 6w\ell_1 d_1^2 - \ell_1 w^3 - 6w^2 \ell_1 d_1}{16\ell_1^3 - 24\ell_1^2 d_1 - 12\ell_1^2 w} \quad (E.13a)$$

$$C_1 = C_2 - \frac{w}{2} \quad (E.13b)$$

Similarly for the second beam

$$F_3 - F'_3 - C_3 p = 0 \quad (E.14a)$$

$$F_4 - F'_3 - C_4 p = 0 \quad (E.14b)$$

where

$$C_4 = \frac{2w\ell_2^3 - 6w\ell_2 d_2^2 - \ell_2 w^3 - 6w^2 \ell_2 d_2}{16\ell_2^3 - 24\ell_2^2 d_2 - 12\ell_2^2 w} \quad (E.15a)$$

$$C_3 = C_4 - \frac{w}{2} \quad (E.15b)$$

And finally, the total load, F , on the cross-beam is given by

$$F = F_1 + F_2 + F_3 + F_4 \quad (E.16)$$

Given the total load, Eqs. (E.10) to (E.16) can be solved for the seven unknown forces, F_1 , F_2 , F_3 , F_4 , F'_1 , F'_3 and p . Having obtained these values, they can be back substituted to solve for the beam displacements and slopes.

The stresses in the beam can now be determined. Consider only the first beam, and define it to be oriented in the x-direction. The bending moment at the centre of the beam is given by

$$M_x = -F_2 \ell_1 + (F_2 - F_1)L_1 + \frac{p}{2} (L_1 - d_1)^2 \quad (E.17)$$

The stresses at thickness z from the composite surface are given by

$$\sigma_{xc} = \frac{E_{cx} M_x (y_{c01} - z)}{(\Sigma EI)_1} \quad (E.18)$$

where E_{cx} = Young's modulus of the composite in the x-direction
 y_{c01} = Distance of the composite outer surface to the neutral axis of the first beam.

The maximum stresses in the metal are given by

$$\sigma_{xm} = \frac{-E_m M_x}{(\Sigma EI)_1} [t_c + t_h + t_m + 2t_a - y_{c01}] \quad (E.19)$$

where t_c , t_h , t_m and t_a are the thickness of the composite, honeycomb, metal and adhesive, respectively. The shear stress between the honeycomb and composite is given by

$$\tau_{cx} = \frac{F_1}{2(\Sigma EI)_1} \left\{ E_{cx} [y_{c01}^2 - (y_{c01} - t_c)^2] + E_a [(y_{c01} - t_c)^2 - (y_{c01} - t_c - t_a)^2] \right\} \quad (E.20)$$

And the shear stress between the honeycomb and the metal is given by

$$\tau_{mx} = \frac{F_1}{2(\Sigma EI)_1} \left\{ E_m [(t_h + t_m + t_c + 2t_a - y_{c01})^2 - (t_h + t_c + 2t_a - y_{c01})^2] + E_a [(t_h + t_c + 2t_a - y_{c01})^2 - (t_h + t_c + 2t_a - y_{c01})^2] \right\} \quad (E.21)$$

Finally, the distance between the neutral axis and the surface of the composite is given by

$$y_{c0} = \frac{[E_m t_m (t_c + 2t_a + t_h + \frac{t_m}{2}) + E_h t_h (t_c + t_a + \frac{t_h}{2}) + E_a t_a (2t_c + 2t_a + t_h) + E_c \frac{t_c^2}{2}]}{[E_m t_m + E_c t_c + E_h t_h + 2E_a t_a]} \quad (E.22)$$

All of the above equations were coded into a FORTRAN program and used to design the composite cross-beam structure used in the biaxial compression test rig.

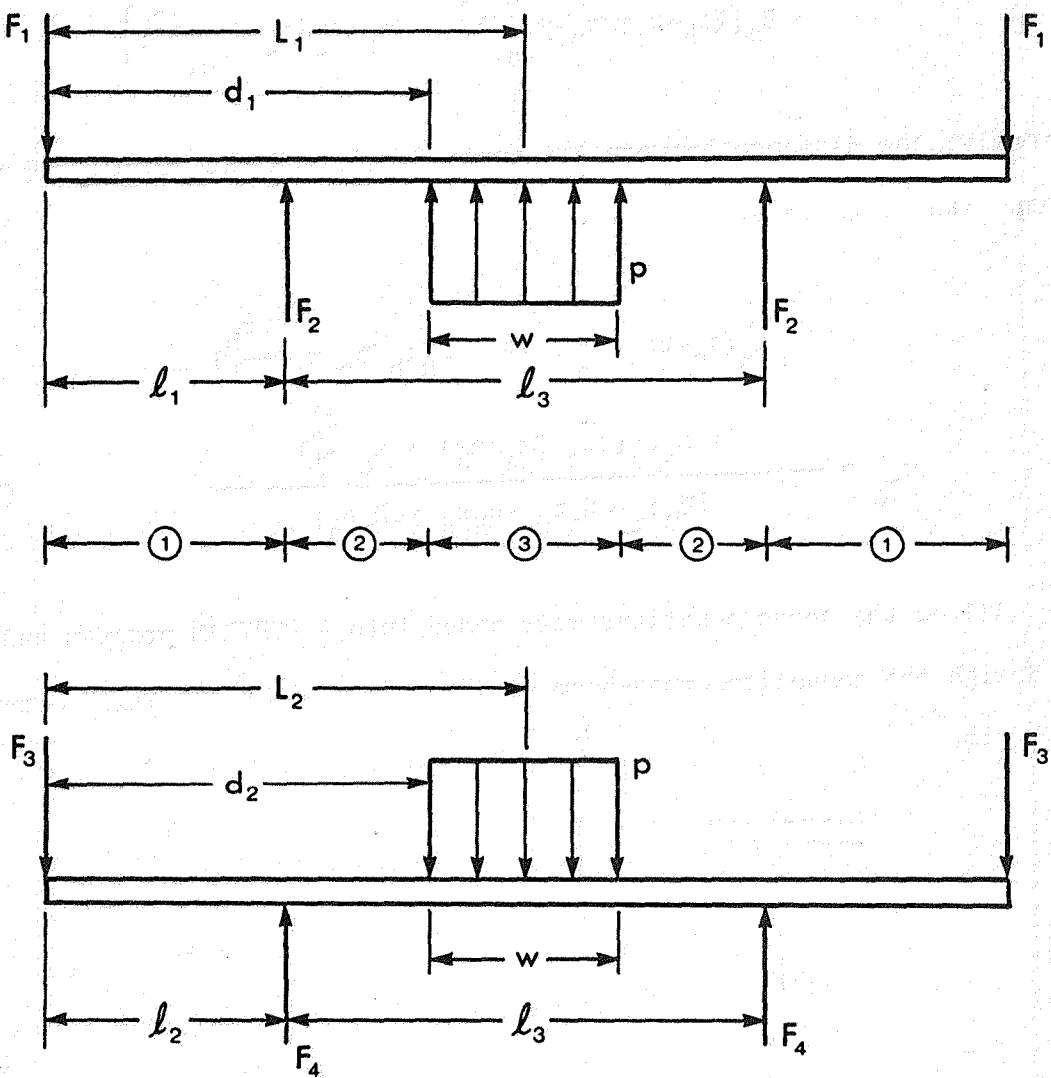


FIGURE E-1: Single Beam Loadings Comprising the Cross-Beam Loading

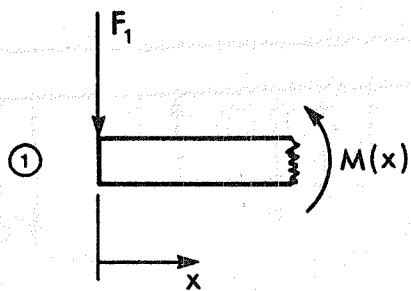


Fig. E-2a

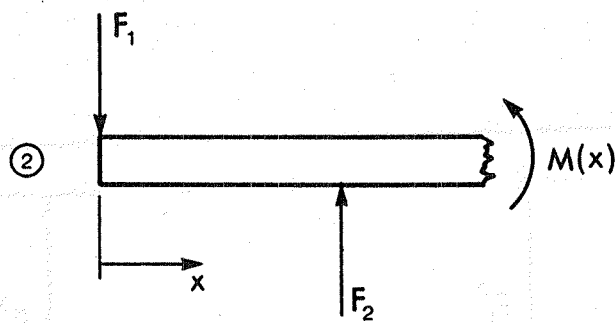


Fig. E-2b

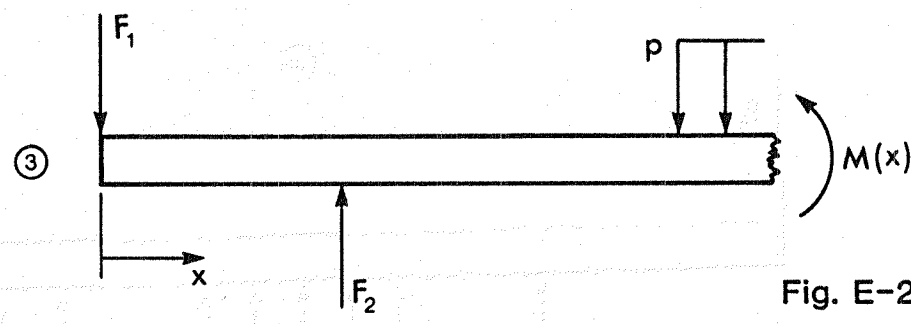


Fig. E-2c

FIGURE E-2: Bending Moments on Beam Sections

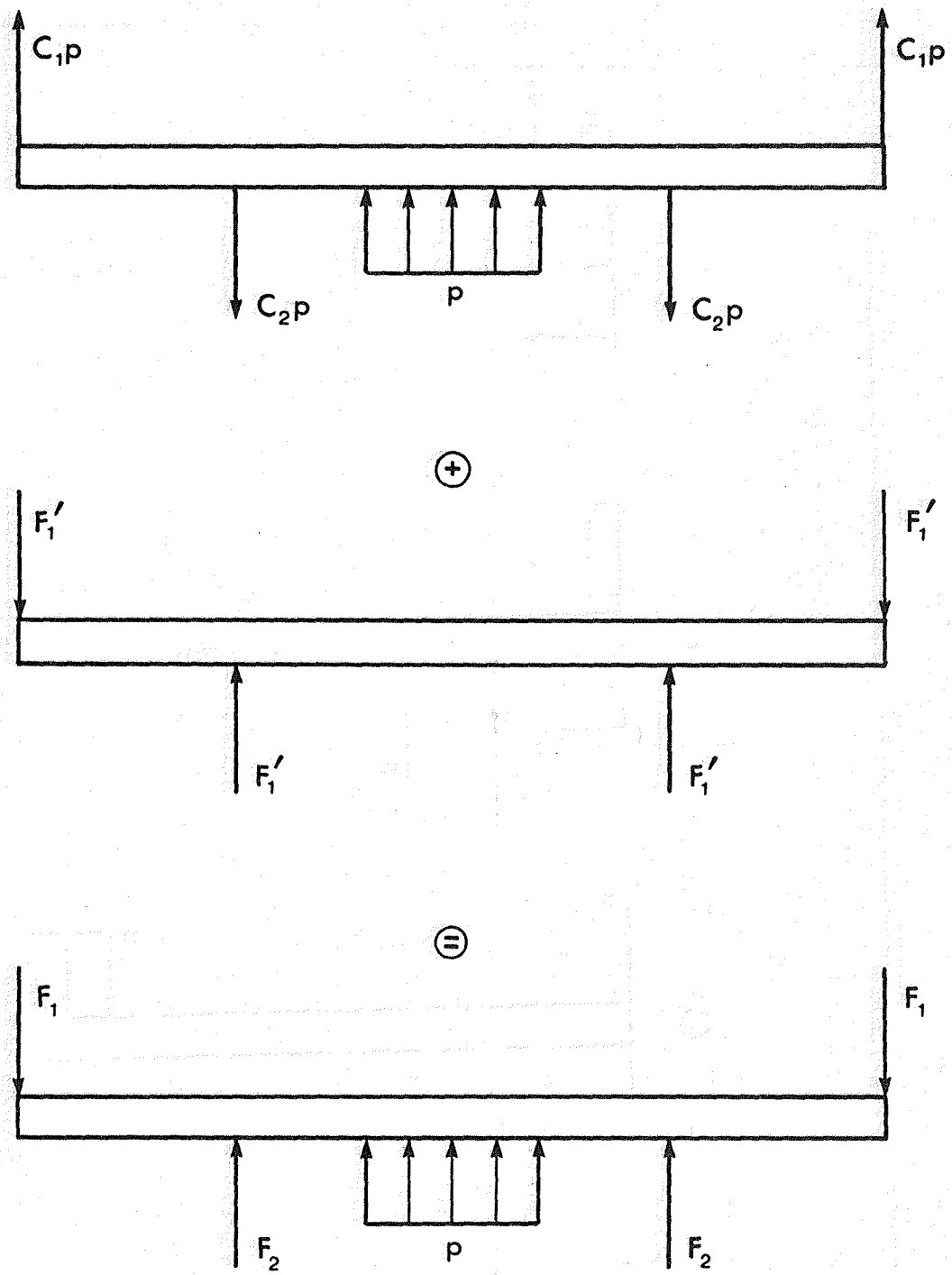


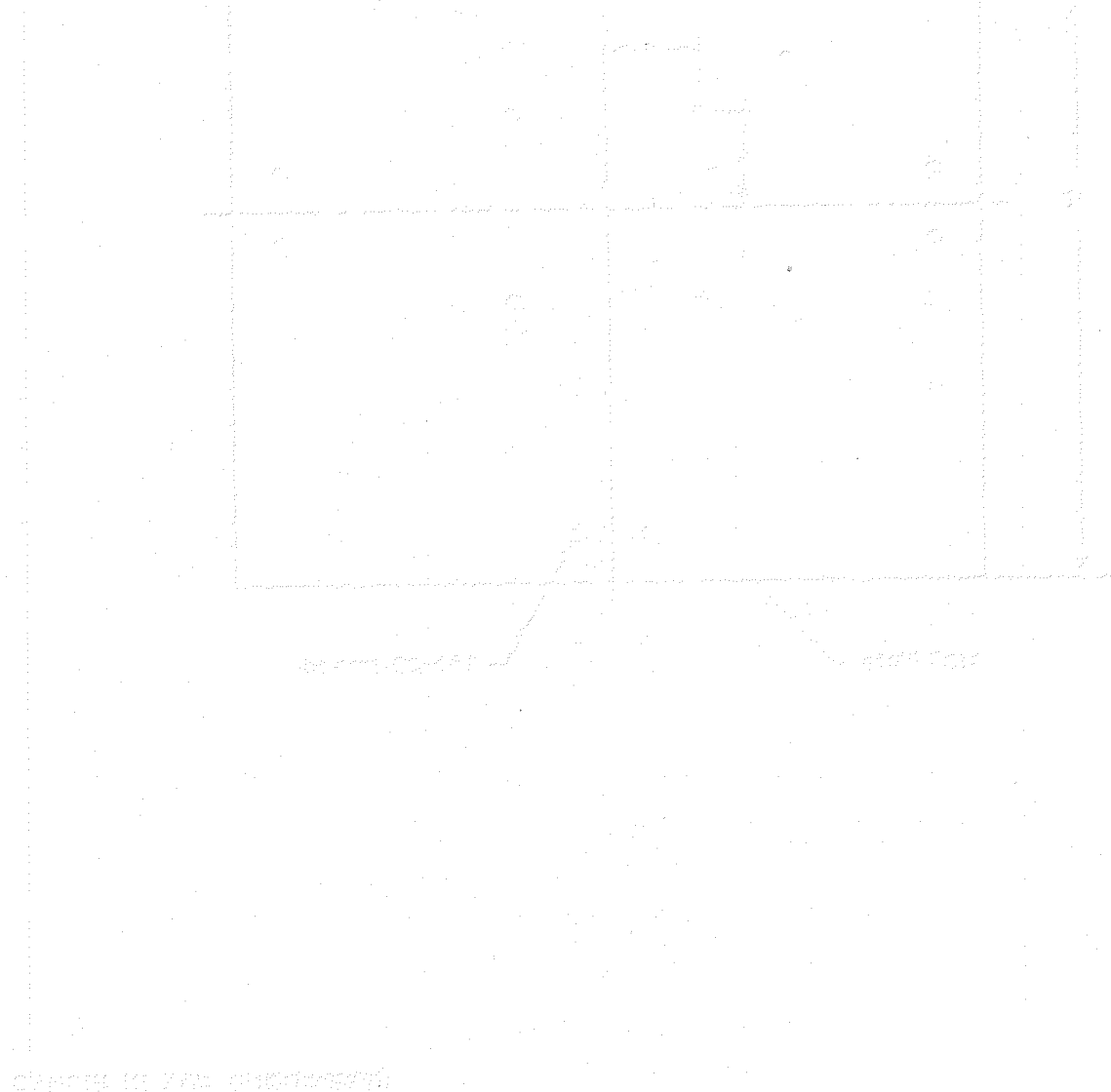
FIGURE E-3: Summation of Beam Loadings

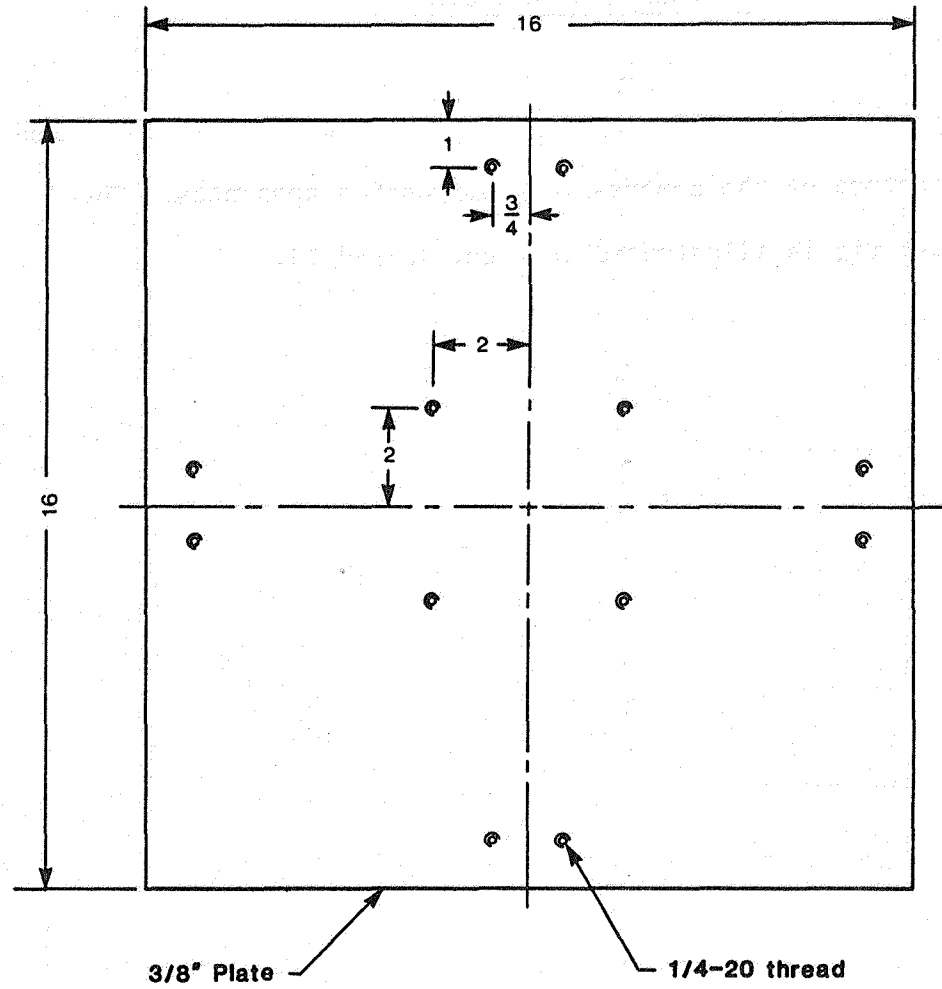
APPENDIX F

TECHNICAL DRAWINGS OF THE BIAXIAL

COMPRESSION TEST RIG

The figures on the following pages give the design drawings used in the manufacture of the compression-compression apparatus. The assembled test rig is illustrated in Figs. 13 and 14.





DIMENSIONS ARE IN INCHES

BASE PLATE

NO. REQ'D: 1

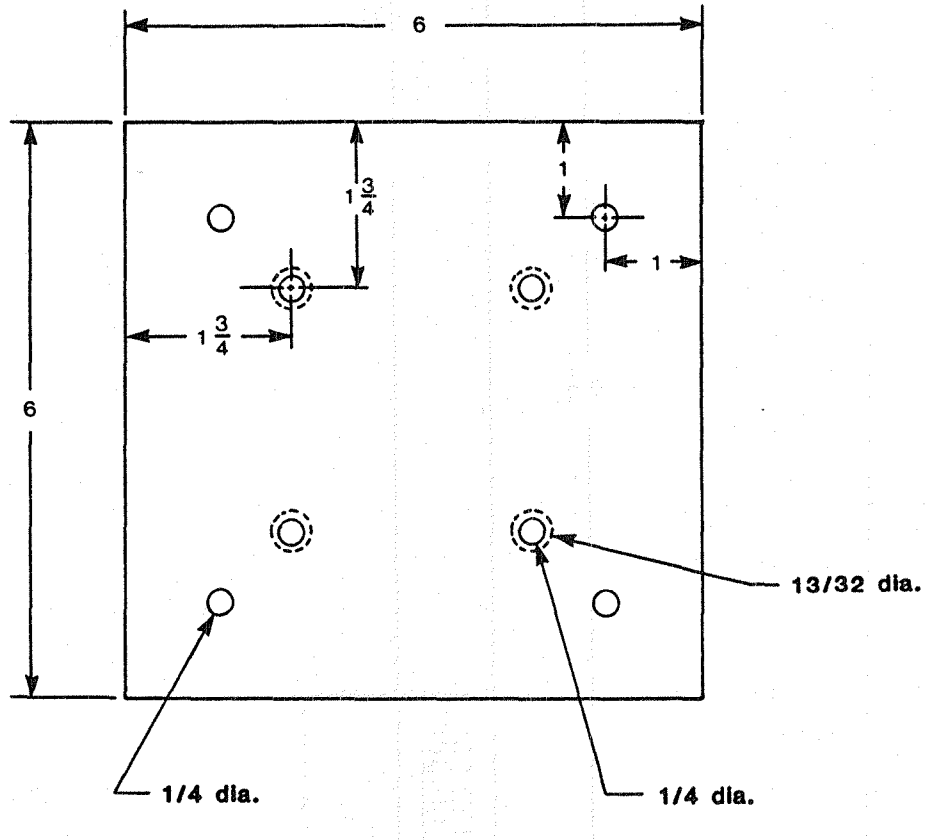
MATERIAL: ALUMINUM

SCALE 1:4

Drawn by: W.G. ELLIOTT

JULY 1982

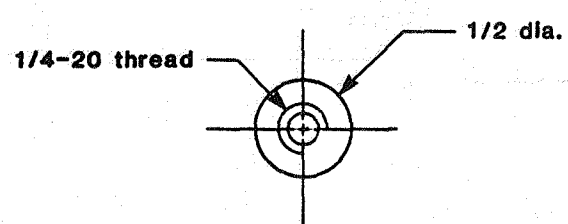
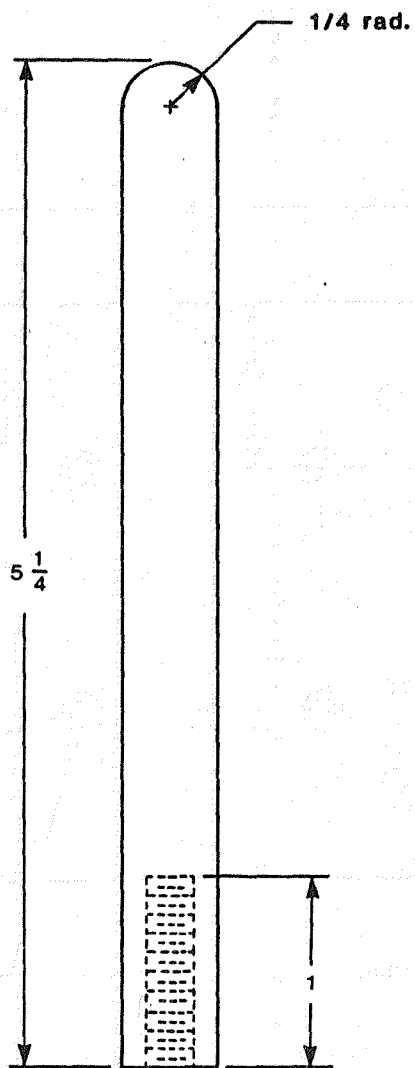
FIGURE F-1



DIMENSIONS ARE IN INCHES

GUIDE SUPPORT PLATE	NO. REQ'D: 1	MATERIAL: ALUMINUM
	SCALE 1:2	1/2
	Drawn by: W.G. ELLIOTT	JULY 1982

FIGURE F-2



DIMENSIONS ARE IN INCHES

CENTRAL LOAD BLOCK GUIDE

NO. REQ'D: 4

MATERIAL: MILD STEEL

FULL SCALE

Drawn by: W.G. ELLIOTT

JULY 1982

FIGURE F-3

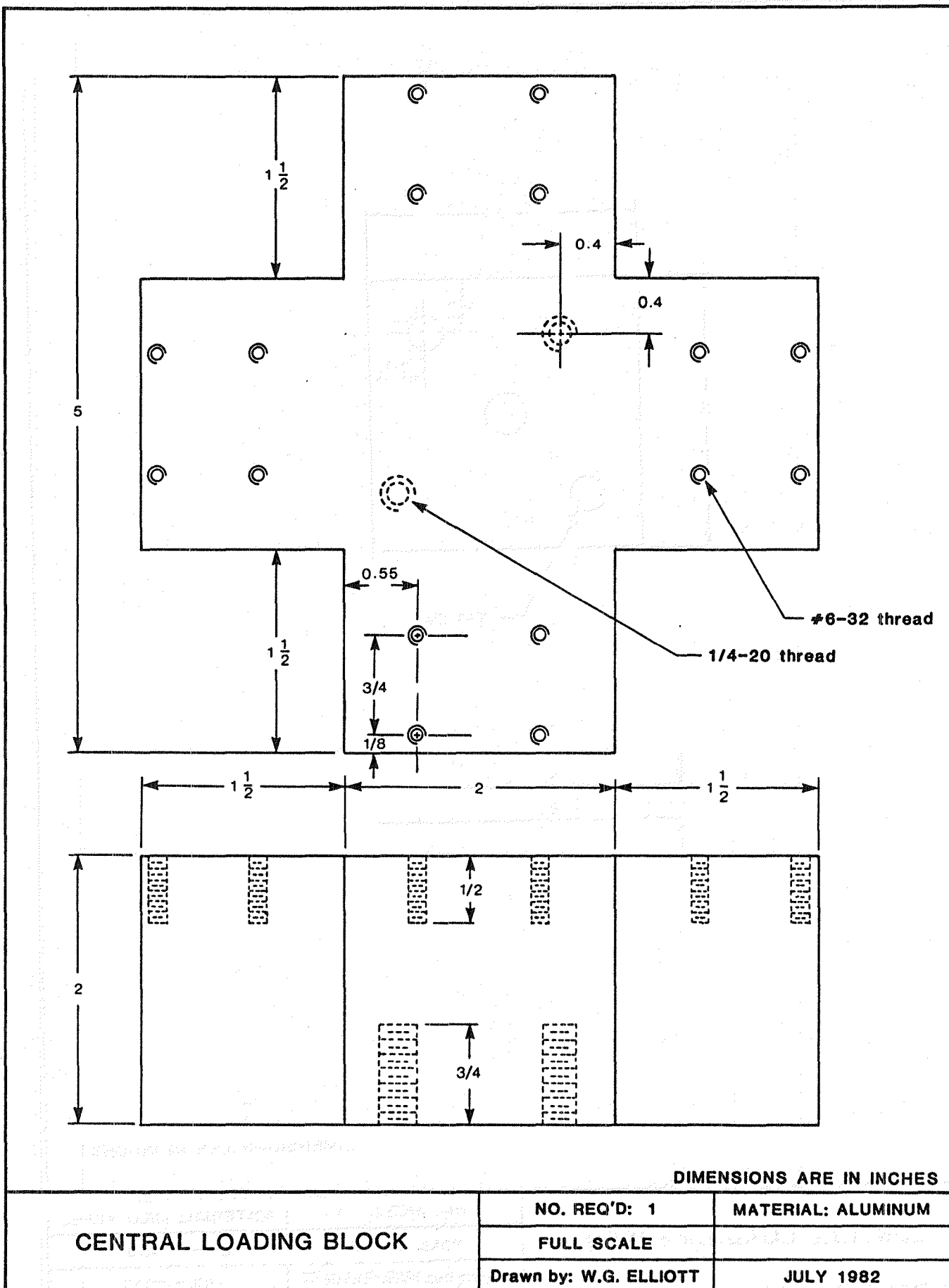


FIGURE F-4 115

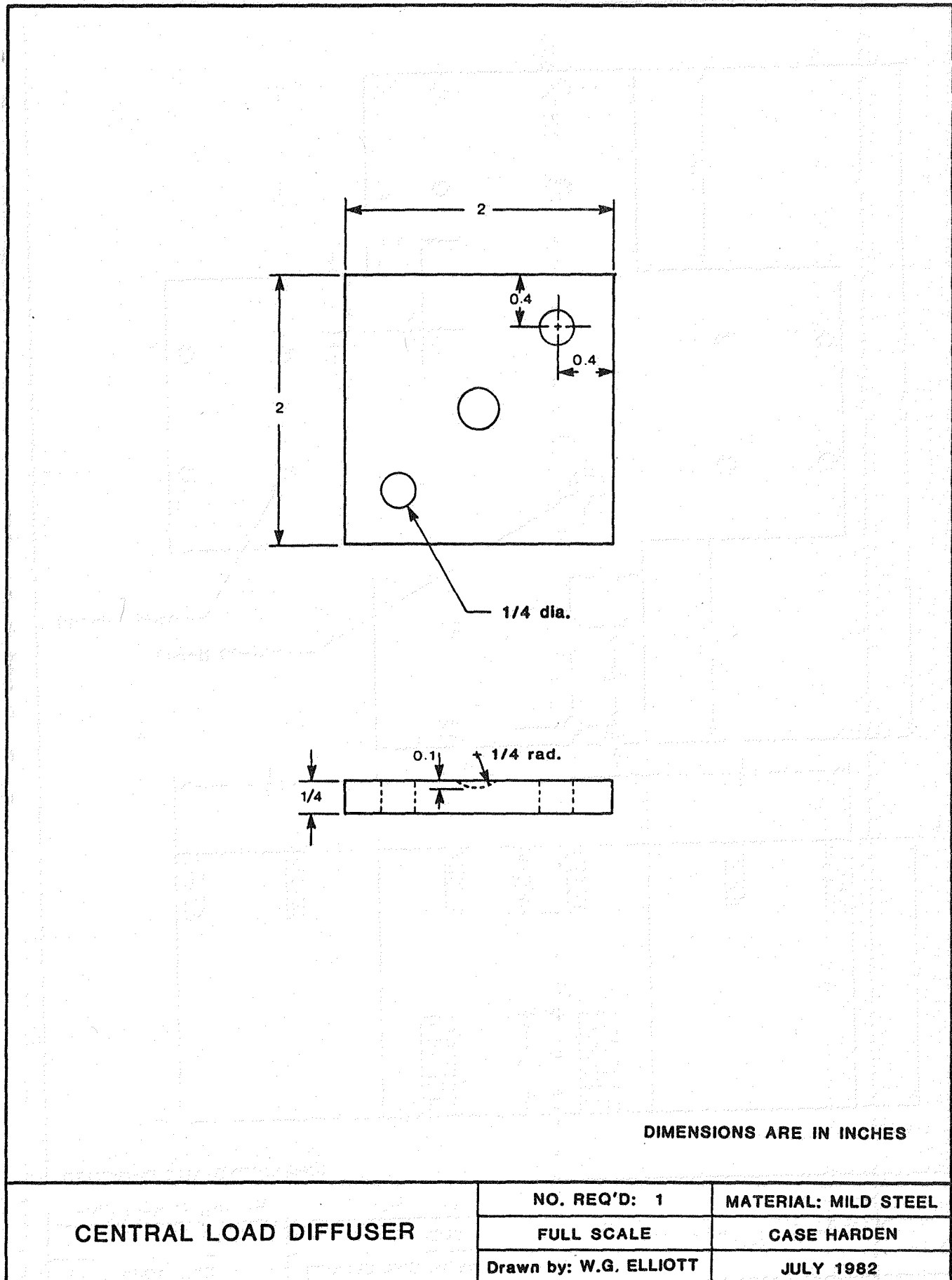
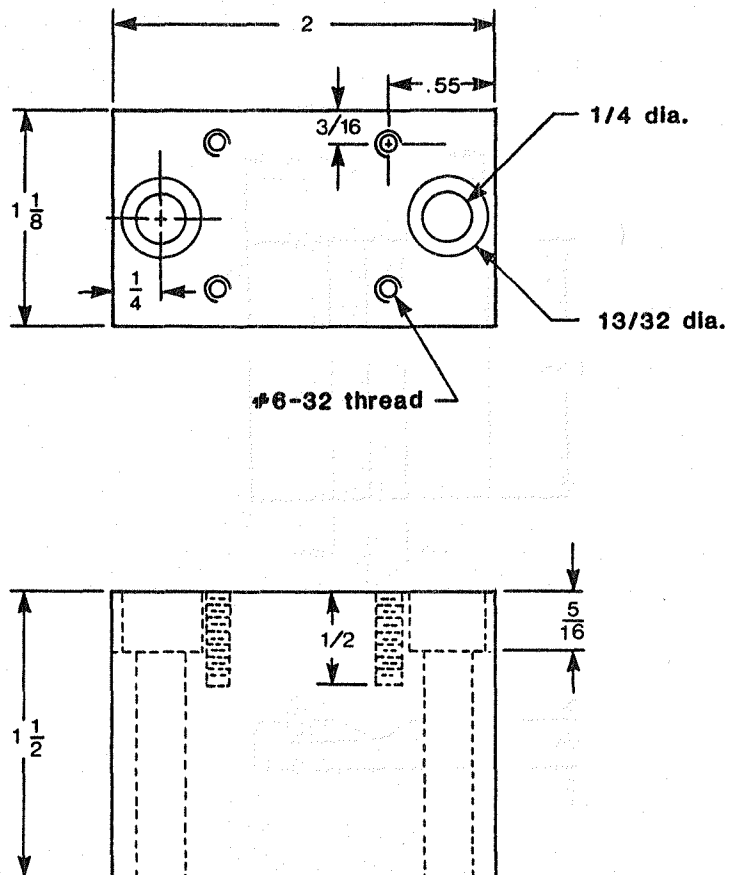


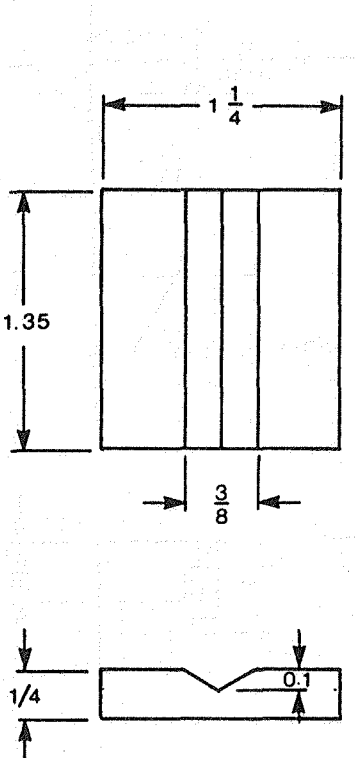
FIGURE F-5



DIMENSIONS ARE IN INCHES

ROCKER ELEVATOR AND SUPPORT	NO. REQ'D: 4 FULL SCALE	MATERIAL: ALUMINUM
	Drawn by: W.G. ELLIOTT	JULY 1982

FIGURE F-6



DIMENSIONS ARE IN INCHES

SIMPLE SUPPORT ROCKER PLATE

NO. REQ'D: 8

MATERIAL: MILD STEEL

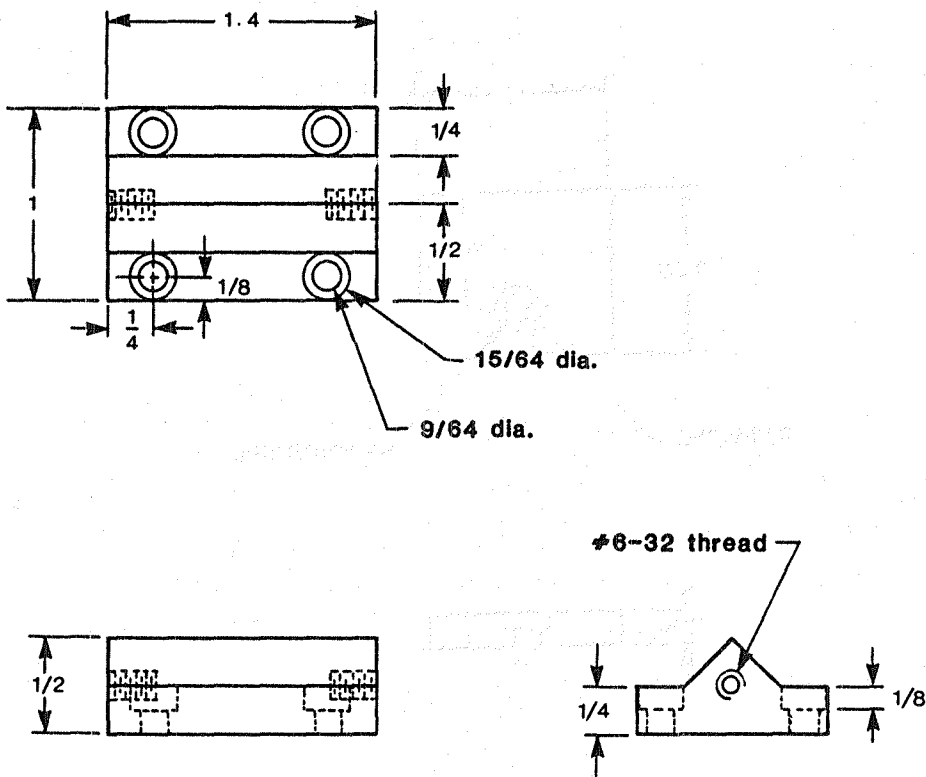
FULL SCALE

CASE HARDEN

Drawn by: W.G. ELLIOTT

JULY 1982

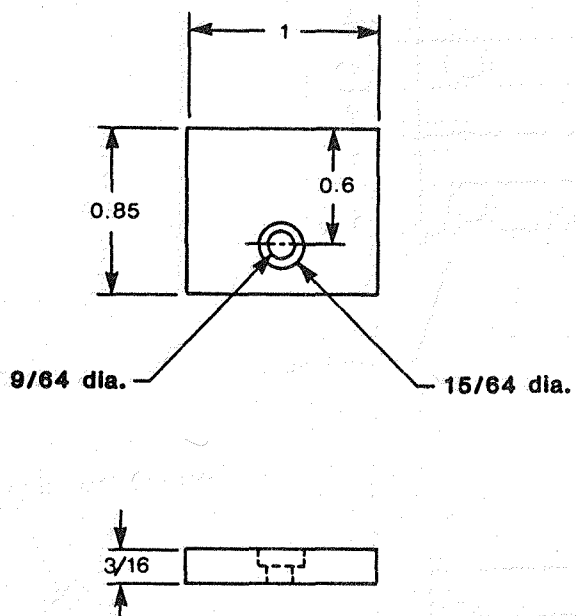
FIGURE F-7



DIMENSIONS ARE IN INCHES

SIMPLE SUPPORT ROCKER BASE	NO. REQ'D: 8	MATERIAL: MILD STEEL
	FULL SCALE	CASE HARDEN
	Drawn by: W.G. ELLIOTT	JULY 1982

FIGURE F-8



DIMENSIONS ARE IN INCHES

ROCKER BASE SIDE

NO. REQ'D: 16

MATERIAL: MILD STEEL

FULL SCALE

Drawn by: W.G. ELLIOTT

JULY 1982

FIGURE F-9

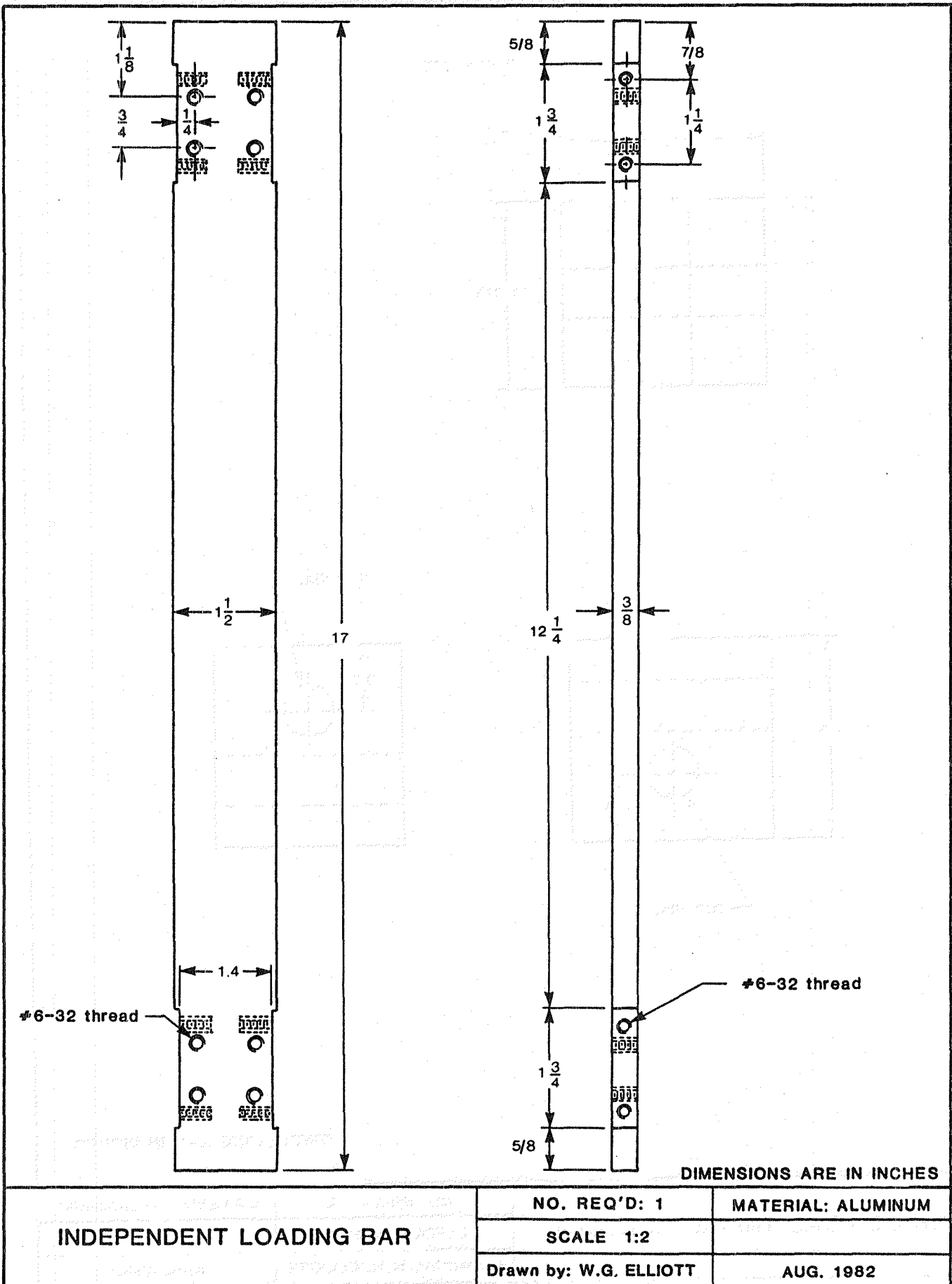
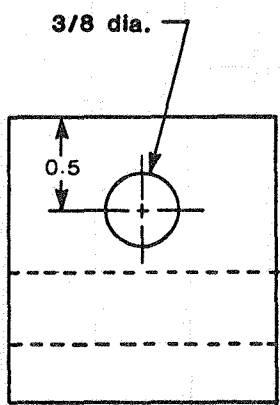
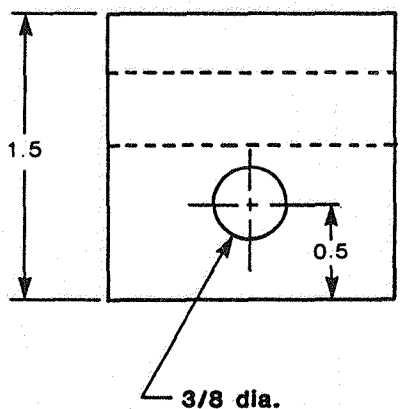
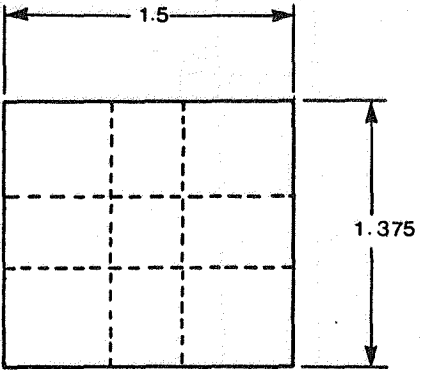


FIGURE F-10



DIMENSIONS ARE IN INCHES

CABLE LOAD TRANSFER BLOCK

NO. REQ'D: 2

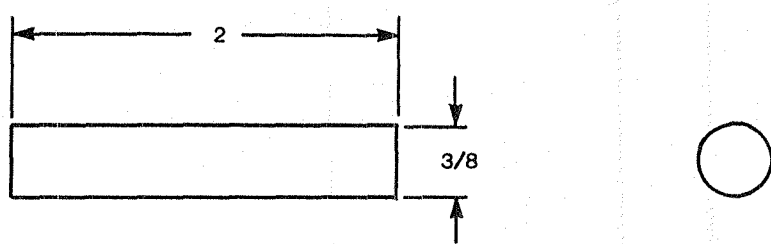
MATERIAL: ALUMINUM

FULL SCALE

Drawn by: W.G. ELLIOTT

AUG. 1982

FIGURE F-11



DIMENSIONS ARE IN INCHES

INDEPENDENT LOADING PIVOT PIN

NO. REQ'D: 2

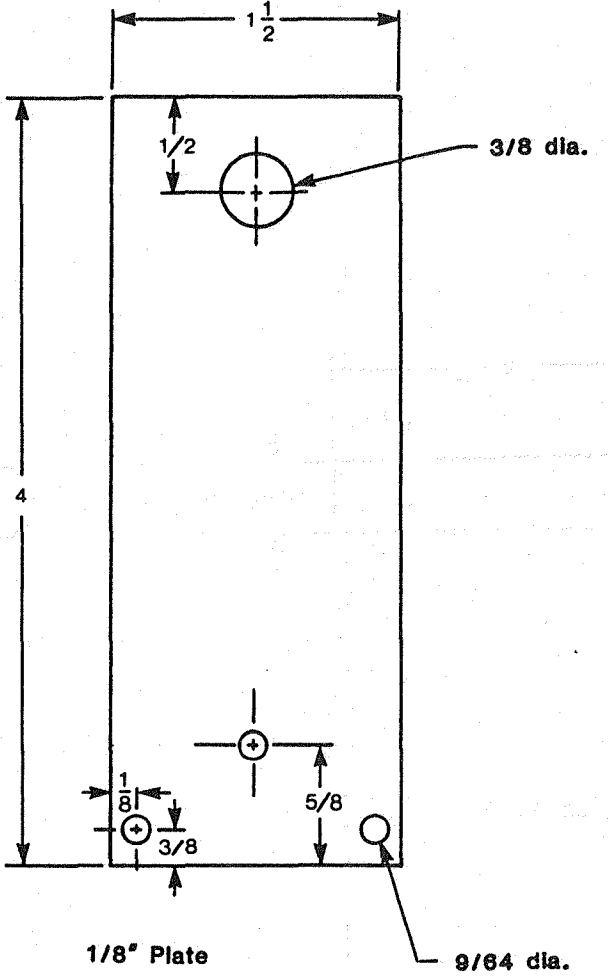
MATERIAL: MILD STEEL

FULL SCALE

Drawn by: W.G. ELLIOTT

AUG. 1982

FIGURE F-12



DIMENSIONS ARE IN INCHES

LOADING BAR SIDE

NO. REQ'D: 4

MATERIAL: MILD STEEL

FULL SCALE

Drawn by: W.G. ELLIOTT

AUG. 1982

FIGURE F-13

1. Report No. NASA CR-172192	2. Government Accession No.	3. Recipient's Catalog No.	
4. Title and Subtitle Failure Analysis of Composite Laminates Including Biaxial Compression		5. Report Date August 1983	
		6. Performing Organization Code	
7. Author(s) R. C. Tennyson W. G. Elliott		8. Performing Organization Report No.	
9. Performing Organization Name and Address University of Toronto Institute for Aerospace Studies Toronto, Ontario, Canada		10. Work Unit No.	
		11. Contract or Grant No. NSG-7409	
12. Sponsoring Agency Name and Address National Aeronautics and Space Administration Washington, DC 20546		13. Type of Report and Period Covered Contractor Report 8/80 - 8/82	
		14. Sponsoring Agency Code 505-42-23-03	
15. Supplementary Notes Langley Technical Monitor: Donald J. Baker Interim Report			
16. Abstract This report describes a continued effort on the development and application of the tensor polynomial failure criterion for composite laminate analysis. In particular, emphasis is given to the design, construction and testing of a cross-beam laminate configuration to obtain 'pure' biaxial compression failure. The purpose of this test case was to provide data to permit 'closure' of the cubic form of the failure surface in the 1-2 compression-compression quadrant. This resulted in a revised set of interaction strength parameters and the construction of a failure surface which can be used with confidence for strength predictions, assuming a plane stress state exists. Furthermore, the problem of complex conjugate roots which can occur in some failure regions is addressed and an 'engineering' interpretation is provided. Results are presented illustrating this behaviour and the methodology for overcoming this problem is discussed. Finally, a further application of the phenomenological approach using a failure equation is presented dealing with holes in laminates. Both analytical and experimental results are given to demonstrate an alternative method for predicting failure loads.			
17. Key Words (Suggested by Author(s)) Composite Structures Failure Analysis Laminates Modulus of Elasticity Tsi-Wu Criterion		18. Distribution Statement Unclassified - Unlimited Subject Category - 24	
19. Security Classif. (of this report) Unclassified	20. Security Classif. (of this page) Unclassified	21. No. of Pages 130	22. Price A07

End of Document